Variational Calculation of Fine and Hyperfine Resolved Rovibronic Spectra of Diatomic Molecules

Qianwei Qu

A dissertation submitted in partial fulfillment

of the requirements for the degree of

Doctor of Philosophy

of

University College London.

Department of Physics and Astronomy

University College London

July 2022

I, Qianwei Qu, confirm that the work presented in this thesis is my own. Where information has been derived from other sources, I confirm that this has been indicated in the work.

Abstract

The thesis presents methods for the variational calculation of fine and hyperfine resolved rovibronic spectra of diatomic molecules, as part of the ExoMol and ExoMolHD projects. The theory of these methods has been fully discussed. The corresponding algorithms have been implemented based on previous works of the ExoMol Group. The line lists of two molecules, NO and VO has been calculated, which validates the proposed methods.

Nitric oxide is one of the principal oxides of nitrogen, which plays a significant role the investigations of our atmosphere and astrophysics. Due to its importance, the radical has been investigated in numerous theoretical and experimental works. However, there is no NO ultraviolet line list in well-known databases. A major issue in generating a UV line list for NO results from the difficulty of modelling the valence-Rydberg interaction between its $B\,^2\Pi$ and $C\,^2\Pi$ states. To address the problem, a spectroscopic model has been proposed to resolve the energy structures of $B\,^2\Pi$ and $C\,^2\Pi$ coupled states. Based on the model, an accurate line list, called XABC, has been computed, which covers the pure rotational, vibrational and rovibronic spectra of $^{14}N^{16}O$.

Vanadium monoxide is also an open shell diatomic system. Its dominating isotopologue $^{51}V^{16}O$ has non-zero nuclear spin, $I = 7/2$. The interaction between the spin of unpaired electrons and the nuclear spin yields a very pronounced hyperfine structure. The widely used effective Hamiltonian method for hyperfine structure is not applicable to give accurate line list of VO, as the interactions between the electronic states of VO reshape its line positions and intensities. This thesis presents a variational algorithm for the calculation of hyperfine structure and spectra of di-

atomic molecules. The hyperfine-resolved IR spectra of VO has been computed from first principles, considering necessary nuclear hyperfine coupling curves.

Impact Statement

- The vibrational method for nuclear hyperfine structure presented in Chapter 3 is useful for the assignment and prediction of high-resolution spectra of diatomic molecules.

- The adiabatic coupling scheme presented in Chapter 4 can be used for calculating rovibronic spectra of other molecules (not limited to diatomic ones) whose electronic states interact, generating avoided-crossing structures in potential energy curves/surfaces.

- The IR-VIS-UV NO line list calculated in Chapter 5 gives more comprehensive references for astronomical spectroscopy and other hot applications, *e.g.* monitoring pollutants by laser absorption spectroscopy in combustion processes. Scientist may find more applicable transitions in the UV regions for laser induced fluorescence spectroscopy of NO.

- The development of VO spectroscopic model in Chapter 6 demonstrates the standard procedures of predicting nuclear hyperfine spectra of diatomic molecules. We will further improve the spectroscopic model and generate a comprehensive rovibronic line list including more electronic states of VO, which is expected to be used to analyse high-accuracy astronomical spectra.

Acknowledgements

I am immensely grateful to Jonathan Tennyson and Sergey Yurchenko for their kind support during my PhD programme. I would like to thank every ExoMoller I have met on my way as well, for your suggestions, for your encouragement, for your Good Mornings ...

Contents

List of associated publications

- Chapter 3: **Qianwei Qu**, Sergei N. Yurchenko, and Jonathan Tennyson*, "A method for the variational calculation of hyperfine-resolved rovibronic spectra of diatomic molecules", J. Chem. Theory Comput., 18(3): 1808–1820, 2022.

- Chapter 4: **Qianwei Qu**, Bridgette Cooper, Sergei N. Yurchenko, and Jonathan Tennyson*, "A spectroscopic model for the low-lying electronic states of NO", J. Chem. Phys., 154(7): 074112, 2021.

- Chapter 5: **Qianwei Qu**, Sergei N. Yurchenko, and Jonathan Tennyson*, "ExoMol molecular line lists – XLII: Rovibronic molecular line list for the low-lying states of NO", Mon. Not. Roy. Astron. Soc., 504(4): 5768-5777, 2021.

- Chapter 6: **Qianwei Qu**, Sergei N. Yurchenko, and Jonathan Tennyson*, "A variational model for the hyperfine resolved spectrum of VO in its ground electronic state", J. Chem. Phys., 157(12): 124305, 2022.

List of Figures

List of Tables

Chapter 1

Introduction

1.1 Molecular spectroscopic databases

Molecular spectroscopic techniques have been widely used in many applications. Astronomers identify the atmospheric components of exoplanets from the observed spectra [12, 13]. Other atmospheric parameters, such as temperature, can be estimated from spectral intensities or line shapes [14]. Scientists use spectroscopic instruments to monitor the concentrations of greenhouse gas and pollutants in the Earth's atmosphere [15, 16]. Doctors learn the physical conditions of patients from spectroscopic diagnoses [17]. Non-invasive spectroscopic techniques give accurate parameters for flames [18], which help engineers design high-efficiency and low-emission combustion systems.

The development of spectroscopic techniques depends on accurate complete spectroscopic databases. For example, high-resolution Doppler-shift spectroscopy [19] requires a wavelength resolving power of 100 000 or better [20]. The completeness plays a significant role as well. Unknown molecules can be identified from the observed spectrum only if complete line lists of all possible species are given in prior.

A spectroscopic database consists of spectral line lists of different molecules and each line list contains spectral lines of a specific molecule. A spectral line can be described by three important properties, *i.e.*, position, strength and shape. Thus, spectroscopic parameters which define the three properties are usually stored in line

lists.

A molecule has unique distribution of energy levels, leading to unique line positions. The line position is a intrinsic property of a molecule. Unknown species can be identified from line positions which have a similar function as the fingerprints. Line positions may shift, *e.g.*, due to the Doppler effect. We always assume that a line list stores the rest frequencies or wavelengths of a molecule. The line strength is another intrinsic property. The values of line strengths can be given in various units, *e.g.*, the Einstein coefficient or the oscillator strength. Line strengths are not directly observable. They are either calculated or derived from transition intensities which are temperature dependent. A spectral line usually has a profile due to broadening effects, which is the line shape property. Calculated or measured broadening parameters can be stored in a line list and the line shapes are simulated by reasonable physical models, *e.g.*, the Gaussian and Lorentzian profiles. External broadening mechanisms, *e.g.*, instrument broadening due to the resolution of instruments, may have observable effects but they are not the components of a line list.

Note that, the line position and line strength can be mixed by statistical effects when intermolecular interactions become strong, *e.g.*, in the high-pressure environments. They are no longer intrinsic properties of a single molecule but statistics related ones. Besides, we may also use statistical terms, *e.g.*, temperature, to describe line position and strength related features. For example, hot lines means they are hardly observed in low-temperature environments, where most molecules populate lower-lying energy levels, and hot lines connecting higher energy levels are weak. A hot line list includes the necessary hot lines of a molecule and can be used in both low-temperature and high-temperature applications.

The most well-used database for atmospheric studies is HITRAN [21]. HITRAN is mainly designed for conditions of the terrestrial atmosphere, particularly for temperatures ranging from the surface of the Earth to the stratosphere, and thus does not contain transitions originating from highlyexited energy levels. The room-temperature line lists contained in HITRAN are not complete enough for high-

temperature applications due to the absence of hot transitions, see Yurchenko *et al.* [22] for an illustration of this issue. The HITEMP database extends the temperature range of HITRAN. It was originally released in 1995 and updated in 2010 [23]; HITEMP encompasses many more bands and transitions than HITRAN but only for H_2O, CO_2, CO, NO and OH. An systematic update of HITEMP is currently in progress, see Hargreaves *et al.* [8]. Nevertheless, the five line lists in the 2010 release of HITEMP were insufficient for the majority of astronomical applications and are expected to be updated.

The atmospheres of even cool stars, brown dwarfs and most observable exoplanets are generally much hotter than of the Earth atmosphere. The ExoMol project was launched as a response to these data needs [24]. The ExoMol database (ExoMol.com) provides line list for spectroscopic studies of hot atmospheres [25] of exoplanets and other astronomical bodies.

The basic form of the ExoMol database is extensive line lists of molecular transitions; these are supplemented by partition functions, state lifetimes, cooling functions, Landé g-factors, temperature-dependent cross sections, opacities, pressure broadening parameter and k-coefficients. The 2020 release of the database was expanded to consider 80 molecules and 190 isotopologues, and contains over 700 billion transitions [25]. While these spectroscopic data are concentrated at infrared and visible wavelengths, ultraviolet transitions are being increasingly considered in response to requests from observers. These numbers are still increasing as we enrich the database with 'rolling-updates' nearly every month.

Besides HITRAN, HITEMP and ExoMol, there are other databases providing spectroscopic data. GEISA [26] is another room temperature database providing comprehensive and validated datasets for approximately 50 key atmospheric molecules. TheoReTS [27] contains hot line lists for 8 polyatomic molecules. Kurucz's compilation of data [28] is very complete for atomic sources but contains data only on about 10 diatomic molecules all of which are covered by ExoMol with higher accuracy. The MoLLIST database [29] of Bernath and coworkers contains empirically derived line lists for about 20 diatomic species. These line lists

have recently been incorporated into the ExoMol database [30]. The JPL [31] and CDMS [32] databases, aimed at the cool interstellar medium, provide comprehensive molecular line lists for wavelengths longer than 30 μm. The NASA Ames Research Center published a series of line lists of molecules, *e.g.*, SO_2 [33]. LIFBASE [34] contains the the datasets of several important radicals, *e.g.*, OH and NO, mainly for laser induced fluorescence investigations.

1.2 Motivation for variational calculation of diatomic spectra

In molecular spectroscopy, we expect the separation between different electronic states to be much larger than that between vibrational levels within each electronic state and the separation between vibrational levels is much larger than the separation between the rotational levels of a molecule. Thus, we can construct a Hamiltonian, which acts in a reduced space and describes the dominating part of the full Hamiltonian with a perturbation procedure to estimate the eigenvalue spectrum. This Hamiltonian is termed as effective Hamiltonian.

The effective Hamiltonian method is widely used in spectroscopic studies. Brown and Carrington [35] discussed how to derivean effective Hamiltonian for diatomic molecules. Well-known programs, *e.g.*, PGOPHER [36] and SPFIT/SPCAT [37], calculate spectra from effective Hamiltonians. Standard practice for the effective Hamiltonian in molecular spectroscopy is to calculate the rotational structure within a vibrational level. The results of effective Hamiltonian calculations can be very accurate, especially for the low-J rotational transitions. The spectral constants also have good physical definitions.

To improve accuracy of the calculated results, higher order corrections can be introduced into effective Hamiltonians when there are large gaps between the target energy levels and the perturbed eigenstates. For instance, Haze *et al.* use sextet-order centrifugal distortion constants to represent the measured high-J transitions in the $A\,^2\Sigma^+$- $X\,^2\Pi$ band system of NO [38]. Nevertheless, effective Hamiltonians can perform very poorly, especially in the regions where states interact. The hot

line lists in the ExoMol database always cover these regions. We, thus, turn to the variational method to give robust and accurate rovibronic spectra. The variational method constructs the Hamiltonian in a complete (or quasi-complete) space. Complex spectroscopic structures can be represented accurately in the variational basis set.

In practical applications, effective Hamiltonians are constructed to estimate the real Hamiltonians and to give spectroscopic constants. The spectroscopic constants are fitted to the experimental data such that the results are mathematically accurate. This phenomenological method is usually valid for interpolation but invalid for extrapolation, as the effective Hamiltonian based spectroscopic models are not really physically accurate. For example, the two dominate factors contributing to spin-splittings of the $X^3\Sigma_g^-$ state of O_2 are the spin-spin coupling within its ground state and the spin-orbit coupling between its $X^3\Sigma_g^-$ and $b^1\Sigma_g^+$ states [39, 40]. However, it is common to only consider the spin-spin coupling contribution in experimental works, *e.g.* Yu *et al.* [41], where effective Hamiltonians are used. Excluding one or more coupling curves may give correct line positions but wrong line intensities even for the fitted transitions.

In contrast, the variational method can include necessary coupling curves obtained in *ab initio* calculations, and give a physically meaningful spectroscopic model. The curves, instead of constants, can be further refined with experimental data. Thus, the variational method not only gives correct and accurate estimates for the properly assigned energy levels or transitions, but also reasonable predictions of unknown ones. This feature is very important for generating hot line lists from models refined by room-temperature data.

The most challenging part of solving quantum mechanical problems using the variational method is finding good variational basis sets. For instance, to find proper active space in multi-configuration self-consistent field calculations is very difficult and one usually need to try different combinations of orbitals and compare the calculated results with experimental values to give the final choice. Diatomic molecules are almost perfect systems for variational calculations. First, the vibrational lev-

els can be accurately determined by using grid base algorithms, *e.g.*, the discrete variable representation method. Second, the one dimensional problem is usually not computationally complex and we can get desired accuracy by increasing the number of vibrational basis functions. In the following chapters, we will see the power of the variational method in the interpretation of very complicated diatomic systems.

1.3 Thesis overview

Chapter 2 consists of the theoretical background for the variational calculation in diatomic spectroscopy. Two mathematical tools, the linear variational method and the theory of irreducible spherical tensor operators, are introduced in the first place. The following sections describe the calculation hierarchy used to characterize diatomic fine structure. A spectroscopic program, Duo, is introduced.

Chapter 3 covers the method for the variational calculation of hyperfine resolved spectra of diatomic molecules based on irreducible spherical tensor operator algebra. The hyperfine coupling terms considered are Fermi-contact, nuclear spin-electron spin dipole-dipole, nuclear spin-orbit, nuclear spin-rotation and nuclear electric quadrupole interactions. The method for the calculation of hyperfine-unresolved wavefunctions are given in Chapter 2. The wavefunctions are used as the variational basis functions, and fully hyperfine-resolved parity-conserved rovibronic Hamiltonian matrices for a given final angular momentum, $\boldsymbol{F}$, are constructed. Then the Hamiltonians are diagonalized to give hyperfine-resolved energies and wavefunctions. Electric transition dipole moment curves can then be used to generate a hyperfine-resolved line list by applying rigorous selection rules. This approach is tested for NO and MgH, and the results are compared to experiment and shown to be consistent with those given in the well-used effective Hamiltonian code PGOPHER.

Chapter 4 mainly discusses the interaction between electronic states of diatomic molecules. The rovibronic structure of the $A\,^2\Sigma^+$, $B\,^2\Pi$ and $C\,^2\Pi$ states of nitric oxide (NO) is studied in this chapter with the aim of producing comprehen-

sive line lists for its near ultraviolet spectrum. Empirical energy levels for the three electronic states are determined using a combination of the empirical MARVEL (Measured Active Rotational-Vibrational Energy Levels) procedure and *ab initio* calculations, and the available experimental data are critically evaluated. *Ab inito* methods which deal simultaneously with the Rydberg-like $A\,^2\Sigma^+$ and $C\,^2\Pi$ states, and the valence $B\,^2\Pi$ state are tested. Methods of modeling the sharp avoided crossing between the $B\,^2\Pi$ and $C\,^2\Pi$ states are tested. A rovibronic Hamiltonian matrix is constructed using variational nuclear motion program Duo whose eigenvalues are fitted to the MARVEL energy levels. The matrix also includes coupling terms obtained from the refinement of the *ab initio* potential energy and spin-orbit coupling curves. Calculated and observed energy levels agree well with each other, validating the applicability of our method and providing a useful model for this open shell system.

In Chapter 5, an accurate NO line list, called XABC, is computed based on the spectroscopic model built in Chapter 4, which covers its pure rotational, vibrational and rovibronic spectra. A mixture of empirical and theoretical electronic transition dipole moments are used for the final calculation of $^{14}N^{16}O$ rovibronic $A\,^2\Sigma^+$ – $X\,^2\Pi$, $B\,^2\Pi$ – $X^2\Pi$ and $C\,^2\Pi$ – $X\,^2\Pi$ transitions which correspond to the γ, β and δ band systems, respectively, as well as minor improvements to transitions within the $X\,^2\Pi$ ground state. The work is a major update of the ExoMol NOname line list. It provides a high-accuracy NO ultraviolet line list covering the complicated regions where the $B\,^2\Pi$-$C\,^2\Pi$ states interact. XABC provides comprehensive data for the lowest four doublet states of NO in the region of $\lambda > 160$ nm ($\tilde{\nu} < 63\ 000$ cm^{-1}) for the analysis of atmospheric NO on Earth, Venus or Mars, other astronomical observations and applications.

In Chapter 6, a variational model for the infra-red spectrum of VO is presented which aims to accurately predict the hyperfine structure within the VO $X\,^4\Sigma^-$ electronic ground state. To give the correct electron spin splitting of the $X\,^4\Sigma^-$ state, electron spin dipolar interaction within the ground state and the spin-orbit coupling between the $X\,^4\Sigma^-$ state and two excited states, $A\,^4\Pi$ and $1\,^2\Sigma^+$, are calcu-

lated *ab initio* alongside hyperfine interaction terms. Four hyperfine coupling terms are explicitly considered: the Fermi-contact interaction, electron spin-nuclear spin dipolar interaction, nuclear spin-rotation interaction and nuclear electric quadrupole interaction. These terms are included as part of a full variational solution of the nuclear-motion Schrödinger equation performed using program Duo, which is used to generate both hyperfine-resolved energy levels and spectra. To improve the accuracy of the model, *ab initio* curves are subject to small shifts. The energy levels generated by this model show good agreement with the recently derived empirical term values. This and other comparisons validate both our model in Chapter 3 and the developed hyperfine modules in Duo.

Chapter7 summarizes the contents of this thesis and gives potential future work.

1.4 Data availability

The programs, spectroscopic models and line lists mentioned in this thesis are available online.

Duo is an open-source software for variational calculations of spectra of diatomic molecules [42] , which is available at https://github.com/ExoMol/Duo . ExoCross is an open-source software for generating lifetimes, spectra, partition function *etc.* [43], which is available at https://github.com/ExoMol/ExoCross . The spectroscopic models of NO and VO, and the line list of NO are available at https://exomol.com .

Chapter 2

Theoretical Background

2.1 Linear variational method

In a quantum system, the variational principle (also termed as the variation principle in quantum chemistry books, *e.g.* Szabo and Ostlund [44]) allows us to calculate an upper bound for the ground state energy.

Theorem: The variational principle

E_0 is the lowest-energy eigenvalue of time independent Hamiltonian $\mathcal{H}$, if ψ is a normalized well-behaved function and satisfy the boundary conditions, then,

$$\langle\psi|\mathcal{H}|\psi\rangle \geq E_1.$$

In this equation, $W = \langle\psi|\mathcal{H}|\psi\rangle$ is called the variational integral and $|\psi\rangle$ is called a trial variation function.

The variational principle is easily proved by expanding $|\psi\rangle$ in terms of the eigenfunctions of $\mathcal{H}$ (see, *e.g.*, Section 8.1 of Levine [45]). Note that, $|\psi\rangle$ is not necessarily normalized. A more general equation includes a normalization factor, *i.e.*

$$\frac{\langle\psi|\mathcal{H}|\psi\rangle}{\langle\psi|\psi\rangle} \geq E_1. \tag{2.1}$$

In this thesis, we always assume $|\psi\rangle$ is normalized and our mission is to find the

minimum of W due to the trial function, *i.e.* solve the variational problem

$$\begin{aligned} \min_{|\psi\rangle} \quad & W = \langle\psi|\mathcal{H}|\psi\rangle \\ \text{s.t.} \quad & \langle\psi|\psi\rangle = 1. \end{aligned} \tag{2.2}$$

Here, a widely used method, the linear variational method is introduced, which lays the theoretical foundation of this thesis.

In the linear variational method, a trial function is chosen as the linear combination of n linearly independent functions $|\phi_1\rangle, \cdots, |\phi_n\rangle$, *i.e.*

$$|\psi\rangle = \sum_{i=1}^{n} c_i \, |\phi_i\rangle, \tag{2.3}$$

and

$$\langle\psi| = \sum_{i=1}^{n} c_i^* \, \langle\phi_i|. \tag{2.4}$$

The functional minimization problem, *i.e.* Eq,(2.2), is equivalent to:

$$\begin{aligned} \min_{\boldsymbol{c}} \quad & W = \sum_{i=1}^{n}\sum_{j=1}^{n} c_i^* c_j H_{ij} \\ \text{s.t.} \quad & \sum_{i=1}^{n}\sum_{j=1}^{n} c_i^* c_k S_{ij} = 1, \end{aligned} \tag{2.5}$$

where the components of $\boldsymbol{c}$ are the linear combination coefficients; H_{ij} is short for $\left\langle\phi_i\middle|\mathcal{H}\middle|\phi_j\right\rangle$; $S_{ij} = \left\langle\phi_i\middle|\phi_j\right\rangle$ is called the overlap integral. The constraint optimization problem can be solved by defining a Lagrange function

$$\mathcal{L}(\boldsymbol{c}, \lambda) = \sum_{i=1}^{n}\sum_{j=1}^{n} c_i^* c_j H_{ij} - \lambda\left[\sum_{i=1}^{n}\sum_{j=1}^{n} c_i^* c_j S_{ij} - 1\right], \tag{2.6}$$

where λ is the Lagrange multiplier. The variation of $\mathcal{L}$ with respect to $\boldsymbol{c}$ is set to zero, *i.e.*,

$$0 = \delta\mathcal{L} = \sum_{i=1}^{n}\sum_{j=1}^{n}\delta c_i^*\, c_j H_{ij} - \lambda\sum_{i=1}^{n}\sum_{j=1}^{n}\delta c_i^*\, c_j S_{ij} + \sum_{i=1}^{n}\sum_{j=1}^{n} c_i^*\,\delta c_j\, H_{ij} - \lambda\sum_{i=1}^{n}\sum_{j=1}^{n} c_i^*\,\delta c_j\, S_{ij}. \tag{2.7}$$

Then,

$$\sum_{i=1}^{n}\delta c_i^*\left[\sum_{j=1}^{n} c_j H_{ij} - \lambda c_j S_{ij}\right] + \sum_{j=1}^{n}\delta c_j\left[\sum_{i=1}^{n} c_i^* H_{ij} - \lambda c_i^* S_{ij}\right] = 0. \tag{2.8}$$

As $H_{ij} = H_{ji}^*$, $S_{ij} = S_{ji}^*$ and λ is a real number, the second term of Eq. (2.8)

$$\sum_{j=1}^{n}\delta c_j\left[\sum_{i=1}^{n} c_i^* H_{ij} - \lambda c_i^* S_{ij}\right] = \sum_{j=1}^{n}\delta c_j\left[\sum_{i=1}^{n} c_i H_{ji} - \lambda c_i S_{ji}\right]^* = \left\{\sum_{j=1}^{n}\delta c_j{}^*\left[\sum_{i=1}^{n} c_i H_{ji} - \lambda c_i S_{ji}\right]\right\}^*, \tag{2.9}$$

is the complex conjugate of the first term of Eq. (2.8). Thus, due to the arbitrariness of δc_i^*, we have

$$\sum_{j=1}^{n} c_j H_{ij} - \lambda c_j S_{ij} = 0, \text{ for } i = 1, \cdots, n. \tag{2.10}$$

All n equations comprise a homogeneous linear system of $\boldsymbol{c}$, which can be rewritten in matrix form:

$$[\boldsymbol{H} - \lambda\boldsymbol{S}]\boldsymbol{c} = 0. \tag{2.11}$$

It has non-trivial solutions if and only if

$$\det(\boldsymbol{H} - \lambda\boldsymbol{S}) = 0. \tag{2.12}$$

In this thesis, we use orthonormal basis functions, *i.e.*, $\langle\phi_i|\phi_j\rangle = \delta_{ij}$. Thus, the overlap matrix decays to an identity matrix, $\mathbf{1}$. The solutions for the equation

$$\det(\boldsymbol{H} - \lambda\mathbf{1}) = 0,$$

λ_i, $i = 1, \cdots, n$, are the eigenvalues of $\boldsymbol{H}$. We can choose a set of orthonormal eigenvectors of $\boldsymbol{H}$ as the solutions for $\boldsymbol{c}$, *i.e.*, $\{\boldsymbol{c}_i \mid i = 1, \cdots, n\}$. If the eigenvalues are arranged in order,

$$\lambda_1 \leq \lambda_2 \leq \cdots \leq \lambda_n,$$

then λ_1 gives the upper bound of the ground quantum state because of the reality:

$$E_1 \leq W_1 = \sum_{i=1}^{n} \sum_{j=1}^{n} c_{1i}^{*} c_{1j} H_{ij} = \boldsymbol{c}_1^{\dagger} \boldsymbol{H} \boldsymbol{c}_1 = \lambda_1 \boldsymbol{c}_1^{\dagger} \boldsymbol{c}_1 = \lambda_1. \tag{2.13}$$

It has been proved [46] that if the bound states of a quantum system are numbered in order of increasing energy,

$$E_1 \leq E_2 \leq \cdots \leq E_n \leq \cdots, \tag{2.14}$$

then λ_i gives the upper bound of E_i,

$$E_i \leq W_i = \lambda_i, \text{ for } i = 1, \cdots, n. \tag{2.15}$$

Thus, we can also estimate the energies of the lowest n states of a quantum system with $\lambda_i, i = 1, ..., n$ and the corresponding wavefunctions are

$$|\psi_i\rangle = \sum_{j=1}^{n} c_{ij} \left|\phi_j\right\rangle, \text{ for } i = 1, \cdots, n. \tag{2.16}$$

Details of the calculation of rovibronic spectra of diatomic molecules via the variational method will be given in Section 2.6. In Chapter 3 we will see variational calculations of hyperfine resolved spectra of diatomic molecules as well. Within each calculation hierarchy the procedures for a variational calculation can be simply summarized as:

1. Choose an appropriate basis set;

2. Construct the Hamiltonian matrix $\boldsymbol{H}$ in the representation of the basis set;

3. Diagonalize the matrix and obtain the estimate of energies and wavefunctions

of the calculated quantum system.

Thus, the linear variational method is implicitly used if a Hamiltonian matrix is diagonalized to give the eigenstates of a quantum system in the following sections and chapters.

2.2 List of angular momenta

The angular momenta used and associated quantum numbers in this thesis are listed in Table 2.1.

Table 2.1: Summary of symbols used to represent angular and other related variables in this thesis.

Symbol	Explanation
$\boldsymbol{S}, S$	total electron spin angular momentum and the corresponding quantum number
Σ	projection of $\boldsymbol{S}$ along the internuclear axis
$\boldsymbol{L}$	total orbital angular momentum
Λ	projection of $\boldsymbol{L}$ along the internuclear axis
$\boldsymbol{J}, J$	total angular momentum excluding nuclear spin and the corresponding quantum number
Ω, M_J	projection of $\boldsymbol{J}$ along the internuclear axis and space-fixed Z axis
$\boldsymbol{I}, I$	nuclear spin angular momentum and the corresponding quantum number
$\boldsymbol{F}, F$	total angular momentum and the corresponding quantum number
M_F	projection of $\boldsymbol{F}$ along the space-fixed Z axis
$\boldsymbol{N}, N$	total angular momentum excluding electron and nuclear spin and the corresponding quantum number
$\boldsymbol{R}$	rotational angular momentum of the bare nuclei

2.3 Irreducible spherical tensor operators

The fine and hyperfine structure of diatomic molecules mainly arises from the interactions between electric or magnetic multipole moments. The theory of irreducible spherical tensor operators is a powerful tool for analysing the coupling of angular momenta. This section gives a basic introduction of spherical tensor algebra. See Edmonds [47] for more details.

Definition: Irreducible spherical tensor operators

An irreducible tensor operator $\mathrm{T}^k(\boldsymbol{T})$ is a set of $2k+1$ operators $\mathrm{T}^k_p(\boldsymbol{T})$ which transform under rotations of the frame of coordinates as [47]

$$\mathcal{R}(\boldsymbol{\omega})\,\mathrm{T}^k_p(\boldsymbol{T})\,\mathcal{R}^{-1}(\boldsymbol{\omega}) = \sum_{p'} \mathrm{T}^k_{p'}(\boldsymbol{T})\,\mathcal{D}^{(k)}_{p'p}(\boldsymbol{\omega}),$$

where $\boldsymbol{\omega}$ indicates the rotational Euler angles; $\mathcal{R}(\boldsymbol{\omega})$ represents the rotation transformation corresponding to $\boldsymbol{\omega}$; $\mathcal{D}^{(k)}_{p'p}(\boldsymbol{\omega})$ is the Wigner rotation matrix.

Then angular momentum itself is an example of a rank-1 spherical tensor operator:

$$\begin{aligned}
\mathrm{T}^1_1(\boldsymbol{J}) &= -\frac{1}{\sqrt{2}} J_+ , \\
\mathrm{T}^1_0(\boldsymbol{J}) &= J_z , \\
\mathrm{T}^1_{-1}(\boldsymbol{J}) &= \frac{1}{\sqrt{2}} J_- .
\end{aligned}$$

When evaluating the matrix elements of spherical tensor operators, we may rotate the operator and wavefunctions:

$$\left\langle \eta, j, m \middle| \mathrm{T}^k_q(\boldsymbol{T}) \middle| \eta, j', m' \right\rangle = \sum_{n,n',p} \mathcal{D}^{(j)}_{n,m}(\boldsymbol{\omega})^*\, \mathcal{D}^{(k)}_{p,q}(\boldsymbol{\omega})\, \mathcal{D}^{(j')}_{n',m'}(\boldsymbol{\omega}) \left\langle \eta, j, n \middle| \mathrm{T}^k_p(\boldsymbol{T}) \middle| \eta, j', n' \right\rangle . \tag{2.17}$$

where the Wigner rotation matrix satisfies

$$\mathcal{D}^{(k)}_{p,q}(\boldsymbol{\omega})^* = (-1)^{p-q}\, \mathcal{D}^{(k)}_{-p,-q}(\boldsymbol{\omega}). \tag{2.18}$$

Integrating over all $\boldsymbol{\omega}$ and dividing by $8\pi^2$, the equation gives:

$$\left\langle \eta, j, m \middle| \mathrm{T}^k_q(\boldsymbol{T}) \middle| \eta, j', m' \right\rangle$$

$$=(-1)^{j-m}\begin{pmatrix} j & k & j' \\ -m & q & m' \end{pmatrix}\left[\sum_{n,n',p}(-1)^{j-n}\begin{pmatrix} j & k & j' \\ -n & p & n' \end{pmatrix}\left\langle \eta, j, n\middle|\mathrm{T}^k_p(\boldsymbol{T})\middle|\eta, j', n'\right\rangle\right], \quad (2.19)$$

where $\begin{pmatrix} j_1 & j_2 & j_3 \\ m_1 & m_2 & m_3 \end{pmatrix}$ is a Wigner-3j symbol. This equation indeed gives the well-known Wigner-Eckart Theorem.

Theorem: The Wigner-Eckart Theorem

For a spherical tensor $\mathrm{T}^k(\boldsymbol{T})$ acting on $|j,m\rangle$,

$$\left\langle \eta, j, m\middle|\mathrm{T}^k_p(\boldsymbol{T})\middle|\eta', j', m'\right\rangle = (-1)^{j-m}\begin{pmatrix} j & k & j' \\ -m & p & m' \end{pmatrix}\left\langle \eta, j\middle\|\mathrm{T}^k(\boldsymbol{T})\middle\|\eta', j'\right\rangle,$$

where $\left\langle \eta, j\middle\|\mathrm{T}^k(\boldsymbol{T})\middle\|\eta', j'\right\rangle$ is independent of the projection quantum numbers and called a reduced matrix element [47]. The definition of reduced matrix element used here is due to Edmonds [47].

The reduced matrix element can be evaluated from one component of the matrix element. For instance,

$$\begin{aligned}\left\langle j, m\middle|\mathrm{T}^1_0(\boldsymbol{J})\middle|j', m'\right\rangle &= (-1)^{j-m}\begin{pmatrix} j & 1 & j' \\ -m & 0 & m' \end{pmatrix}\left\langle j\middle\|\mathrm{T}^1(\boldsymbol{J})\middle\|j'\right\rangle \\ &= (-1)^{j-m}(-1)^{j-m}m\sqrt{j(j+1)(2j+1)}\left\langle j\middle\|\mathrm{T}^1(\boldsymbol{J})\middle\|j'\right\rangle. \quad (2.20)\end{aligned}$$

The left-hand-side is easily obtained from the Cartesian operator:

$$\left\langle j, m\middle|\mathrm{T}^1_0(\boldsymbol{J})\middle|j', m'\right\rangle = \langle j, m\middle|J_Z\middle|j', m'\rangle = \delta_{jj'}\,\delta_{mm'}\,m. \quad (2.21)$$

Then,

$$\left\langle j\middle\|\mathrm{T}^1(\boldsymbol{j})\middle\|j'\right\rangle = \delta_{j,j'}\sqrt{j(j+1)(2j+1)}. \quad (2.22)$$

Without proof, we give some standard results from spherical tensor algebra, which reveal the coupling schemes of spherical tensor operators [47].

If $\boldsymbol{j} = \boldsymbol{j}_1 + \boldsymbol{j}_2$ and $\mathrm{T}^k(\boldsymbol{T}_1)$ acts only on j_1, then

$$\begin{aligned}&\left\langle j_1, j_2, j \middle\| \mathrm{T}^k(\boldsymbol{T}_1) \middle\| j_1', j_2', j' \right\rangle \\ &= \delta_{j_2,j_2'} (-1)^{j_1+j_2+j'+k} \sqrt{(2j+1)(2j'+1)} \begin{Bmatrix} j_1' & j' & j_2 \\ j & j_1 & k \end{Bmatrix} \left\langle j_1 \middle\| \mathrm{T}^k(\boldsymbol{T}_1) \middle\| j_1' \right\rangle, \end{aligned} \tag{2.23}$$

where $\begin{Bmatrix} j_1 & j_2 & j_3 \\ j_4 & j_5 & j_6 \end{Bmatrix}$ is a Wigner-6j symbol.

The scalar product of two spherical tensors of rank k is defined as

$$\mathrm{T}^k(\boldsymbol{T}_1) \cdot \mathrm{T}^k(\boldsymbol{T}_2) = \sum_p (-1)^p \mathrm{T}^k_p(\boldsymbol{T}_1) \mathrm{T}^k_{-p}(\boldsymbol{T}_2). \tag{2.24}$$

The following equation decouples the scalar product of two spherical tensors operating on two angular momenta, $\boldsymbol{T}_1$ and $\boldsymbol{T}_2$, respectively.

$$\begin{aligned}&\left\langle j_1, j_2, j, m \middle| \mathrm{T}^k(\boldsymbol{T}_1) \cdot \mathrm{T}^k(\boldsymbol{T}_2) \middle| j_1', j_2', j', m' \right\rangle \\ &= \delta_{j,j'} \delta_{m,m'} (-1)^{j_1'+j_2+j} \begin{Bmatrix} j_2' & j_1' & j \\ j_1 & j_2 & k \end{Bmatrix} \left\langle j_1 \middle\| \mathrm{T}^k(\boldsymbol{T}_1) \middle\| j_1' \right\rangle \left\langle j_2 \middle\| \mathrm{T}^k(\boldsymbol{T}_2) \middle\| j_2' \right\rangle, \end{aligned} \tag{2.25}$$

where $\boldsymbol{j}_1$ and $\boldsymbol{j}_2$ couple to $\boldsymbol{j}$ and j_1, j_2, j are corresponding quantum numbers.

In molecular spectroscopy, we often need to transform operators from one coordinate system to another. The rotation of spherical tensor components from the space-fixed coordinate system where the components of operators are indicated by p, to the body-fixed system where the components of operators are indicated by q, is,

$$\mathrm{T}^k_p(\boldsymbol{T}) = \sum_q \mathcal{D}^{(k)}_{p,q}(\boldsymbol{\omega})^* \, \mathrm{T}^k_q(\boldsymbol{T}), \tag{2.26}$$

The rotational wavefunction of a symmetric top is used for diatomic molecules,

which is proportional to the conjugate of the Wigner rotation matrix element

$$|J,\Omega,M\rangle = \sqrt{\frac{2J+1}{8\pi^2}}\mathcal{D}^{(J)}_{M,\Omega}(\omega)^*. \tag{2.27}$$

From this equation,

$$\begin{aligned}&\left\langle J,\Omega,M\middle|\mathcal{D}^{(k)}_{p,q}(\omega)^*\middle|J',\Omega',M'\right\rangle \\ =&(-1)^{M-\Omega}\sqrt{(2J+1)(2J'+1)}\begin{pmatrix} J & k & J' \\ -\Omega & q & \Omega' \end{pmatrix}\begin{pmatrix} J & k & J' \\ -M & p & M' \end{pmatrix}.\end{aligned} \tag{2.28}$$

The reduced matrix element of the Wigner rotation matrix is

$$\left\langle J,\Omega,M\middle\|\mathcal{D}^{(k)}_{.q}(\omega)^*\middle\|J',\Omega',M'\right\rangle = (-1)^{J-\Omega}\sqrt{(2J+1)(2J'+1)}\begin{pmatrix} J & k & J' \\ -\Omega & q & \Omega' \end{pmatrix}. \tag{2.29}$$

2.4 The non-relativistic molecular Hamiltonian

If we assume the nuclei and electrons to be point masses, then the non-relativistic Hamiltonian operator of a diatomic molecule is the sum of the kinetic energy of the nuclei, the kinetic energy of the electrons, the potential energy associated the repulsion between the nuclei, the potential energy of the attraction between the electrons and the nuclei, and the potential energy of the repulsion between the electrons, *i.e.*,

$$\begin{aligned}\mathcal{H} = &-\frac{\hbar^2}{2M_a}\boldsymbol{\nabla}_a^2 - \frac{\hbar^2}{2M_b}\boldsymbol{\nabla}_b^2 \\ &+\sum_i -\frac{\hbar^2}{2m_e}\boldsymbol{\nabla}_i^2 \\ &+\frac{Z_a Z_b e^2}{4\pi\varepsilon_0 R} \\ &+\sum_i -\frac{Z_a e^2}{4\pi\varepsilon_0 r_{ai}} + \sum_i -\frac{Z_b e^2}{4\pi\varepsilon_0 r_{bi}} \\ &+\sum_j\sum_{i>j}\frac{e^2}{4\pi\varepsilon_0 r_{ij}},\end{aligned} \tag{2.30}$$

where M_a and M_b are the mass of nucleus a and b, respectively; e is the elementary charge; m_e is the electron mass; i indicates the i-th electron; Z_a and Z_b are the atomic number of the nuclei; ε_0 is the vacuum permittivity; R is the internuclear distance; r_{ai} and r_{bi} are the distances between the nuclei and the i-th electron; r_{ij} is the distance between the i-th and j-th electrons. Bound state energies and wavefunctions are obtained by solving the time-independent Schrödinger equation:

$$\mathcal{H}\psi = E\psi. \tag{2.31}$$

2.5 The separation of nuclear and electronic motion

Electrons are much lighter than nuclei, and thus, move much faster than nuclei. Therefore, we may regard the nuclei as fixed and separate the electron wavefunction and nuclear wavefunction

$$\psi = \psi_{\mathrm{e}}\psi_{\mathrm{n}},$$

following the well-known Born-Oppenheimer (BO) approximation. The electronic Hamiltonian is

$$\mathcal{H}_{\mathrm{e}} = \sum_i -\frac{\hbar^2}{2m_e}\boldsymbol{\nabla}_i^2 + \frac{e^2}{4\pi\varepsilon_0}\left(\frac{Z_a Z_b}{R} + \sum_i -\frac{Z_a}{r_{ai}} + \sum_i -\frac{Z_b}{r_{bi}} + \sum_j \sum_{i>j} \frac{1}{r_{ij}}\right). \tag{2.32}$$

The energy solutions of the electronic Schrödinger equation,

$$\mathcal{H}_{\mathrm{e}}\psi_{\mathrm{e}} = E_{\mathrm{e}}\psi_{\mathrm{e}},$$

are R-dependent curves, *i.e.*, the potential energy curves (PECs) of a diatomic molecule are:

$$E_{\mathrm{e}}(\mathrm{state}) = V_{\mathrm{state}}(R),$$

where the subscript 'state' indicates the electronic states.

The electronic structure of molecules is usually calculated by quantum chemistry programs. When considering relativistic effects, electrons gain one of their

most important properties, spin. Quantum chemistry programs usually treat the electron spin as an extra degree of freedom besides spatial freedoms in Schrödinger equation, rather than solving relativistic quantum equations. The calculated PECs will have both definite spatial symmetry and spin multiplicity.

When the electron spin angular momentum interacts with other angular momenta, extra energy operators are introduced and the degeneracy of electronic states is lifted. These terms include spin-orbit interaction, spin-spin interaction, spin-rotation interaction, *etc.* Quantum chemistry programs can evaluate many of these electron spin interaction operators and generate R-dependent coupling curves involing them.

2.6 Rovibronic fine structure of diatomic molecules

In the absence of an external field, we may solve the Schrödinger equation of nuclear motion in a body-fixed axis system. After separating out the centre-of-mass motion and having introduced a body-fixed set of Cartesian axes with origin at the centre of nuclear mass and with the z-axis along the internuclear direction, the non-relativistic diatomic Hamiltonian can be divided into four parts

$$\mathcal{H} = \mathcal{H}_{\mathrm{e}} + \mathcal{H}_{\mu} + \mathcal{H}_{\mathrm{v}} + \mathcal{H}_{\mathrm{r}}. \tag{2.33}$$

We have discuss the electronic Hamiltonian, $\mathcal{H}_{\mathrm{e}}$, in the previous section. $\mathcal{H}_{\mu}$ is the mass-polarization term given by

$$\mathcal{H}_{\mu} = -\frac{\hbar^2}{2(M_a + M_b)} \sum_{i,j} \boldsymbol{\nabla}_i \cdot \boldsymbol{\nabla}_j. \tag{2.34}$$

(2.35)

$\mathcal{H}_{\mu}$ is usually small and negligible. $\mathcal{H}_{\mathrm{v}}$ and $\mathcal{H}_{\mathrm{r}}$ are the vibrational and rotational Hamiltonians, respectively:

$$\mathcal{H}_{\mathrm{v}} = -\frac{\hbar^2}{2\mu} \frac{\partial^2}{\partial R^2} \tag{2.36}$$

$$\mathcal{H}_{\rm r} = \frac{\hbar^2}{2\mu R^2}\boldsymbol{R}^2, \tag{2.37}$$

where $\boldsymbol{R}$ is the body-fixed nuclear rotation angular momentum.

In diatomic molecular spectroscopy, apart from the BO approximation, another good approximation is that the wavefunctions of nuclear vibration and rotation are separable. Thus, the rotationless Schrödinger equation can be solved independently for each uncoupled potential energy curve $V_{\rm state}(R)$ in the first place, to give reasonable vibrational energy levels, $E_{{\rm state},v}$, and wavefunctions, $\psi_{{\rm state},v}$, of the specific electronic state:

$$\left[-\frac{\hbar^2}{2\mu}\frac{{\rm d}^2}{{\rm d}R^2} + V_{\rm state}(R)\right]\psi_{{\rm state},v}(R) = E_{{\rm state},v}\psi_{{\rm state},v}(R)\,, \tag{2.38}$$

where v indicates the vibrational quantum numbers. This is a one-dimensional ordinary differential secular equation, which can be solved by well-developed numerical algorithms *e.g.*, discrete variable representation (DVR) method.

The rotational terms are usually treated as perturbations of the eigenstates of the vibration. As a consequence, Standard practice for these terms is including them in effective Hamiltonians. However, rigorously, the vibrational and rotational motion cannot be separated. Electronic states also interacts with each other. Effective Hamiltonians are no longer accurate in the region of resonances. The ExoMol group at UCL, thus, proposed variational models and developed a program Duo [42], for variational calculation of spectra of diatomic molecules. In Duo, after solving the vibrational problem Eq.(2.38), a rovibronic Hamiltonian matrix, for each specific total angular momentum exclusive of nuclear spin, J, and parity, τ, is constructed using a Hund's case (a) basis set [48]:

$$|{\rm state},v,\Lambda,S,\Sigma,J,\Omega\rangle = |{\rm state},\Lambda,S,\Sigma\rangle\,|{\rm state},v\rangle\,|J,\Omega,M_J\rangle\,, \tag{2.39}$$

which is decoupled into three parts: (i) the electronic eigenfunction, (ii) the vibrational eigenfunction of Eq. (2.38), and (iii) the rotational eigenfunction of a symmetric top. See Table 2.1 for the meanings of the quantum numbers. Note that, Duo

calculates the spectra of diatomic molecules in field-free environments. Thus, we do not use M_J to construct the basis set, as the left hand side of Eq. (2.39) indicates. All the angular momenta are quantized along the body-fixed axes.

The rovibronic Hamiltonian, denoted as $\mathcal{H}^{(0)}$, includes the necessary couplings, *e.g.*, the spin-orbit interaction. When evaluating the matrix elements using the basis functions of Eq. (2.39), the coupling curves are integrated over pairs of vibrational basis functions:

$$C_{\text{state}',v';\text{state},v} = \langle \text{state}, v \big| C_{\text{state}';\text{state}}(R) \big| \text{state}', v' \rangle , \tag{2.40}$$

where $C(R)$ can be either a diagonal coupling curve for a particular electronic state or an off-diagonal coupling curve between two states.

The basis functions of Eq. (2.39) do not have definite parities. Duo uses linear combinations of them to define parity-conserved basis functions:

$$\begin{aligned} + &: \frac{1}{\sqrt{2}} |\text{state}, v, \Lambda, S, \Sigma, J, \Omega\rangle + \frac{1}{\sqrt{2}} (-1)^{s-\Lambda+S-\Sigma+J-\Omega} |\text{state}, v, -\Lambda, S, -\Sigma, J, -\Omega\rangle , \\ - &: \frac{1}{\sqrt{2}} |\text{state}, v, \Lambda, S, \Sigma, J, \Omega\rangle - \frac{1}{\sqrt{2}} (-1)^{s-\Lambda+S-\Sigma+J-\Omega} |\text{state}, v, -\Lambda, S, -\Sigma, J, -\Omega\rangle , \end{aligned} \tag{2.41}$$

where $s = 1$ for Σ^- states and $s = 0$ for all other states. Note that, the parity is independent of M_J. Each matrix of $\mathcal{H}^{(0)}$ constructed using these basis functions can be diagonalized to give rovibronic energy levels and wavefunctions of a definite J and parity τ. Let $\left|\phi_m^{\tau,J}\right\rangle$ be the m-th eigenfunction corresponding to a given J and parity τ, we have:

$$\left\langle \phi_m^{\tau,J} \middle| \mathcal{H}^{(0)} \middle| \phi_{m'}^{\tau,J} \right\rangle = \delta_{m,m'} E_m^{\tau,J} , \tag{2.42}$$

where $E_m^{\tau,J}$ is the m-th eigenvalue.

Thanks to the use of complete angular basis sets and the variational method, the final energies are independent of the coupling scheme used. If enough vibrational basis functions (determined by the users' setup), the choice of Hund's case (a) will give correct results even for cases where other coupling schemes provide a better zeroth-order approximation.

2.7 The program Duo

Duo is a variational nuclear motion program developed for the calculation of rovibronic spectra of diatomic molecules [42] as part of the ExoMol project [49]. The program LEVEL by Le Roy [50] is also developed for solving the one-dimensional Schrödinger equation. However, it only provides good treatment to closed-shell systems. Duo provides explicit treatment of spin-orbit and other coupling terms and can generate high-accuracy line lists of open-shell diatomic molecules. Duo has been used to generate many line lists including those for AlO [51], CaO [52], VO [53], TiO [54], YO [55], and SiO [56], which are provided via the ExoMol database [25]. Duo was also recently employed to calculate temperature-dependent photodissociation cross sections and rates [57]. Duo has also been adapted to treat ultra-low energy collisions as the inner region in an R-matrix formalism [58]; hyperfine effects are very important in such collisions. Recently, a new module treating electric quadrupole transitions has been added to Duo [59], which makes it capable of predicting spectra for diatomic molecules with no electric dipole moment, *e.g.* O_2 and N_2.

Figure 2.1 demonstrate the procedures to calculate the rovibronic spectra of diatomic molecule in Duo. Notice that a curve refinement module is also implemented which allows users to fit potential energy and other coupling curves with measured values with the aim of achieve experimental accuracy.

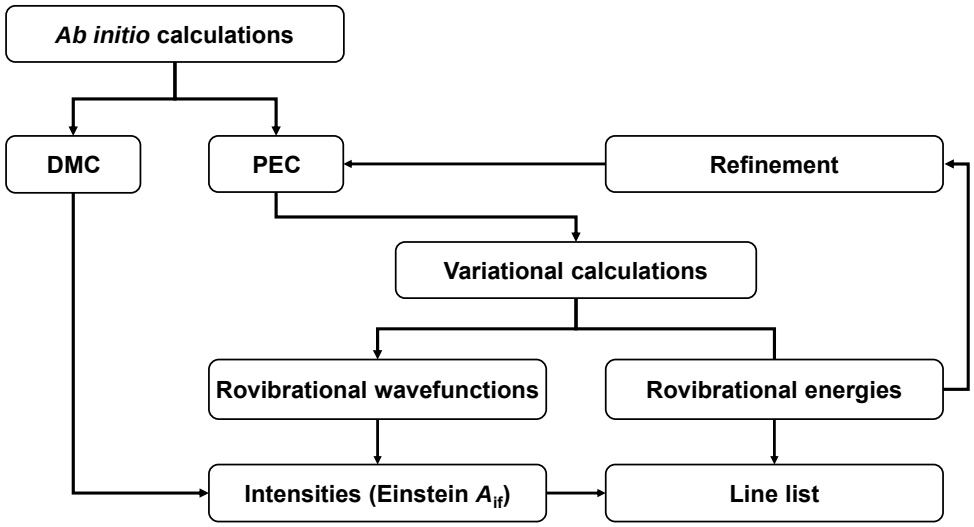

Figure 2.1: Variational calculation of diatomic fine structure. DMC is short for dipole moment curve. PEC is short for potential energy curve.

Chapter 3

Variational Calculation of Hyperfine-resolved Rovibronic Spectra of Diatomic Molecules

3.1 Introduction

The hyperfine structure of molecules lays the foundation for the studies of many important areas. The most immediate application is to reveal the properties of the molecules [60, 61, 62]. Other examples includes laser cooling experiments [63, 64], astronomical observations [65], and, of course, nuclear magnetic resonance which has many applications including ones in medicine.

In the absence of external fields, the rotational hyperfine structure results from interactions between the electric and magnetic multipole moments of the nuclei and their molecular environments [66]. Due to parity conservation inside the nuclei, only even electric and odd magnetic multipoles are non vanishing. Although higher multipole effects are observed in some experiments, the dominant contributions to the hyperfine structure arise from magnetic dipole and electric quadrupole interactions.

Frosch and Foley[67] performed a pioneering theoretical study of the magnetic interactions between nuclei and electron spins in diatomic molecules based on the Dirac equation, see discussion by Brown and Carrington [68]. Bardeen and Townes

[69] provided the first extensive discussion of the electric quadrupole interactions.

The application of irreducible spherical tensor operators facilitate the evaluation of effective hyperfine Hamiltonian matrix elements [70, 66, 71, 72, 68], although one must still pay attention to anomalous commutation relationships when coupling angular momenta [73, 74]. Standard practice is to use these matrix elements to solve problems where hyperfine structure is important using effective Hamiltonians which implicitly use a perturbation theory based representation of the problem [65, 62]. The effective Hamiltonian of a fine or hyperfine problem is usually constructed within a particular vibrational state and the rotational coupling terms are treated as perturbations. The assumptions implicit in this approach are usually valid because the splitting of the (rotational) energy levels due to hyperfine effects are generally small compared to the separation between electronic or vibrational states. However, this assumption can fail, such as for example, for Rydberg states of molecules[75, 76]. The B $^2\Pi$ – C $^2\Pi$ avoided crossing structure in NO is another example of strong electronic state interaction. The perturbative treatment of this vibronic coupling is difficult: it requires a lot of parameters [77], and is not very accurate. The interaction between different states leads to significant complications which are difficult to model using the standard effective Hamiltonian approach.

We present a variational procedure for calculating hyperfine-resolved spectra of diatomic molecules in this chapter. The new algorithm we design is implemented as new modules in Duo. In general, the most challenging part of solving quantum mechanical problems using a variational method is finding good variational basis sets. We show below that Duo gives appropriate basis sets thanks to its well-designed calculation hierarchy and algorithm. Numerical tests indicates that the algorithm proposed here can achieve high accuracy for calculation of hyperfine structure.

3.2 Overview

In this section, we outline our algorithm so that the readers can easily follow the details given in the following sections. Figure 3.1 gives a graphical representation

of the algorithm.

We write the Hamiltonian for the problem as

$$\mathcal{H} = \mathcal{H}^{(0)} + \mathcal{H}_{\text{hfs}}, \tag{3.1}$$

where $\mathcal{H}^{(0)}$ is the rovibronic Hamiltonian which has been discussed in Chapter 2. $\mathcal{H}_{\text{hfs}}$ gives the nuclear hyperfine interaction terms introduced in this chapter. We emphasize that although this structure is the standard one used in perturbation theory, here we aim for a full variational solution of the whole Hamiltonian $\mathcal{H}$.

We program new Duo modules to accomplish the functions denoted by the red rectangles in Fig. 3.1 for nuclear hyperfine structure calculations. We only consider heteronuclear diatomic molecules with one nucleus possessing non-zero spin in this thesis. In this case, nuclear spin, $\boldsymbol{I}$, is coupled with $\boldsymbol{J}$ to give total angular momentum, $\boldsymbol{F}$, *i.e.*,

$$\boldsymbol{F} = \boldsymbol{I} + \boldsymbol{J}. \tag{3.2}$$

To evaluate the matrix elements of $\mathcal{H}_{\text{hfs}}$, we introduce the following primitive basis functions

$$|\text{state}, v, \Lambda, S, \Sigma, J, \Omega, I, F, M_F\rangle = |\text{state}, \Lambda, S, \Sigma\rangle |\text{state}, v\rangle |J, \Omega, M_J\rangle |J, I, F, M_F\rangle, \tag{3.3}$$

where the angular momenta $\boldsymbol{I}$ and $\boldsymbol{F}$ are quantized to the space-fixed axes; $\boldsymbol{J}$ is quantized to both the space-fixed and the body-fixed axes; $\boldsymbol{L}$ and $\boldsymbol{S}$ are quantized to the body-fixed axes. Without an external field, M_F can be omitted:

$$|\text{state}, v, \Lambda, S, \Sigma, J, \Omega, I, F\rangle. \tag{3.4}$$

The basis functions are countable in Duo and thus, can be simply denoted as:

$$|k, J, I, F\rangle = |k, J\rangle |J, I, F\rangle, \tag{3.5}$$

where k is a counting number for the basis functions associated with a given J. It is

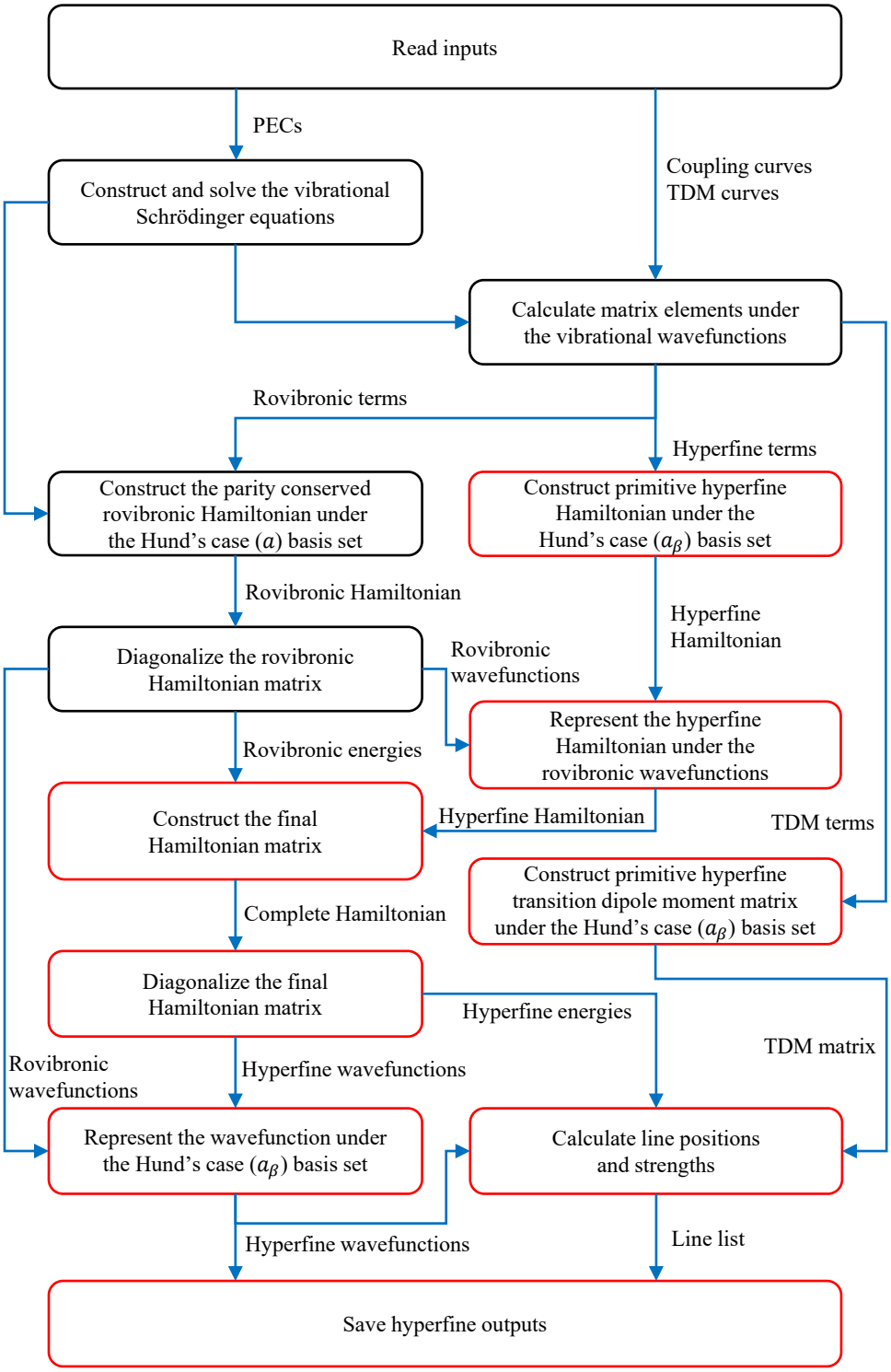

Figure 3.1: Flowchart showing the structure of a Duo hyperfine calculation. Existing modules are given by black rectangles while new modules are denoted by red rectangles. PEC is short for potential energy curve and TDM is short for transition dipole moment.

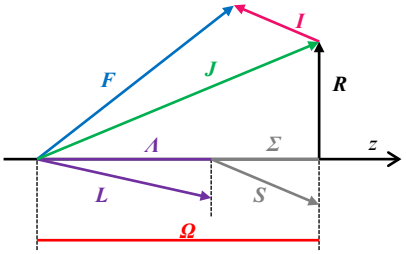

Figure 3.2: Hund's case (a_β) angular momenta coupling scheme. ***R*** is the rotational angular momentum of bare nuclei.

an equivalent representation of Eq. (3.4) and $|k, J\rangle$ is short for Eq. (2.39).

The quantum numbers, J, I and F, satisfy the triangle inequality:

$$|F - I| \leq J \leq F + I. \tag{3.6}$$

The coupling scheme used is known as Hund's case (a_β) [67], and is illustrated in Fig. 3.2. We emphasize that because we use complete angular basis sets, our results are independent of the coupling scheme used and its choice largely becomes one of algorithmic convenience.

To obtain a parity-conserved basis set, we rely on the symmetrization procedure given in Eq. (2.41) by making use of the eigenfunctions obtained as solutions of $\mathcal{H}^{(0)}$, $\left|\phi_m^{\tau,J}\right\rangle$, to define the basis functions:

$$\left|\phi_m^{\tau,J}, I, F\right\rangle = \left|\phi_m^{\tau,J}\right\rangle |J, I, F\rangle\,. \tag{3.7}$$

The parity-conserved rovibronic basis functions, Eq. (3.7), can be represented by the primitive basis functions, Eq. (3.4) or Eq. (3.5)

$$\begin{aligned}\left|\phi_m^{\tau,J}, J, I, F\right\rangle &= \left(\sum_{k,J_1} |k, J_1, I, F\rangle\langle k, J_1, I, F|\right)\left|\phi_m^{\tau,J}, J, I, F\right\rangle \\ &= \sum_k \left\langle k, J\middle|\phi_m^{\tau,J}\right\rangle |k, J, I, F\rangle\,,\end{aligned} \tag{3.8}$$

where the coefficients, $\left\langle k, J\middle|\phi_m^{\tau,J}\right\rangle$, have been obtained when calculating rovibronic fine structure by solving for $\mathcal{H}^{(0)}$. The matrix elements of $\mathcal{H}^{(0)}$ in this basis func-

tions are straightforward

$$\left\langle \phi_m^{\tau,J}, I, F \middle| \mathcal{H}^{(0)} \middle| \phi_{m'}^{\tau,J'}, I, F \right\rangle = \delta_{m,m'}\ \delta_{J,J'}\ E_m^{\tau,J}. \tag{3.9}$$

Therefore constructing the hyperfine-resolved matrix elements

$$\left\langle \phi_m^{\tau,J}, I, F \middle| \mathcal{H}^{(0)} + \mathcal{H}_{\text{hfs}} \middle| \phi_{m'}^{\tau,J'}, I, F \right\rangle,$$

just requires the matrix elements of $\mathcal{H}_{\text{hfs}}$, $\left\langle \phi_m^{\tau,J}, I, F \middle| \mathcal{H}_{\text{hfs}} \middle| \phi_{m'}^{\tau,J'}, I, F \right\rangle$.

In practice, we first construct the matrix elements of $\mathcal{H}_{\text{hfs}}$ using the primitive basis functions of Eq. (3.4) and then transform to the representation of $\mathcal{H}^{(0)}$ of Eq. (3.7) using a basis transformation. The mathematical and physical details are discussed in the next two sections. Before that, we outline the algorithm used to calculate hyperfine-resolved spectra.

As a first step, the hyperfine coupling curves, such as the Fermi contact interaction curves [78], are integrated over the vibrational wavefunctions. Duo uses these vibrational matrix elements to compute the hyperfine matrix elements within a Hund's case (a_β) basis set, Eq. (3.4), and constructs a Hamiltonian matrix for each specific total angular momentum, F. Next, the matrix, corresponding to $\mathcal{H}_{\text{hfs}}$ is constructed in the representation of Eq. (3.7). After this step, the hyperfine matrix elements are parity conserved. Combining the rovibronic energies and hyperfine matrix elements, Duo constructs the complete Hamlitonian matrix, corresponding to $\mathcal{H}$, for each given value of F and τ. Diagonalizing this matrix gives the hyperfine-resolved energy levels and corresponding wavefunctions in the representation of Eq. (3.7). Finally, the eigenfunctions are transformed back to the Hund's case (a_β) representation of Eq. (3.4) as this representation is more convenient to use for hyperfine-resolved intensity calculations, for analysis of wavefunctions and to assign quantum numbers to hyperfine states.

3.3 The hyperfine structure Hamiltonian

We investigate the field-free hyperfine structure of diatomic molecules in which only one of the nuclei possess nuclear spin, and consider five nuclear hyperfine terms:

$$\mathcal{H}_{\text{hfs}} = \mathcal{H}_{\text{FC}} + \mathcal{H}_{\text{IL}} + \mathcal{H}_{\text{dip}} + \mathcal{H}_{\text{IJ}} + \mathcal{H}_{\text{EQ}}. \tag{3.10}$$

They are, respectively, the Hamiltonians of the Fermi contact interaction, the nuclear spin-orbit interaction, the nuclear-spin–electron-spin dipole-dipole interaction, the nuclear-spin–rotation interaction and the nuclear electric quadrupole interaction. These Hamiltonians have the following definitions [68, 72]:

$$\mathcal{H}_{\text{FC}} = \sum_i \frac{8\pi}{3} g_S\, g_N \mu_B \mu_N \frac{\mu_0}{4\pi} \delta(\boldsymbol{r}_{1i}) \boldsymbol{I} \cdot \boldsymbol{S}_i, \tag{3.11}$$

$$\mathcal{H}_{\text{IL}} = \sum_i 2 g_N \mu_B \mu_N \frac{\mu_0}{4\pi} \frac{\boldsymbol{I} \cdot \boldsymbol{L}_i}{r_{1i}^3}, \tag{3.12}$$

$$\mathcal{H}_{\text{dip}} = \sum_i g_S\, g_N \mu_B \mu_N \frac{\mu_0}{4\pi} \left[\frac{\boldsymbol{S}_i \cdot \boldsymbol{I}}{r_{1i}^3} - \frac{3(\boldsymbol{S}_i \cdot \boldsymbol{r}_{1i})(\boldsymbol{I} \cdot \boldsymbol{r}_{1i})}{r_{1i}^5} \right], \tag{3.13}$$

$$\mathcal{H}_{\text{IJ}} = c_I(R) \boldsymbol{I} \cdot \boldsymbol{J}, \tag{3.14}$$

$$\mathcal{H}_{\text{EQ}} = \sum_{i,n} -\frac{e^2}{4\pi\epsilon_0} \frac{r_n^2}{r_i^3} \sum_p (-1)^p C_p^{(2)}(\theta_i, \phi_i) C_{-p}^{(2)}(\theta_n, \phi_n). \tag{3.15}$$

The constants, e, g_S, μ_B, g_N, μ_N and μ_0, are the elementary charge, the free electron spin g-factor, the electron Bohr magneton, the nuclear spin g-factor, the nuclear magneton and the vacuum permeability, respectively. $\boldsymbol{I}$ is the spin of the nucleus of interest (defined as nucleus 1), $\boldsymbol{r}_{1i}$ is the relative position between the i-th electron and nucleus 1, $\boldsymbol{S}_i$ is the spin of the i-th electron, $\boldsymbol{L}_i$ is the orbit angular momentum of the i-th electron, and $\delta(\cdot)$ is the Dirac delta function. In Eq. (3.14), we introduce the nuclear spin-rotation interaction constant, $c_I(R)$, which is a function of internuclear distance. Section 8.2.2(d) of Brown and Carrington [68] and Miani and Tennyson [79] define the nuclear spin-rotation tensor and how it can be reduced to a constant for a diatomic molecule. In Eq. (3.15), $C_p^{(2)}$ is the modified rank-2 spherical

harmonic:

$$C_p^{(2)}(\theta,\phi) = \sqrt{\frac{4\pi}{5}}\, Y_p^{(2)}(\theta,\phi). \tag{3.16}$$

where $Y_p^{(2)}(\theta,\phi)$ is the standard spherical harmonic; (r_i,θ_i,ϕ_i) and (r_n,θ_n,ϕ_n) are the positions of the i-th electron and the n-th proton, respectively.

The first four hyperfine Hamiltonians, given by Eqs. (3.11) – (3.14), are nuclear magnetic dipole terms resulting from the interactions between the magnetic dipole moment given by nuclear spin and magnetic fields due to the motion of nuclei or electrons. The nuclear electric quadrupole Hamiltonian arises from the interaction between the nuclear electric quadrupole moment and the electric field inside a molecule. The nuclear spin-rotation interaction is usually much weaker than the other four hyperfine terms (if non-zero). See Table 1 of Broyer *et al.* [71] for the order of magnitude of the hyperfine terms.

To aid the evaluation of matrix elements, the hyperfine Hamiltonians can be written as scalar products of irreducible tensor operators [68]:

$$\mathcal{H}_{\rm FC} = \sum_i \frac{8\pi}{3} g_S\, g_N \mu_B \mu_N \frac{\mu_0}{4\pi} \delta(\boldsymbol{r}_{1i}) \mathrm{T}^1(\boldsymbol{I}) \cdot \mathrm{T}^1(\boldsymbol{S}_i), \tag{3.17}$$

$$\mathcal{H}_{\rm IL} = \sum_i 2\, g_N \mu_B \mu_N \frac{\mu_0}{4\pi} \frac{1}{r_{1i}^3} \mathrm{T}^1(\boldsymbol{I}) \cdot \mathrm{T}^1(\boldsymbol{L}_i), \tag{3.18}$$

$$\mathcal{H}_{\rm dip} = \sum_i -\sqrt{10}\, g_S\, g_N \mu_B \mu_N \frac{\mu_0}{4\pi} \mathrm{T}^1(\boldsymbol{I}) \cdot \mathrm{T}^1(\boldsymbol{S}_i, \boldsymbol{C}^{(2)}), \tag{3.19}$$

$$\mathcal{H}_{\rm IJ} = c_I(R) \mathrm{T}^1(\boldsymbol{I}) \cdot \mathrm{T}^1(\boldsymbol{J}), \tag{3.20}$$

$$\mathcal{H}_{\rm EQ} = -e\mathrm{T}^2(\boldsymbol{\nabla E}) \cdot \mathrm{T}^2(\boldsymbol{Q}), \tag{3.21}$$

where $\mathrm{T}^k(\cdot)$ indicates a rank-k tensor. All the tensors here are defined in space-fixed frame. The two tensors in Eq. (3.21) defining the gradient of electric field and the nuclear quadrupole moment are, respectively:

$$\mathrm{T}^2(\boldsymbol{\nabla E}) = -\frac{1}{4\pi\varepsilon_0} \sum_i \frac{e}{r_i^3} \boldsymbol{C}^{(2)}(\theta_i,\phi_i), \tag{3.22}$$

$$e\mathrm{T}^2(\boldsymbol{Q}) = e \sum_n r_n^2 \boldsymbol{C}^{(2)}(\theta_n,\phi_n). \tag{3.23}$$

3.4 Matrix elements of the hyperfine structure

3.4.1 Primitive matrix elements of the hyperfine structure

In this section, primitive matrix elements of the hyperfine structure are initially evaluated in the representation of Eq. (3.4). We do not consider hyperfine couplings between different electronic states when evaluating primitive matrix elements, which are, thus, diagonal in the electronic state and electron spin, *i.e.*,

$$\text{state} = \text{state}', \quad S = S',$$

in the bra-ket notation, and immediately we have

$$|\Lambda| = \left|\Lambda'\right|.$$

As $\boldsymbol{F} = \boldsymbol{J} + \boldsymbol{I}$, we can initially decouple the representation of $|J, I, F, M_F\rangle$ in Eq. (3.3) to uncoupled ones. Taking the Fermi contact term as an example, the non-vanishing matrix element on the primitive basis functions for $M_F = M_F'$ is

$$\begin{aligned}
&\langle \text{state}, v, \Lambda, S, \Sigma, J, \Omega, I, F \left| \mathcal{H}_{\text{FC}} \right| \text{state}, v', \Lambda', S, \Sigma', J', \Omega', I, F \rangle \\
&= (-1)^{J'+F+I} \begin{Bmatrix} I & J' & F \\ J & I & 1 \end{Bmatrix} \left\langle I \middle\| \mathrm{T}^1(\boldsymbol{I}) \middle\| I \right\rangle \times \frac{8\pi}{3} g_S \, g_N \mu_B \mu_N \frac{\mu_0}{4\pi} \\
&\quad \times \left\langle \text{state}, v, \Lambda, S, \Sigma, J, \Omega \middle\| \sum_i \delta(\boldsymbol{r}_{1i}) \mathrm{T}^1(\boldsymbol{S}_i) \middle\| \text{state}, v', \Lambda', S, \Sigma', J', \Omega' \right\rangle, \qquad (3.24)
\end{aligned}$$

where $\begin{Bmatrix} j_1 & j_2 & j_3 \\ j_4 & j_5 & j_6 \end{Bmatrix}$ is the Wigner-6j symbol. The projection of nuclear spin is quantized to the space-fixed axes, and thus, the reduced matrix element of $\mathrm{T}^1(\boldsymbol{I})$ is

$$\left\langle I \middle\| \mathrm{T}^1(\boldsymbol{I}) \middle\| I \right\rangle = \sqrt{I(I+1)(2I+1)}. \qquad (3.25)$$

The projection of electron spin is quantized to the body-fixed axes. To evaluate the second reduced matrix element in Eq. (3.24), the electron spin spherical tensor is

rotated from the space-fixed frame to the body-fixed frame in which the components of tensors are denoted by q:

$$\begin{aligned}
&\left\langle \text{state}, v, \Lambda, S, \Sigma, J, \Omega \middle\| \sum_i \delta(\boldsymbol{r}_{1i})\, \mathrm{T}^1(\boldsymbol{S}_i) \middle\| \text{state}, v', \Lambda', S, \Sigma', J', \Omega' \right\rangle \\
&= \left\langle \text{state}, v, \Lambda, S, \Sigma, J, \Omega \middle\| \sum_i \delta(\boldsymbol{r}_{1i}) \sum_q \mathcal{D}^{(1)}_{\cdot q}(\boldsymbol{\omega})^*\, \mathrm{T}^1_q(\boldsymbol{s}_i) \middle\| \text{state}, v', \Lambda', S, \Sigma', J', \Omega' \right\rangle \\
&= \sum_q (-1)^{J-\Omega} \begin{pmatrix} J & 1 & J' \\ -\Omega & q & \Omega' \end{pmatrix} \sqrt{(2J+1)(2J'+1)}\, \delta_{\Lambda,\Lambda'} \\
&\quad \times \left\langle \text{state}, v \middle| \left\langle \text{state}, \Lambda, S, \Sigma \middle| \sum_i \delta(\boldsymbol{r}_{1i})\, \mathrm{T}^1_q(\boldsymbol{s}_i) \middle| \text{state}, \Lambda', S, \Sigma' \right\rangle \middle| \text{state}, v' \right\rangle, \qquad (3.26)
\end{aligned}$$

where $\boldsymbol{s}_i$ is the spin of the i-th electron in the body-fixed system, $\mathcal{D}^{(k)}_{m',m}(\boldsymbol{\omega})$ is a Wigner rotation matrix and $\begin{pmatrix} j_1 & j_2 & j_3 \\ m_1 & m_2 & m_3 \end{pmatrix}$ is a Wigner-3j symbol. The electron tensor operators, $\mathrm{T}^1_q(\boldsymbol{s}_i)$, do not directly act on the electronic part of Hund's case (a) basis. We may replace the electron spin operators with an effective one:

$$\begin{aligned}
&\frac{8\pi}{3}\, g_S\, g_N \mu_B \mu_N \frac{\mu_0}{4\pi} \left\langle \text{state}, \Lambda, S, \Sigma \middle| \sum_i \delta(\boldsymbol{r}_{1i})\, \mathrm{T}^1_q(\boldsymbol{s}_i) \middle| \text{state}, \Lambda, S, \Sigma' \right\rangle \\
&= \left\langle \text{state}, \Lambda, S, \Sigma \middle| b_{\mathrm{F}}(R)\, \mathrm{T}^1_q(\boldsymbol{S}) \middle| \text{state}, \Lambda, S, \Sigma' \right\rangle, \qquad (3.27)
\end{aligned}$$

where $\boldsymbol{S}$ is the total spin. Requiring $\Sigma = \Sigma'$, the Fermi contact interaction curve can be defined as [78]:

$$b_{\mathrm{F}}(R) = \frac{8\pi}{3}\, g_S\, g_N \mu_B \mu_N \frac{\mu_0}{4\pi} \left\langle \text{state}, \Lambda, S, \Sigma \middle| \sum_i \delta(\boldsymbol{r}_{1i}) \frac{\mathrm{T}^1_0(\boldsymbol{s}_i)}{\Sigma} \middle| \text{state}, \Lambda, S, \Sigma \right\rangle, \qquad (3.28)$$

where $\mathrm{T}^1_0(\boldsymbol{s}_i)/\Sigma$ represents the projection operator for each electron i (see Eq. (7.152) of Brown and Carrington [68]). Based on Eqs. (3.24) to (3.28), we finally get:

$$\langle \text{state}, v, \Lambda, S, \Sigma, J, \Omega, I, F \big| \mathcal{H}_{\mathrm{FC}} \big| \text{state}, v', \Lambda', S, \Sigma', J', \Omega', I, F \rangle$$

$$
\begin{aligned}
&= (-1)^{J'+F+I} \begin{Bmatrix} I & J' & F \\ J & I & 1 \end{Bmatrix} \sqrt{I(I+1)(2I+1)} \ldots \\
&\times \left[\sum_q (-1)^{J-\Omega} \begin{pmatrix} J & 1 & J' \\ -\Omega & q & \Omega' \end{pmatrix} \sqrt{(2J+1)(2J'+1)} \ldots \right. \\
&\times (-1)^{S-\Sigma} \begin{pmatrix} S & 1 & S \\ -\Sigma & q & \Sigma' \end{pmatrix} \sqrt{S(S+1)(2S+1)} \ldots \\
&\left. \times \delta_{\Lambda,\Lambda'} \left\langle \text{state}, v \middle| b_{\mathrm{F}}(R) \middle| \text{state}, v' \right\rangle \right]. \qquad (3.29)
\end{aligned}
$$

Other hyperfine matrix elements can be evaluated analogusly.

For the nuclear spin-orbit term, we are only interested in the diagonal matrix elements of Λ

$$
\begin{aligned}
&\left\langle \text{state}, v, \Lambda, S, \Sigma, J, \Omega, I, F \middle| \mathcal{H}_{\mathrm{IL}} \middle| \text{state}, v', \Lambda, S, \Sigma', J', \Omega', I, F \right\rangle \\
&= (-1)^{J'+F+I} \begin{Bmatrix} I & J' & F \\ J & I & 1 \end{Bmatrix} \sqrt{I(I+1)(2I+1)} \ldots \\
&\times (-1)^{J-\Omega} \begin{pmatrix} J & 1 & J' \\ -\Omega & 0 & \Omega \end{pmatrix} \sqrt{(2J+1)(2J'+1)} \ldots \\
&\times \delta_{\Sigma,\Sigma'} \Lambda \left\langle \text{state}, v \middle| a(R) \middle| \text{state}, v' \right\rangle. \qquad (3.30)
\end{aligned}
$$

The non-diagonal couplings between different electronic states via $\mathrm{T}^1_{\pm 1}(\boldsymbol{L})$ are not considered here. The diagonal nuclear-spin–orbit interaction curve is defined as [78]:

$$
a(R) = 2 g_N \mu_B \mu_N \frac{\mu_0}{4\pi} \left\langle \text{state}, \Lambda, S, \Sigma \middle| \sum_i \frac{1}{r_{1i}^3} \frac{\mathrm{T}^1_0(\boldsymbol{l}_i)}{\Lambda} \middle| \text{state}, \Lambda, S, \Sigma \right\rangle, \qquad (3.31)
$$

where $\boldsymbol{l}_i$ is the orbital angular momentum of the i-th electron defined in the body-fixed frame.

The nuclear spin-electron spin dipole-dipole interaction is somewhat compli-

cated. With the definition (see Appendix 8.2 of Brown and Carrington [68]):

$$\mathrm{T}^1_q(\boldsymbol{s}_i, \boldsymbol{C}^{(2)}) = \sum_{q_1,q_2} -\sqrt{3}(-1)^q \mathrm{T}^1_{q_1}(\boldsymbol{s}_i) \frac{C^{(2)}_{q_2}(\theta_{1i},\phi_{1i})}{r^3_{1i}} \begin{pmatrix} 1 & 2 & 1 \\ q_1 & q_2 & -q \end{pmatrix}, \tag{3.32}$$

where $(r_{1i}, \theta_{1,i}, \phi_{1,i})$ are the spherical polar coordinates of electron i relative to nucleus 1, we shall give two kinds of matrix elements. For the term diagonal in Λ, *i.e.* $q_2 = 0$ and $q = q_1$:

$$\begin{aligned}
&\left\langle \text{state}, v, \Lambda, S, \Sigma, J, \Omega, I, F \middle| \mathcal{H}_{\text{dip}} \middle| \text{state}, v', \Lambda, S, \Sigma', J', \Omega', I, F \right\rangle \\
&= (-1)^{J'+F+I} \begin{Bmatrix} I & J' & F \\ J & I & 1 \end{Bmatrix} \sqrt{I(I+1)(2I+1)} \ldots \\
&\quad \times \left[\sum_q (-1)^{J-\Omega} \begin{pmatrix} J & 1 & J' \\ -\Omega & q & \Omega' \end{pmatrix} \sqrt{(2J+1)(2J'+1)} \ldots \right. \\
&\qquad \times (-1)^q \sqrt{30} \begin{pmatrix} 1 & 2 & 1 \\ q & 0 & -q \end{pmatrix} (-1)^{S-\Sigma} \begin{pmatrix} S & 1 & S \\ -\Sigma & q & \Sigma' \end{pmatrix} \sqrt{S(S+1)(2S+1)} \ldots \\
&\qquad \left. \times \frac{1}{3} \left\langle \text{state}, v \middle| c(R) \middle| \text{state}, v' \right\rangle \right],
\end{aligned} \tag{3.33}$$

The diagonal nuclear-spin–electron-spin dipole-dipole interaction constant curve is defined as [78],

$$c(R) = 3\, g_S\, g_N \mu_B \mu_N \frac{\mu_0}{4\pi} \left\langle \text{state}, \Lambda, S, \Sigma \middle| \sum_i \frac{C^{(2)}_0(\theta_{1i},\phi_{1i})}{r^3_{1i}} \frac{\mathrm{T}^1_0(\boldsymbol{s}_i)}{\Sigma} \middle| \text{state}, \Lambda, S, \Sigma \right\rangle. \tag{3.34}$$

For the off-diagonal terms of $\mathcal{H}_{\text{dip}}$ in Λ and Λ' which satisfy $q_2 = \mp 2$, *i.e.* $q_1 = \pm 1$ and $q = \mp 1$, we have

$$\begin{aligned}
&\left\langle \text{state}, v, \Lambda, S, \Sigma, J, \Omega, I, F \middle| \mathcal{H}_{\text{dip}} \middle| \text{state}, v', \Lambda', S, \Sigma', J', \Omega', I, F \right\rangle \\
&= (-1)^{J'+F+I} \begin{Bmatrix} I & J' & F \\ J & I & 1 \end{Bmatrix} \sqrt{I(I+1)(2I+1)} \ldots
\end{aligned}$$

$$\times(-1)^{J-\Omega}\begin{pmatrix} J & 1 & J' \\ -\Omega & \mp 1 & \Omega' \end{pmatrix}\sqrt{(2J+1)(2J'+1)}\,\ldots$$
$$\times\frac{\sqrt{S(S+1)-\Sigma(\Sigma\pm 1)}}{\mp\sqrt{2}}\left\langle \text{state}, v\middle|d(R)\middle|\text{state}, v'\right\rangle, \tag{3.35}$$

The off-diagonal nuclear-spin–electron-spin dipole-dipole interaction constant curve is defined as [78],

$$d(R) = -\sqrt{6}\,g_S\,g_N\mu_B\mu_N\frac{\mu_0}{4\pi}\ldots$$
$$\times\left\langle \text{state}, \Lambda, S, \Sigma\middle|\sum_i \frac{C^{(2)}_{\mp 2}(\theta_{1i},\phi_{1i})}{r^3_{1i}}\frac{\mp\sqrt{2}\,\mathrm{T}^1_{\pm 1}(\boldsymbol{s}_i)}{\sqrt{S(S+1)-\Sigma(\Sigma\pm 1)}}\middle|\text{state}, \Lambda', S, \Sigma'\right\rangle. \tag{3.36}$$

The case of the nuclear spin-rotation interaction is much simpler, as it is not necessary to rotate $\mathrm{T}^1(\boldsymbol{J})$ to the body-fixed axis system:

$$\left\langle \text{state}, v, \Lambda, S, \Sigma, J, \Omega, I, F\middle|\mathcal{H}_{\mathrm{IJ}}\middle|\text{state}, v', \Lambda', S, \Sigma', J', \Omega', I, F\right\rangle$$
$$=(-1)^{J'+F+I}\begin{Bmatrix} I & J' & F \\ J & I & 1 \end{Bmatrix}\sqrt{I(I+1)(2I+1)}\,\ldots$$
$$\times(-1)^{J-\Omega}\begin{pmatrix} J & 1 & J' \\ -\Omega & 0 & \Omega \end{pmatrix}\delta_{\Lambda,\Lambda'}\,\delta_{\Sigma,\Sigma'}\,\delta_{J,J'}\,\sqrt{J(J+1)(2J+1)}\,\ldots$$
$$\times\left\langle \text{state}, v\middle|c_I(R)\middle|\text{state}, v'\right\rangle. \tag{3.37}$$

To evaluate the matrix elements for the electric quadrupole interaction, we decouple the inner product of second rank irreducible tensors:

$$\left\langle \text{state}, v, \Lambda, S, \Sigma, J, \Omega, I, F\middle|\mathcal{H}_{\mathrm{EQ}}\middle|\text{state}, v', \Lambda', S, \Sigma', J', \Omega', I, F\right\rangle$$
$$=(-1)^{J'+I+F}\begin{Bmatrix} I & J & F \\ J' & I & 2 \end{Bmatrix}\left\langle I\middle\|-e\mathrm{T}^2(\boldsymbol{Q})\middle\|I\right\rangle\ldots$$
$$\times\left\langle \text{state}, v, \Lambda, S, \Sigma, J, \Omega\middle\|\mathrm{T}^2(\boldsymbol{\nabla E})\middle\|\text{state}, v', \Lambda', S, \Sigma', J', \Omega'\right\rangle. \tag{3.38}$$

The electric quadrupole reduced matrix element is non-zero only if $I \geq 1$; it can be evaluated as

$$\left\langle I \middle\| -e\mathrm{T}^2(\boldsymbol{Q}) \middle\| I \right\rangle = \frac{-eQ}{2} \begin{pmatrix} I & 2 & I \\ -I & 0 & I \end{pmatrix}^{-1} . \tag{3.39}$$

where eQ is the nuclear electric quadrupole moment, see Cook and De Lucia [66] or Appendix 8.4 of Brown and Carrington [68]. The values of Q for various atoms were collected by Pyykkö [80]. The reduced matrix element of the gradient of electric field is

$$\begin{aligned} &\left\langle \text{state}, v, \Lambda, S, \Sigma, J, \Omega \middle\| \mathrm{T}^2(\boldsymbol{\nabla E}) \middle\| \text{state}, v', \Lambda', S, \Sigma', J', \Omega' \right\rangle \\ &= \sum_q (-1)^{J-\Omega} \begin{pmatrix} J & 2 & J' \\ -\Omega & q & \Omega' \end{pmatrix} \sqrt{(2J+1)(2J'+1)}\, \delta_{\Sigma,\Sigma'} \ldots \\ &\times \left\langle \text{state}, v \middle| \left\langle \text{state}, \Lambda, S, \Sigma \middle| \mathrm{T}^2_q(\boldsymbol{\nabla E}) \middle| \text{state}, \Lambda', S, \Sigma' \right\rangle \middle| \text{state}, v' \right\rangle . \end{aligned} \tag{3.40}$$

The diagonal and off-diagonal R-dependent constants of the gradient of electric field are respectively defined as (see Eqs. (7.159) and (7.163) of Brown and Carrington [68]):

$$q_0(R) = -2 \left\langle \text{state}, \Lambda, S, \Sigma \middle| \mathrm{T}^2_0(\boldsymbol{\nabla E}) \middle| \text{state}, \Lambda, S, \Sigma \right\rangle, \tag{3.41}$$

$$q_2(R) = -2\sqrt{6} \left\langle \text{state}, \Lambda, S, \Sigma \middle| \mathrm{T}^2_{\pm 2}(\boldsymbol{\nabla E}) \middle| \text{state}, \Lambda', S, \Sigma \right\rangle . \tag{3.42}$$

Note that sometimes q_0 is denoted as q_1, see *e.g.* Eq. (2.3.76 a) of Hirota [81]. We follow the convention of Brown and Carrington [68] and preserve the variable q_1 for the nuclear electric quadrupole coupling constant between different electronic states arising from $\mathrm{T}^2_{\pm 1}(\boldsymbol{\nabla E})$ which will be the subject of future work. Finally, the diagonal matrix elements of nuclear electric quadrupole coupling are

$$\left\langle \text{state}, v, \Lambda, S, \Sigma, J, \Omega, I, F \middle| \mathcal{H}_{\mathrm{EQ}} \middle| \text{state}, v', \Lambda', S, \Sigma', J', \Omega', I, F \right\rangle$$

$$
\begin{aligned}
&= (-1)^{J'+I+F} \begin{Bmatrix} I & J & F \\ J' & I & 2 \end{Bmatrix} \begin{pmatrix} I & 2 & I \\ -I & 0 & I \end{pmatrix}^{-1} \cdots \\
&\times (-1)^{J-\Omega} \begin{pmatrix} J & 2 & J' \\ -\Omega & 0 & \Omega \end{pmatrix} \sqrt{(2J+1)(2J'+1)}\, \delta_{\Sigma,\Sigma'}\, \delta_{\Lambda,\Lambda'} \cdots \\
&\times \frac{1}{4} \left\langle \text{state}, v \middle| eQq_0(R) \middle| \text{state}, v' \right\rangle ,
\end{aligned} \tag{3.43}
$$

while the off-diagonal ones are:

$$
\begin{aligned}
&\left\langle \text{state}, v, \Lambda, S, \Sigma, J, \Omega, I, F \middle| \mathcal{H}_{\text{EQ}} \middle| \text{state}, v', \Lambda', S, \Sigma', J', \Omega', I, F \right\rangle \\
&= (-1)^{J'+I+F} \begin{Bmatrix} I & J & F \\ J' & I & 2 \end{Bmatrix} \begin{pmatrix} I & 2 & I \\ -I & 0 & I \end{pmatrix}^{-1} \cdots \\
&\times (-1)^{J-\Omega} \begin{pmatrix} J & 2 & J' \\ -\Omega & \pm 2 & \Omega' \end{pmatrix} \sqrt{(2J+1)(2J'+1)}\, \delta_{\Sigma,\Sigma'} \cdots \\
&\times \frac{1}{4\sqrt{6}} \left\langle \text{state}, v \middle| eQq_2(R) \middle| \text{state}, v' \right\rangle .
\end{aligned} \tag{3.44}
$$

As we only consider the hyperfine interactions within a particular electronic state in this thesis, the off-diagonal matrix elements arising from $d(R)$ in Eq. (3.36) and $q_2(R)$ in Eq. (3.42) only contribute to the Λ - doubling terms of Π states.

3.4.2 Parity conserved matrix elements under the rovibronic wavefunctions

Recall the short notation of Hund's case (a_β) basis in Eq. (3.5), $|k, J, I, F\rangle$ and the basis functions we defined in Eq. (3.7), $\left|\phi_m^{\tau,J}, I, F\right\rangle$, the hyperfine matrix elements under the basis set can be expanded as

$$
\begin{aligned}
&\left\langle \phi_m^{\tau,J}, I, F \middle| \mathcal{H}_{\text{hfs}} \middle| \phi_{m'}^{\tau,J'}, I, F \right\rangle \\
&= \left\langle \phi_m^{\tau,J}, I, F \middle| \left(\sum_{k,J_1} |k, J_1, I, F\rangle\langle k, J_1, I, F| \right) \mathcal{H}_{\text{hfs}} \left(\sum_{k',J_2} |k', J_2, I, F\rangle\langle k', J_2, I, F| \right) \middle| \phi_{m'}^{\tau,J'}, I, F \right\rangle \\
&= \sum_{k,J_1} \sum_{k',J_2} \left\langle \phi_m^{\tau,J}, I, F \middle| k, J_1, I, F \right\rangle \left\langle k, J_1, I, F \middle| \mathcal{H}_{\text{hfs}} \middle| k', J_2, I, F \right\rangle \left\langle k', J_2, I, F \middle| \phi_{m'}^{\tau,J'}, I, F \right\rangle
\end{aligned}
$$

$$= \sum_k \sum_{k'} \left\langle \phi_m^{\tau,J}, I, F \middle| k, J, I, F \right\rangle \langle k, J, I, F | \mathcal{H}_{\rm hfs} | k', J', I, F \rangle \left\langle k', J', I, F \middle| \phi_{m'}^{\tau,J'}, I, F \right\rangle . \tag{3.45}$$

We can rewrite the basis transformation into the matrix format:

$$\boldsymbol{H}_{\rm hfs}^{\tau,F} = \left(\boldsymbol{\Phi}^{\tau,F}\right)^{\dagger} \boldsymbol{H}_{\rm hfs}^{F} \boldsymbol{\Phi}^{\tau,F} . \tag{3.46}$$

$\left\langle \phi_m^{\tau,J}, I, F \middle| \mathcal{H}_{\rm hfs} \middle| \phi_{m'}^{\tau,J'}, I, F \right\rangle$, $\langle k, J, I, F | \mathcal{H}_{\rm hfs} | k', J', I, F \rangle$ and $\left\langle k', J', I, F \middle| \phi_{m'}^{\tau,J'}, I, F \right\rangle$ are the matrix elements of $\boldsymbol{H}_{\rm hfs}^{\tau,F}$, $\boldsymbol{H}_{\rm hfs}^{F}$ and $\boldsymbol{\Phi}^{\tau,F}$, respectively, and,

$$\left\langle k', J', I, F \middle| \phi_{m'}^{\tau,J'}, I, F \right\rangle = \left\langle k', J' \middle| \phi_{m'}^{\tau,J'} \right\rangle .$$

3.4.3 Solution for the hyperfine structure

The final Hamiltonian which is constructed from summation of the rovibronic and hyperfine matrices

$$\boldsymbol{H}^{\tau,F} = \boldsymbol{H}^{(0),\tau,F} + \boldsymbol{H}_{\rm hfs}^{\tau,F}, \tag{3.47}$$

where $\boldsymbol{H}^{(0),\tau,F}$ is the matrix of $\mathcal{H}^{(0)}$ (see Eq. (3.9) for the matrix elements). Diagonalizing the parity-conserved matrix of each F results in the energies and wavefunctions associated with the hyperfine structure:

$$\boldsymbol{E}^{\tau,F} = \left(\boldsymbol{U}^{\tau,F}\right)^{\dagger} \boldsymbol{H}^{\tau,F} \boldsymbol{U}^{\tau,F} . \tag{3.48}$$

The eigenfunction matrix $\boldsymbol{U}^{\tau,F}$ is represented in the parity-conserved rovibronic basis set defined in Eq. (3.7), which is, however, not very useful for quantum number assignments and wavefunction analysis. For these purposes, the wavefunctions can be transformed back in the representation of Hund's case (a) basis set and the final wavefunction matrix is

$$\boldsymbol{\Psi}^{\tau,F} = \boldsymbol{\Phi}^{\tau,F} \boldsymbol{U}^{\tau,F} . \tag{3.49}$$

Here, we denote the countable rovibronic wavefunctions considering nuclear hyperfine interaction as

$$\left|\psi_m^{\tau,F}\right\rangle, \tag{3.50}$$

such that

$$\left\langle\psi_m^{\tau,F}\middle|\mathcal{H}\middle|\psi_{m'}^{\tau,F}\right\rangle = \delta_{m,m'}\, E_m^{\tau,F}, \tag{3.51}$$

where $E_m^{\tau,F}$ is the corresponding eigenvalue of $\left|\psi_m^{\tau,F}\right\rangle$.

The basis transformation procedures from Eq. (3.45) to Eq. (3.49) reveal the key feature of our variational method which involves accounting for the contribution of every basis function to the final eigenstates. Finally, only F, τ, and counting number m are good quantum numbers.

3.5 Line strength of the hyperfine transitions

In the absence of an external field, the line strength of a nuclear spin resolved rovibronic transition is defined by[66]

$$\begin{aligned}
&S(m,\tau,F \leftrightarrow m',\tau',F') \\
&= \sum_{p,M_F,M_{F'}} \left|\left\langle\psi_m^{\tau,F}, M_F\middle|\mathrm{T}_p^1(\boldsymbol{\mu})\middle|\psi_{m'}^{\tau',F'}, M_{F'}\right\rangle\right|^2 \\
&= \left|\left\langle\psi_m^{\tau,F}\middle\|\mathrm{T}^1(\boldsymbol{\mu})\middle\|\psi_{m'}^{\tau',F'}\right\rangle\right|^2 \left[\sum_{p,M_F,M_{F'}} \left|\begin{pmatrix} F & 1 & F' \\ -M_F & p & M_{F'}\end{pmatrix}\right|^2\right] \\
&= \left|\left\langle\psi_m^{\tau,F}\middle\|\mathrm{T}^1(\boldsymbol{\mu})\middle\|\psi_{m'}^{\tau',F'}\right\rangle\right|^2
\end{aligned} \tag{3.52}$$

We initially evaluate the reduced matrix elements of the electric dipole moment in the representation of Eq. (3.4) and then calculate the reduced line strength matrix elements by matrix multiplication:

$${}^{\tau,F}\boldsymbol{D}^{\tau',F'} = (\boldsymbol{\Psi}^{\tau,F})^{\dagger}\, {}^{F}\boldsymbol{D}^{F'}\, \boldsymbol{\Psi}^{\tau',F'}, \tag{3.53}$$

where ${}^{F}\boldsymbol{D}^{F'}$ and ${}^{\tau,F}\boldsymbol{D}^{\tau',F'}$ are the reduced transition dipole moment matrices in the representation of Eq. (3.4) and Eq. (3.50) respectively. The following equations give

the elements of ${}^{F}\boldsymbol{D}^{F'}$, *i.e.* $\left\langle k,J,I,F\middle\|\mathrm{T}^1(\boldsymbol{\mu})\middle\|k',J',I,F\right\rangle$.

As $\boldsymbol{F}=\boldsymbol{J}+\boldsymbol{I}$ and $\mathrm{T}^1(\boldsymbol{\mu})$ commutes with $\boldsymbol{I}$,

$$\begin{aligned}
&\left\langle \text{state},v,\Lambda,S,\Sigma,J,\Omega,M_J,I,F\middle\|\mathrm{T}^1(\boldsymbol{\mu})\middle\|\text{state}',v',\Lambda',S',\Sigma',J',\Omega',M_{J'},I,F'\right\rangle\\
&=(-1)^{J+I+F'+1}\sqrt{(2F+1)(2F'+1)}\begin{Bmatrix}J' & F' & I\\ F & J & 1\end{Bmatrix}\ldots\\
&\quad\times\left\langle \text{state},v,\Lambda,S,\Sigma,J,\Omega\middle\|\mathrm{T}^k(\boldsymbol{\mu})\middle\|\text{state}',v',\Lambda',S',\Sigma',J',\Omega'\right\rangle. \qquad (3.54)
\end{aligned}$$

Rotating the spherical tensor to the body-fixed frame gives:

$$\begin{aligned}
&\left\langle \text{state},v,\Lambda,S,\Sigma,J,\Omega\middle\|\mathrm{T}^k(\boldsymbol{\mu})\middle\|\text{state}',v',\Lambda',S',\Sigma',J',\Omega'\right\rangle\\
&=\left\langle \text{state},v,\Lambda,S,\Sigma,J,\Omega\middle\|\sum_{q=-1}^{1}\mathcal{D}^{(1)}_{\cdot q}(\boldsymbol{\omega})^*\,\mathrm{T}^1_q(\boldsymbol{\mu})\middle\|\text{state}',v',\Lambda',S',\Sigma',J',\Omega'\right\rangle\\
&=\sum_{q=-1}^{1}(-1)^{J-\Omega}\sqrt{(2J+1)(2J'+1)}\begin{pmatrix}J & 1 & J'\\ -\Omega & q & \Omega'\end{pmatrix}\ldots\\
&\quad\times\left\langle \text{state},v,\Lambda,S,\Sigma\middle|\mathrm{T}^1_q(\boldsymbol{\mu})\middle|\text{state}',v',\Lambda',S',\Sigma'\right\rangle. \qquad (3.55)
\end{aligned}$$

The matrix element $\left\langle \text{state},v,\Lambda,S,\Sigma\middle|\mathrm{T}^1_q(\boldsymbol{\mu})\middle|\text{state}',v',\Lambda',S',\Sigma'\right\rangle$ is the same as the one used for the calculation of rovibronic transition intensities excluding nuclear spin in Duo [42],

$$\left\langle \text{state},v,\Lambda,S,\Sigma\middle|\mathrm{T}^1_q(\boldsymbol{\mu})\middle|\text{state}',v',\Lambda',S',\Sigma'\right\rangle=\left\langle \text{state},v\middle|\mu_q(R)\middle|\text{state}',v'\right\rangle, \qquad (3.56)$$

where $\mu_q(R)$ is the electric dipole moment curve represented in the body-fixed frame which can be obtained from *ab initio* calculation.

For electric dipole moment transitions parity has to be changed and thus follows the selection rule:

$$\tau: \quad + \Leftrightarrow - \qquad (3.57)$$

The selection rules on F comes from the Wigner-6j symbol of Eq. (3.54):

$$\Delta F = -1, 0, 1; \text{ and } F \neq 0 \text{ if } \Delta F = 0. \tag{3.58}$$

The hyperfine Hamiltonian mixes wavefunctions with different J; as a result, electric dipole 'forbidden' lines with $|\Delta J| > 1$ are observable. For example, when $I = 1/2$, we can observe electric dipole transitions of O and S branches ($\Delta J = \pm 2$), even if they might be much weaker than the transitions of P, Q and R branches.

3.6 Numerical verification

To illustrate and validate our new hyperfine modules, we calculate hyperfine-resolved rotational spectra for electronic and vibrational ground state of $^{14}N^{16}O$ and $^{24}Mg^{1}H$. While both ^{16}O and ^{24}Mg have nuclear spin zero; ^{14}N has $I = 1$ and ^{1}H has $I = 1/2$ which allows us to test different coupling mechanisms. For this purpose we compare the results of our Duo calculations with of PGOPHER [82] using the same model for each calculation. PGOPHER obtains the energy levels and spectra from effective Hamiltonians given appropriate spectral constants. In contrast, Duo takes in coupling curves and performs variational calculations. To get consistent inputs between the two codes it was necessary to simplify the treatment used by Duo.

For $^{14}N^{16}O$ we approximate the Duo solution by using only one contracted vibrational basis function, *i.e.*, $\left|X\,^2\Pi, v = 0\right\rangle$ which ensures that we avoid any hyperfine-induced interaction between different vibrational states. In PGOPHER, we used values for the rotational constant, B_0, and spin-orbit coupling constant matrix, A_0, computed using Duo:

$$B_0 = \left\langle X\,^2\Pi, v = 0 \middle| \frac{\hbar^2}{2\mu R^2} \middle| X\,^2\Pi, v = 0 \right\rangle, \tag{3.59}$$

$$A_0 = 2\left\langle X\,^2\Pi, v = 0 \middle| C_{\mathrm{SO}}(R) \middle| X\,^2\Pi, v = 0 \right\rangle, \tag{3.60}$$

where μ is the reduced mass of $^{14}N^{16}O$ and $C_{\mathrm{SO}}(R)$ is the spin-orbit coupling curve. Note that, for spin-orbit interaction, the coupling curve, $C_{\mathrm{SO}}(R)$, describes the cou-

Table 3.1: Spectroscopic constants for $^{14}N^{16}O$ used in this chapter.

Constants	Values [cm^{-1}]
B_0	1.69608401
A_0	120

pling energies, while the constant, A, is defined by the splitting energies. Thus, A is defined by twice the matrix element. The NO X $^2\Pi$ potential energy curve used by Duo was taken from Wong *et al.* [83]. $C_{SO}(R)$ was assigned an artificial constant $C_{SO}(R) = 60\,cm^{-1}$ and the transition dipole moment was set to 1 Debye. Our adopted values for B_0 and A_0 are given in Table 3.1.

For this analysis, the hyperfine coupling was chosen using artificial curves much greater than experimental values. By including only one hyperfine constant at a time, we test the affects of particular hyperfine interactions. The results are compared in Table 3.2. Note that, PGOPHER uses nuclear spin-electron spin constants, b, defined by Frosch and Foley [67], rather than b_F. They are related by the dipole-dipole constant, c,

$$b_F = b + \frac{c}{3}. \tag{3.61}$$

Duo achieves excellent agreement with PGOPHER for the calculation of both the line positions ν and line strengths S. The slight differences are due to rounding errors. As we did not include Λ - doubling terms in our calculation the wavenumbers corresponding to b_F, a, eQq_0 and c_I in the first and second columns of the same F = 0.5 (or in the third and fourth columns, $F = 1.5$) of Table 3.2 are the same. Hyperfine interactions only split the transitions of different F in the first and third columns (or in the second and fourth columns). In contrast, the wavenumbers obtained with eQq_2 or d included are different from each other even for the same values of F due to the hyperfine contribution to both Λ - doubling and hyperfine splitting.

We also tested the code for an $I = 1/2$ case by calculating pure rotational transitions within the $v = 0$, $X^2\Sigma^+$ state of ^{24}MgH, again using a unit electric dipole moment curve. This is a rather realistic case, as the input spectral constants to PGOPHER listed in Table 3.3 were determined by the observed transitions[11]. As for the input to Duo, the potential energy curve was shifted from an empirically-

Table 3.2: Comparison of $^{14}N^{16}O$ line positions and line strengths for calculated results from Duo and PGOPHER. Hyperfine constants are in cm^{-1} and line positions are given in MHz. The line strength, S [Debye^2], has the same definition as that in PGOPHER when the intensity unit option of PGOPHER, `IntensityUnit`, is chosen as `HonlLondon` and the transition dipole moment is set to 1 Debye.

Number		1	2	3	4
Upper	F'	0.5	0.5	1.5	1.5
	τ''	−	+	−	+
	J''	1.5	1.5	1.5	1.5
Lower	F''	0.5	0.5	0.5	0.5
	τ''	+	−	+	−
	J''	0.5	0.5	0.5	0.5
$b = 0.1$	ν_{Duo}	148343.21846	148343.21846	147225.55589	147225.55589
	ν_{PG}	148343.21850	148343.21850	147225.55590	147225.55590
$c = 0.3$	S_{Duo}	0.60757296	0.60757296	0.77125182	0.77125182
	S_{PG}	0.60757300	0.60757300	0.77125180	0.77125180
$a = 0.1$	ν_{Duo}	151349.03162	151349.03162	151956.77196	151956.77196
	ν_{PG}	151349.03160	151349.03160	151956.77200	151956.77200
	S_{Duo}	0.58421238	0.58421238	0.72433238	0.72433238
	S_{PG}	0.58421240	0.58421240	0.72433240	0.72433240
$eQq_0 = 0.1$	ν_{Duo}	149591.09156	149591.09156	150930.88155	150930.88155
	ν_{PG}	149591.09160	149591.09160	150930.88160	150930.88160
	S_{Duo}	0.59805081	0.59805081	0.73432902	0.73432902
	S_{PG}	0.59805080	0.59805080	0.73432900	0.73432900
$c_I = 0.1$	ν_{Duo}	145827.72503	145827.72503	150324.61190	150324.61190
	ν_{PG}	145827.72500	145827.72500	150324.61190	150324.61190
	S_{Duo}	0.59221720	0.59221720	0.74027149	0.74027149
	S_{PG}	0.59221720	0.59221720	0.74027150	0.74027150
$eQq_2 = 0.1$	ν_{Duo}	150346.43930	150302.88914	150307.21201	150342.05212
	ν_{PG}	150346.43930	150302.88910	150307.21200	150342.05210
	S_{Duo}	0.59221687	0.59221668	0.74027121	0.74027140
	S_{PG}	0.59221690	0.59221670	0.74027120	0.74027140
$d = 0.1$	ν_{Duo}	150329.98859	150332.52077	149133.39987	151532.62042
	ν_{PG}	150329.98860	150332.52080	149133.39990	151532.62040
	S_{Duo}	0.59210956	0.59211520	0.75214574	0.72851989
	S_{PG}	0.59210960	0.59211520	0.75214570	0.72851990

determined one [84, 85] to reproduce the B_0 constant given in Table 3.3, *i.e.*

$$B_0 = \left\langle X\,^2\Sigma^+, v = 0 \left| \frac{\hbar^2}{2\mu R^2} \right| X\,^2\Sigma^+, v = 0 \right\rangle \tag{3.62}$$

The curves of spin-rotation and hyperfine couplings were defined as:

$$\gamma(R) = \gamma_0, \tag{3.63}$$

$$b_{\mathrm{F}}(R) = b_0 + \frac{c_0}{3}, \tag{3.64}$$

$$c(R) = c_0. \tag{3.65}$$

Note that the contribution of D_0 is not allowed for when only one contracted basis function is used in Duo. Just like the B_v constant, Duo does not use rotational constants, D_v, H_v, *etc.*, either and introduction of these centrifugal distortion would require manipulation of the potential energy curves which are beyond the scope of this thesis. Nevertheless, Duo still gives hyperfine splittings which are consistent with PGOPHER, see the comparison in Table 3.4, because D_0 uniformly shifts the hyperfine energy levels within the same N rotational levels, where N is the quantum number corresponding to $\boldsymbol{N}$ which is defined as:

$$\boldsymbol{N} = \boldsymbol{J} - \boldsymbol{S}. \tag{3.66}$$

Table 3.3: $X\,^2\Sigma^+$, $v = 0$ spectral constants of $^{24}Mg^1H$ determined by Ziurys *et al.* [11]. These values were used as the input to PGOPHER.

Constants	Values [MHz]
B_0	171976.1782
D_0	10.6212
γ_0	790.809
b_0	306.277
c_0	4.792

We then allowed for the effect of vibrational coupling in Duo by increasing contracted vibration bases was set to five functions, *i.e.*, $\left|X\,^2\Sigma^+, v = 0,1,2,3,4\right\rangle$. As shown in Table 3.5, vibrational coupling from higher vibrational states automati-

Table 3.4: Comparison of ^{24}MgH $v = 0$ hyperfine energies calculated by Duo and PGOPHER. Only one vibrational contracted basis function $\left|X\,^2\Sigma^+, v = 0\right\rangle$ was used in this case. All energies are given in MHz.

No.	F	τ	J	N	E_{Duo}	E_{PG}	Difference
1	0	+	0.5	0	-230.9057	-230.9057	0.0000
2	1	+	0.5		76.9686	76.9686	0.0000
3	1	−	0.5	1	343117.2196	343074.7347	42.4849
4	0	−	0.5		343236.9188	343194.4339	42.4849
5	1	−	1.5		344238.9505	344196.4655	42.4850
6	2	−	1.5		344424.5699	344382.0849	42.4850

cally introduces centrifugal distortion to the $v = 0$ state and improves the accuracy of the calculation, compared with the lower rotational levels in Table 3.4. The potential energy and spin-rotation curves are not very accurate here, and thus for higher rotational levels, we still got obvious energy differences in Table 3.5, and frequency differences in Table 3.6.

Finally, we list two calculated S branch ($\Delta J = 2$) transitions in the second and fourth rows of Table 3.7. These hyperfine-induced transitions are much weaker than the two R branch ($\Delta J = 1$) transitions in the first and third rows.

3.7 Conclusion

We demonstrate an algorithm for the calculation of hyperfine structure of diatomic molecules based on a variational treatment of nuclear motion. Nuclear magnetic dipole coupling terms including Fermi-contact, nuclear-spin–electron-spin dipole-dipole interaction, nuclear spin-orbit, nuclear spin-rotation, and nuclear electric quadrupole interaction terms are considered in our calculation. New modules for the hyperfine structure calculation are added to the flexible variational nuclear-motion package Duo [42].

Based on the eigenfunctions and eigenvalues of $\boldsymbol{J}$, a parity-conserved rovibronic Hamiltonian matrix of particular total angular momentum, $\boldsymbol{F}$, is constructed and diagonalized. The hyperfine wavefunctions are finally represented using a Hund's case (a_β) basis set. Hyperfine-resolved line lists for diatomic molecules can be computed depending on the hyperfine energy levels and wavefunctions. To

Table 3.5: Comparison of ^{24}MgH $v = 0$ hyperfine energies calculated by Duo and PGOPHER. Five vibrational contracted basis functions $\left|X\,^2\Sigma^+, v = 0,1,2,3,4\right\rangle$ were used in this case. All energies are given in MHz.

No.	F	τ	J	N	E_{Duo}	E_{PG}	ΔE
1	0	+	0.5	0	-230.9058	-230.9057	-0.0001
2	1	+	0.5	0	76.9686	76.9686	0.0000
3	1	−	0.5	1	343074.6047	343074.7347	-0.1300
4	0	−	0.5	1	343194.3039	343194.4339	-0.1300
5	1	−	1.5	1	344196.3356	344196.4655	-0.1299
6	2	−	1.5	1	344381.9550	344382.0849	-0.1299
7	2	+	1.5	2	1030229.8178	1030230.9249	-1.1071
8	1	+	1.5	2	1030363.5553	1030364.6624	-1.1071
9	2	+	2.5	2	1032168.8370	1032169.9441	-1.1071
10	3	+	2.5	2	1032341.1483	1032342.2554	-1.1071
11	3	−	2.5	3	2060535.9577	2060540.0064	-4.0487
12	2	−	2.5	3	2060675.3485	2060679.3973	-4.0488
13	3	−	3.5	3	2063276.7730	2063280.8218	-4.0488
14	4	−	3.5	3	2063443.5527	2063447.6015	-4.0488
15	4	+	3.5	4	3433222.1380	3433231.9781	-9.8401
16	3	+	3.5	4	3433364.6194	3433374.4596	-9.8402
17	4	+	4.5	4	3436759.8067	3436769.6469	-9.8402
18	5	+	4.5	4	3436923.5400	3436933.3802	-9.8402
19	5	−	4.5	5	5147267.6517	5147285.8407	-18.1890
20	4	−	4.5	5	5147412.0861	5147430.2751	-18.1890
21	5	−	5.5	5	5151599.9592	5151618.1483	-18.1891
22	6	−	5.5	5	5151761.7609	5151779.9499	-18.1890
23	6	+	5.5	6	7201400.1636	7201426.5351	-26.3715
24	5	+	5.5	6	7201545.9449	7201572.3164	-26.3715
25	6	+	6.5	6	7206525.9256	7206552.2971	-26.3715
26	7	+	6.5	6	7206686.3922	7206712.7637	-26.3715
27	7	-	6.5	7	9594096.6941	9594124.3704	-27.6763
28	6	-	6.5	7	9594243.4608	9594271.1371	-27.6763
29	7	-	7.5	7	9600015.2023	9600042.8786	-27.6763
30	8	-	7.5	7	9600174.6909	9600202.3672	-27.6763
31	8	+	7.5	8	12323585.3054	12323594.8594	-9.5540
32	7	+	7.5	8	12323732.8245	12323742.3785	-9.5540
33	8	+	8.5	8	12330296.1028	12330305.6568	-9.5540
34	9	+	8.5	8	12330454.8439	12330464.3979	-9.5540
35	9	-	8.5	9	15387847.1770	15387798.6594	48.5176
36	8	-	8.5	9	15387995.2894	15387946.7718	48.5176
37	9	-	9.5	9	15395349.9512	15395301.4336	48.5176
38	10	-	9.5	9	15395508.1024	15395459.5848	48.5176

Table 3.6: Comparison of ^{24}MgH $v = 0$ hyperfine line positions. Five vibrational contracted basis functions $\left|X\,^2\Sigma^+, v = 0,1,2,3,4\right\rangle$ were used in this case. All frequencies are give in MHz.

No.	N'	J'	F'	N''	J''	F''	ν_{Duo}	Measured [11] [86]
1	1	0.5	1	0	0.5	1	342997.636	342997.763(050)
2	1	0.5	0	0	0.5	1	343117.335	343117.463(050)
3	1	0.5	1	0	0.5	0	343305.510	343305.646(050)
4	1	1.5	1	0	0.5	1	344119.367	344119.497(050)
5	1	1.5	2	0	0.5	1	344304.986	344305.125(050)
6	1	1.5	1	0	0.5	0	344427.241	344427.362(050)
7	2	1.5	2	1	0.5	1	687155.213	687157.17(17)
8	2	1.5	1	1	0.5	0	687169.251	687171.00(17)
9	2	2.5	3	1	1.5	2	687959.193	687959.54(19)
10	2	2.5	2	1	1.5	1	687972.501	687972.66(17)
11	3	2.5	3	2	2.5	3	1028194.809	1028202.5(10)
12	3	2.5	2	2	2.5	2	1028506.511	1028514.2(10)
13	3	3.5	4	2	2.5	3	1031102.404	1031104.29(21)
14	3	3.5	3	2	2.5	2	1031107.936	1031104.29(21)
15	4	3.5	4	3	3.5	4	1369778.585	1369797.0(10)
16	4	3.5	3	3	3.5	3	1370087.846	1370107.5(10)
17	4	3.5	4	3	2.5	3	1372686.180	1372700.06(98)
18	4	3.5	3	3	2.5	2	1372689.271	1372700.06(98)
19	4	4.5	5	3	3.5	4	1373479.987	1373485.81(55)
20	4	4.5	4	3	3.5	3	1373483.034	1373485.81(55)
21	6	5.5	6	5	4.5	5	2054132.512	2054170.48(71)
22	6	5.5	5	5	4.5	4	2054133.859	2054170.48(71)
23	6	6.5	7	5	5.5	6	2054924.631	2054944.05(82)
24	6	6.5	6	5	5.5	5	2054925.966	2054944.05(82)

test the new module, we calculate the hyperfine structure of the $v = 0$, $X\,^2\Sigma^+$ state of ^{24}MgH. The results of Duo and PGOPHER show excellent agreement for both line positions and line strengths. The Duo code and the input file used for $^{14}N^{16}O$ and ^{24}MgH are available at https://github.com/ExoMol/Duo .

Our newly developed methodology builds a bridge between calculations of electronic motion and nulcear motion of diatomic molecules which makes it possible to calculate nuclear magnetic dipole and electric quadruple hyperfine structure effects from first principles. Some hyperfine coupling constants considered in this chapter may be calculated by quantum chemistry programs *e.g.*, DALTON [87] and CFOUR [88]. It is also possible to evaluate them manually after obtaining elec-

Table 3.7: Comparison of the line positions and strengths in the R and S branches of ^{24}MgH $v = 0$ hyperfine transitions. Line positions are given in MHz. Five vibrational contracted basis functions $\left|X\,^2\Sigma^+, v = 0,1,2,3,4\right\rangle$ were used in this case. The line strength, S [Debye^2], has the same definition as that in PGOPHER when the intensity unit option of PGOPHER, `IntensityUnit`, is chosen as `HonlLondon` and the transition dipole moment is set to 1 Debye.

No.	1	2	3	4
F'	2	2	3	3
τ'	+	+	-	-
J'	2.5	2.5	3.5	3.5
F''	1	1	2	2
τ''	-	-	+	+
J''	1.5	0.5	2.5	1.5
ν_{Duo}	687972.5015	689094.2323	1031107.9360	1033046.9552
ν_{PG}	687973.4786	689095.2094	1031110.8777	1033049.8969
S_{Duo}	1.7558441	0.0053314	2.8371019	0.0014804
S_{PG}	1.755851	0.0053315	2.837127	0.0014805

tronic wavefunctions [78]. We will discuss the *ab initio* calculation of hyperfine coupling constants in Chapter 6.

Chapter 4

A Spectroscopic Model for the Lowest Four Doublet States of NO

4.1 Introduction

Nitric oxide (NO) is one of the principle oxides of nitrogen. It plays a significant role in the nitrogen cycle of our atmosphere [89, 90] but also causes problems of air pollution and acid rain [91, 92, 93]. Therefore, scientists are devoting increasing attention to reducing NO in combustion processes [94, 95]. NO is a biological messenger for both animals and plants [96, 97, 98] but it may be harmful or even deadly as well [99, 100]. Nitric oxide (NO) is widely distributed in the universe. The molecule was observed in the atmosphere of Venus [12] and Mars [101], where it is one of the emission sources of the UV nightglow [102, 103]. Gerin et al. detected transitions of NO in the dark clouds L134N [104] and TMC1 [105]. Halfen *et al.* reported their analysis of transitions of N_2O to NO in the core region of the Sagittarius B2 and evaluated the N/O chemical network [106]. The first detection of extragalactic NO helps us to understand the chemistry of galaxy NGC 253 [107]. NO has yet to be detected in the atmosphere of an exoplanet but is thought likely to be important in the atmospheres of rocky exoplanets [108]. The detection of NO in the astronomical objects relies on knowledge of the corresponding spectral lines of the molecule so accurate NO line list plays significant role in the processes.

The importance of NO has aroused the interest of academia and industry since

it was prepared by van Helmont in the 17th century [109] and then studied by Priestley in 1772 [110]. In numerous theoretical and experimental works, there are large number of spectroscopic investigations, as spectra provide a powerful weapon to reveal the physical and chemical properties of the molecule. For instance, as a stable open shell molecule, the electronically excited Rydberg states of NO have been extensively studies, see the paper of Deller and Hogan [76] and references therein. The spectrum of NO was also of great value in many applications, such as temperature measurements by laser induced fluorescence [111, 112].

The ExoMol project [24] computes molecular line lists studies of exoplanet and (other) hot atmospheres. The ExoMol database was formally released in 2016 [113]. The most recent 2020 version [25] covers the line lists of 80 molecules and 190 isotopologues, totaling 700 billion transitions. It includes an accurate infrared (IR) line list of NO, called `NOname`, which contains the rovibrational transitions within the ground electronic state [114]. The rovibronic transitions of NO in the ultraviolet (UV) region are not included in `NOname`. These bands are strong, atmospherically important and have been observed in many studies [115, 116, 7]. There is no NO UV line list in well-known databases such as HITRAN [117] and GEISA [26] either.

Luque and Crosley have investigated spectra of diatomic molecules over a long period [118, 6, 119]. Based on their works, they developed a spectral simulation program, LIFBASE [34], providing a database of OH, OD, CH *etc.*, and NO as well. LIFBASE contains the positions and relative probabilities of UV transitions in four spectral systems of NO, *i.e.*, γ ($A^2\Sigma^+$ to $X^2\Pi$), β ($B^2\Pi$ to $X^2\Pi$), δ ($C^2\Pi$ to $X^2\Pi$) and ϵ ($D^2\Sigma^+$ to $X^2\Pi$) systems. The upper vibrational energy levels for $B^2\Pi$ and $C^2\Pi$ of NO in LIFBASE are limited to below $v = 7$ and $v = 1$, respectively. However, the observed β and δ transitions corresponding to higher upper vibrational energy levels are even stronger [120, 7]. There is a need to develop a comprehensive UV line list for NO to cover these band systems. To do this one first needs to construct a spectroscopic model which requires overcoming a number of theoretical difficulties.

A major issue in generating a UV line list for NO results from the difficulty

of modelling the interaction between $B\,^2\Pi$ and $C\,^2\Pi$ states, which is caused by the particular electronic structure of NO. To understand this fifteen-electron system one must analyse the electron configuration of these states from the perspective of molecular orbitals. On one hand, excitation of inner paired electrons to higher valence orbitals leads to valence states such as the $B\,^2\Pi$ state. On the other hand, the outermost unpaired electron may be excited to Rydberg orbitals, yielding a series of Rydberg-like states such the $A\,^2\Sigma^+$ or $C\,^2\Pi$ state. These Rydberg states lie close in energy to the valence ones. Furthermore, as NO^+ has a shorter equilibrium bond length than NO [121], Rydberg states tend to be lower in energy at short bond lengths, R, while valence states are lower at larger R. Thus, in NO, Rydberg-valence interactions are densely distributed in the neighbourhood of the equilibrium bond length of its ground state, where large Franck-Condon factors exist. The $B\,^2\Pi$ - $C\,^2\Pi$ interaction is the lowest one and has attracted the most attention. As described by Lagerqivst and Miescher [115], the two states show a strong and extended mutual perturbation. They proposed a 'deperturbation' method to explain the vibrational and rotational perturbation of $B\,^2\Pi$ - $C\,^2\Pi$ interaction. Further analysis was made by Gallusser and Dressler [77], who set up a vibronic interaction matrix of five $^2\Pi$ states and fitted the eigenvalues of the matrix to experimental data in the determination of RKR potential curves and off-diagonal electronic energies. As a consequence, they predicted vibrational states of the $B\,^2\Pi$ electronic state up to $v = 37$.

In this chapter, we present a method based on directly diagonalizing a rovibronic matrix to resolve the energy structures of $B\,^2\Pi$ - $C\,^2\Pi$ coupled states. This matrix is based on the use of full variational solution of the rovibronic nuclear motion Hamiltonian rather than perturbation theory. This method is general and can be used to predict spectra, for example at elevated temperatures.

In addition to the vibronic matrix elements (*e.g.*, spin doublets) considered in the previous studies, more fine structure terms, such as Λ-doubling and spin-rotational coupling, are used to construct the rovibronic matrix. The eigenvalues of the matrix are fitted to rovibronic energies obtained using a MARVEL (mea-

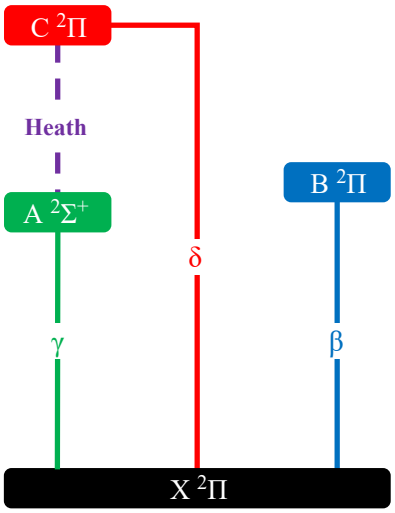

Figure 4.1: The band systems of NO involved in this thesis and their names. The γ, β and δ systems mainly cover the UV transitions of NO. Jenkins *et al.* recorded many visible lines from the B $^2\Pi$ state to higher vibrational levels of the X $^2\Pi$ state, *e.g.*, those of the $\beta(3,16)$ band [1]. The high-accuracy IR transitions of the Heath$(0,0)$ band were measured by Amiot and Verges [2]. For a comprehensive band system diagram, see the work of Cartwright *et al.* [3]

sured active rotation-vibration energy levels) procedure [122, 123] analysis of the observed NO IR/visible/UV transitions to ensure a quantitatively accurate result. Figure 4.1 summarizes the band systems involved in our MARVEL analysis. The objective functions were constrained with the *ab initio* curves produced using MOLPRO 2015 [124] to avoid overfitting problems. The above procedures are also applied to the A $^2\Sigma^+$ state of NO to get a self-consistent description of the doublet electronic states up to and including C $^2\Pi$.

The model in this chapter forms the foundation of our study on the generation of the UV line list of NO in the next chapter. The modeling of the B $^2\Pi$ - C $^2\Pi$ coupling paves the way for the investigations of molecules with similar avoided crossing structures, *e.g.*, NO_3 [125].

4.2 Theoretical study of the low-lying electronic states of NO

Complete active space self-consistent field (CASSCF) and multireference configuration interaction (MRCI) calculations were performed in the quantum chemistry

package MOLPRO 2015 [126] to get the potential energy and spin-orbit curves of the $X\,^2\Pi$, $A\,^2\Sigma^+$, $B\,^2\Pi$ and $C\,^2\Pi$ states. A major issue in the calculation is achieving a balance between representations of the Rydberg, A and C, states and the valence, X and B, states. Figure 4.2 presents an overview of the low-lying PECs and illustrates the importance of the $C\,^2\Pi$– $B\,^2\Pi$ Rydberg – Valence avoided crossing.

The history of high quality CI calculations for the excited states of NO can be tracked back to 1982, when Grein and Kapur reported their work on states with minimum electronic energies lower than 6.58 eV [127]. Several years later, a comprehensive theoretical study on NO was presented and discussed by de Vivie and Peyerimhoff [128]. The results of this paper were further improved by Shi and East in 2006 [4]. More accurate curves were obtained with extended basis set and active space in the recent works of Cheng *et al.* [129, 130]. Recently, the spin-orbit coupling in the ground state of NO was studied by Silva *et al.* [131]. Although the previous works [127, 132, 133, 128, 134, 135, 4, 129] provide us with strong inspiration, the task is still challenging due to the interactions between the Rydberg and valence states of NO.

4.2.1 Active space and basis set

For heteronuclear diatomic molecules, MOLPRO executes calculations in four irreducible representations a_1, b_1, b_2 and a_2 of the C_{2v} point group. Here, we use $[(n_1,n_2,n_3,n_4)-(n_1',n_2',n_3',n_4')]$ to represent occupied orbitals excluding closed orbitals, *i.e.* the calculation active space. A typical active space for the lower electronic state calculations of NO is $[(8,3,3,0)-(2,0,0,0)]$, as suggested by Shi and East [4]. Although only a few of the PECs are of direct interest here, we had to include extra states to achieve correct calculation. We also adjusted the active space to get smooth curves.

A Dunning aug-cc-pV(n)Z basis set [136] was used in both CASSCF and MRCI calculations. This basis set has an additional shell of diffuse functions compared to the cc-pV(n)Z basis set, which benefits the calculation of Rydberg states. Too many diffuse functions, *e.g.*, those of the d-aug-cc-pV(n)Z basis set, may have negative effects on the calculation because of the overemphasis of the Rydberg

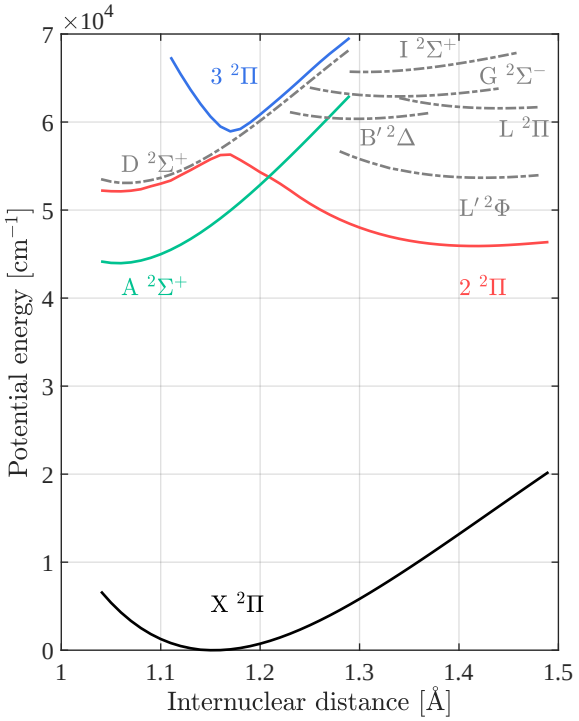

Figure 4.2: NO PECs calculated by Shi and East [4]. The states of interest are indicated by solid curves. Here, $2\,^2\Pi$ is the $B\,^2\Pi$ to $C\,^2\Pi$ PEC while $3\,^2\Pi$ is the $C\,^2\Pi$ to $B\,^2\Pi$ PEC.

states relative to the valence states.

4.2.2 CASSCF calculation

Our calculations started with a $[(8,3,3,0)-(2,0,0,0)]$ active space in which the interactions between the Rydberg and valence states are inescapable. However, representing the avoided crossing points caused by $C\,^2\Pi$ and the valence $^2\Pi$ states is a huge obstacle. panel (a) of Fig. 4.3 shows the behavior of B - C interaction near 1.18 Å. The potential energy curve (PEC) of $C\,^2\Pi$ suddenly jumps to that of $B\,^2\Pi$, producing discontinuity in the PEC of $X\,^2\Pi$ too. To get the exited states, we used the state average algorithm but the average energy of the two $^2\Pi$ states changed when traversing the crossing point of $C\,^2\Pi$ and $B\,^2\Pi$.

A valid way to smooth the curves is to increase the number of averaged states. For example, the discontinuities near 1.18 Å disappears when introducing a third $^2\Pi$ state in CASSCF calculation, as shown in panel (b) of Fig. 4.3. Nevertheless, similar phenomenon arise when the third state comes across the $L\,^2\Pi$ state. Alternatively,

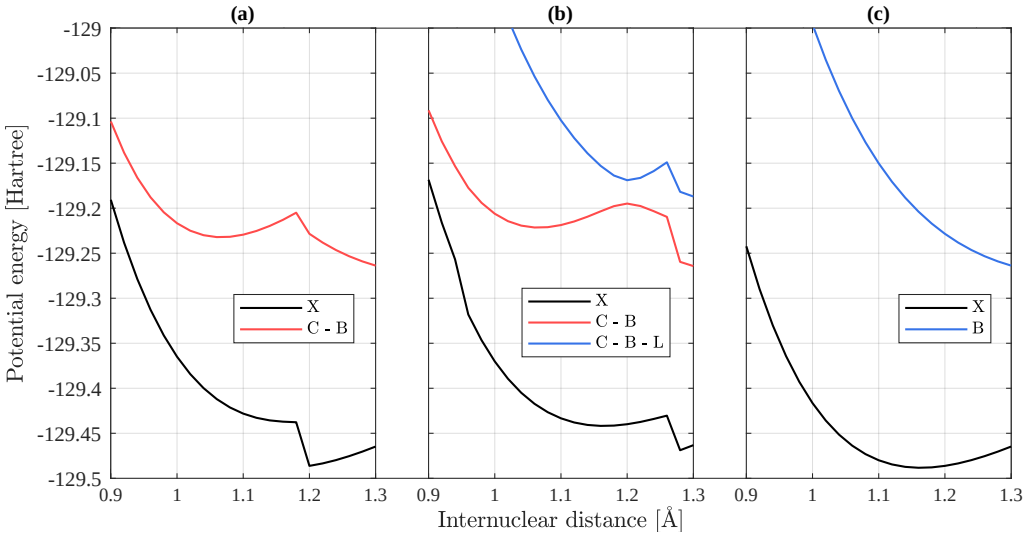

Figure 4.3: The PECs in the active space of $[(8,3,3,0)-(2,0,0,0)]$ with the basis set of aug-cc-pVTZ. (a) Two $^2\Pi$ states averaged CASSCF calculation starting from 0.9 Å. (b) Three $^2\Pi$ states averaged CASSCF calculation starting from 0.9 Å. (c) Two $^2\Pi$ states averaged CASSCF calculation starting from 1.3 Å.

smooth curves can be obtained in a limited active space. For example, we can get a continuous curves of the C $^2\Pi$ state in the active space $[(6,3,3,0)-(4,1,1,0)]$ from 0.9 Å to 1.28 Å.

We always started a new CASSCF iteration from the orbitals of a nearby geometry to stabilize and accelerate the calculation. The PECs in panels (a) and (b) of Fig. 4.3, are obtained by increasing the internuclear distance from 0.9 Å to 1.3 Å. Interestingly, with a initial geometry at 1.3 Å, reversing the calculation direction gives a completely different result in the same active space, *i.e.*, two smooth valence PECs of the X $^2\Pi$ and B $^2\Pi$ states in panel (c) of Fig. 4.3. Due to the limitation of nonlinear programming, CASSCF iterations may fall into local minima. To get the target states, the numerical optimization must be properly initialized. For the NO molecule, the iterations which begin with valence orbitals usually end with valence orbitals but it is uncertain for those begin with Rydberg orbitals. The results imply that there are at least two kinds of local minima in the *ab initio* calculation of NO with MOLPRO: pure valence orbitals (corresponding to panel (c) of Fig. 4.3) and Rydberg-valence hybrid orbitals (corresponding to panels (a) and (b) of Fig. 4.3). To verify the conjecture: initializing a calculation of two $^2\Pi$ states averaged with

the CASSCF orbitals of the $X\,^2\Pi$ state in the single state calculation, one can get almost the same curves as those in panel (c) of Fig. 4.3, starting from 0.9 Å.

In Section 4.4, we use diabatic potentials in modeling the interaction between the $B\,^2\Pi$ and $C\,^2\Pi$ states. We describe the curves as 'adiabatic' if they contain the B - C avoided crossing feature, *e.g.*, those in panel (b) of Fig. 4.3. If not, we call the curves 'diabatic', *e.g.*, those in panel (c) of Fig. 4.3.

4.2.3 MRCI calculation

Although consuming many more computational resources, the MRCI calculation in MOLPRO is straightforward. MOLPRO automatically takes the CASSCF orbitals as the references and performs an internally contracted configuration interaction calculation based on single or double excitation. The spin-orbit coupling terms were also produced. To compensate the error brought by a truncated configuration interaction expansion, the energies were modified by a Davidson correction, *i.e.*, a MRCI + Q calculation. panel (a) of Fig. 4.4 demonstrates the results of CASSCF & MRCI + Q calculations of the $X\,^2\Pi$, $A\,^2\Sigma^+$, $B\,^2\Pi$, $C\,^2\Pi$, $D\,^2\Sigma^+$ and $L'\,^2\Phi$ states, in the $[(8,3,3,0)-(2,0,0,0)]$ active space with the aug-cc-pV5Z basis set.

In the CASSCF routine, the projection of angular momentum of a diatomic molecule on its internuclear axis, Λ, can be assigned to specify the expected states. However, the MRCI routine does not have this the option and always finds the lowest energy states of the same spin. As a result, the PECs of $C\,^2\Pi$ and $L'\,^2\Phi$ exchange with each other at their crossing point although the avoided crossing principle is not applicable for the two states, as shown by the blue curve in panel (a) of Fig. 4.4. It is feasible to calculate and output the Λ quantum numbers (technically, `Lz`, which is defined as a non-diagonal matrix element between two degenerate components, *e.g.* $\left\langle \Pi_x \middle| \hat{L}_z \middle| \Pi_y \right\rangle$) in MRCI calculations, which helps to distinguish the $C\,^2\Pi$, $L'\,^2\Phi$ and $L\,^2\Pi$ states. The blue and yellow curves on the right of their crossing point were manually switched, as shown in panel (c) of Fig. 4.4, according to their Λ quantum numbers shown in panel (b). The T_e values of $A\,^2\Sigma^+$, $B\,^2\Pi$ and $C\,^2\Pi$ states are compared with those calculated by Shi and East in Table 4.1.

The PECs in Fig. 4.4 range from 1.0 Å to 1.26 Å. The curves were deliberately

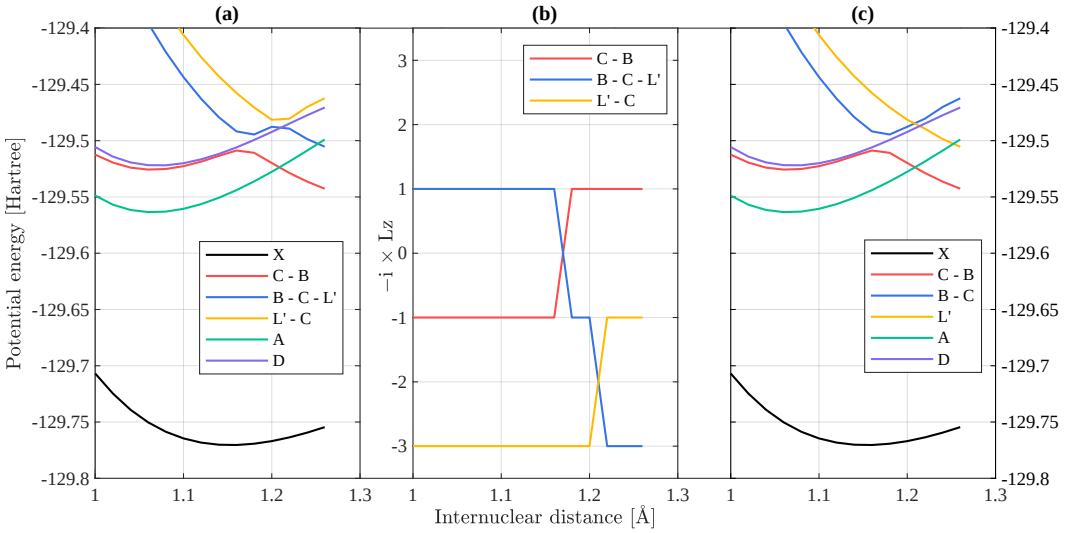

Figure 4.4: The PECs of the $X\,^2\Pi$, $A\,^2\Sigma^+$, $B\,^2\Pi$, $C\,^2\Pi$, $D\,^2\Sigma^+$ and $L'\,^2\Phi$ states, obtained by CASSCF & MRCI + Q calculation starting from 1.06 Å to both sides in the active space $[(8,3,3,0)-(2,0,0,0)]$ with the aug-cc-pV5Z basis set. The third $^2\Pi$ curve and the $L'\,^2\Phi$ curve in panel (a) were manually switched in panel (c) on the right of 1.2 Å, according to the value of `Lz`, shown in panel (b). The phase of `Lz`, in the Cartesian representation, is random. To distinguish different electronic states, the yellow curve in panel (b) is smoothed for internuclear distances less than 1.1 Å. The $X\,^2\Pi$ state is not shown in the panel as the `Lz` values obtained are all −i.

Table 4.1: Comparison of T_e values of the MRCI + Q calculation

State	CASSCF & MRCI + Q		Empirical	
	Shi and East [4]	This work	Huber and Herzberg [137]	This work[b]
$A\,^2\Sigma^+$	43 558	45 410.2	43 965.7	43 902.99
$B\,^2\Pi$	44 803	46 260.3[a]	45 913.6	45 867.05
$C\,^2\Pi$	51 808	53 709.5	52 126	52 081.97

a. Two-state average CASSCF & MRCI + Q calculation.
b. See Section 4.4.

truncated at the right endpoint because of the $C\,^2\Pi$ - $L\,^2\Pi$ interaction as shown in panel (b) of Fig. 4.3. On the left endpoint, The MRCI program exited with an '`INSUFFICIENT OVERLAP`' error. The error is triggered by interactions with another $^2\Pi$ state, $H'\,^2\Pi$, which lies below the $B\,^2\Pi$ state near the 1.06 Å and which cannot be described by the reference space. A solution to the problem is to perform MRCI calculations using a larger active space such as $[(8,4,4,0)-(2,0,0,0)]$.

It is not quantitatively accurate to generate line lists with the *ab initio* curves;

however, the curves and couplings provide a suitable starting point for work. These curves and couplings need to be refined using experimental data, which is the content of the subsequent two sections.

4.3 MARVEL analysis of the rovibronic energy levels of $^{14}N^{16}O$

The rovibronic energy levels of the $A\,^2\Sigma^+$, $B\,^2\Pi$ and $C\,^2\Pi$ states were reconstructed by MARVEL analysis of the experimental transitions of the γ, β, δ, and Heath systems and those inside the ground state.

In the previous work by Wong *et al.* [114], 11 136 IR transitions were collected, yielding a spectroscopic network of 4106 energy levels. To retrieve the energy levels of $A\,^2\Sigma^+$, $B\,^2\Pi$ and $C\,^2\Pi$ states, we extracted a further 9861 transitions (including 3393 γ, 5103 β, 1004 δ and 361 Heath transitions) from the data sources listed in Table 4.2. The vibronic structure of the spectroscopic network is illustrated in Fig. 4.5.

Although there are studies which report measured transition frequencies for the four band systems of interest, only the most reliable data sets were included in our MARVEL analysis. For example, Lagerqvist and Miescher published the line position data of 20 bands of the β and δ systems ($\beta(5,0)$ to $\beta(19,0)$ and $\delta(0,0)$ to $\delta(4,0)$, respectively) in 1958 (58LaMi [115]), but half of them were replaced by more accurate line lists measured by Yoshino *et al.* around 2000 (94MuYoEs [138], 98YoEsPa [120], 00ImYoEs [139], 02ChLoLe [140], 02RuYoTh [141], 06YoThMu [7]).

Table 4.2: Data sources used in the final MARVEL analysis

Source	Band	$J''_{\min}$	$J''_{\max}$	Uncertainty[cm^{-1}]	No. of Trans.[a] (A)	(V)
97DaDoKe [116]	$\gamma(0,0)$	0.5	41.5	0.04 - 0.15	304	277

a. Number of measured (A) and validated (V) Transitions

Source	Band	J''_{min}	J''_{max}	Uncertainty[cm^{-1}]	No. of Trans.[a] (A)	(V)
97DaDoKe	$\gamma(0,1)$	0.5	40.5	0.04 - 0.15	277	245
97DaDoKe	$\gamma(0,2)$	1.5	39.5	0.04 - 0.15	339	317
97DaDoKe	$\gamma(0,3)$	1.5	38.5	0.04 - 0.1	289	279
97DaDoKe	$\gamma(0,4)$	1.5	42.5	0.04 - 0.1	294	283
97DaDoKe	$\gamma(0,5)$	1.5	37.5	0.04 - 0.1	266	249
97DaDoKe	$\gamma(0,6)$	1.5	31.5	0.04 - 0.15	158	142
97DaDoKe	$\gamma(1,0)$	0.5	30.5	0.04 - 0.15	302	275
97DaDoKe	$\gamma(1,4)$	0.5	41.5	0.04 - 0.15	295	277
97DaDoKe	$\gamma(1,5)$	1.5	39.5	0.04 - 0.15	142	135
97DaDoKe	$\gamma(2,6)$	1.5	40.5	0.04 - 0.15	277	246
97DaDoKe	$\gamma(2,7)$	2.5	41.5	0.04 - 0.15	160	155
02ChLoLe [140]	$\gamma(3,0)$	0.5	24.5	0.03 - 0.05	227	205
97DaDoKe	$\gamma(3,4)$	4.5	32.5	0.04 - 0.2	63	56
27JeBaMu [1]	$\beta(0,4)$	0.5	24.5	0.2	122	52
27JeBaMu	$\beta(0,5)$	0.5	24.5	0.2	152	143
27JeBaMu	$\beta(0,6)$	0.5	24.5	0.2	126	124
27JeBaMu	$\beta(0,7)$	0.5	29.5	0.2	202	200
27JeBaMu	$\beta(0,8)$	0.5	31.5	0.2	206	204
27JeBaMu	$\beta(0,9)$	0.5	31.5	0.2	192	188
27JeBaMu	$\beta(0,10)$	0.5	31.5	0.2	208	202
27JeBaMu	$\beta(0,11)$	0.5	31.5	0.2	184	180
27JeBaMu	$\beta(0,12)$	0.5	22.5	0.2	138	138
27JeBaMu	$\beta(1,6)$	0.5	19.5	0.2	123	119
27JeBaMu	$\beta(1,11)$	0.5	24.5	0.2	148	142
27JeBaMu	$\beta(1,13)$	0.5	23.5	0.2	154	150
27JeBaMu	$\beta(2,9)$	0.5	22.5	0.2	138	130

a. Number of measured (A) and validated (V) Transitions

Source	Band	J''_{min}	J''_{max}	Uncertainty[cm^{-1}]	No. of Trans.[a] (A)	(V)
27JeBaMu	β(2,13)	0.5	21.5	0.2	128	128
27JeBaMu	β(2,14)	0.5	21.5	0.2	144	139
27JeBaMu	β(2,15)	0.5	24.5	0.2	102	99
92FaCo [142]	β(3,0)	0.5	31.5	0.05 - 0.1	432	426
96DrWo [143]	β(4,0)	0.5	8.5	0.003 - 0.004	66	66
96DrWo	β(5,0)	0.5	7.5	0.003 - 0.005	52	52
58LaMi [115]	β(5,0)	8.5	14.5	0.2	36	36
02ChLoLe	β(6,0)	0.5	17.5	0.03 - 0.1	138	135
94MuYoEs [138]	β(7,0)	0.5	7.5	0.03 - 0.1	76	60
58LaMi	β(7,0)	6.5	16.5	0.2 - 0.25	70	64
58LaMi	β(8,0)	0.5	16.5	0.2	124	120
98YoEsPa [120]	β(9,0)	0.5	23.5	0.02 - 0.03	188	178
06YoThMu [7]	β(10,0)	0.5	12.5	0.03 - 0.15	218	193
02RuYoTh [141]	β(11,0)	0.5	17.5	0.03 - 0.08	134	125
06YoThMu	β(12,0)	0.5	20.5	0.03 - 0.15	188	173
58LaMi	β(13,0)	11.5	18.5	0.2	97	97
06YoThMu	β(14,0)	0.5	20.5	0.03 - 0.08	196	153
58LaMi	β(15,0)	0.5	17.5	0.2 - 0.5	239	215
58LaMi	β(16,0)	0.5	14.5	0.2 - 0.3	138	133
58LaMi	β(17,0)	0.5	11.5	0.2 - 0.5	42	42
58LaMi	β(18,0)	0.5	12.5	0.2 - 0.5	120	108
58LaMi	β(19,0)	0.5	12.5	0.2 - 0.5	82	80
94MuYoEs	δ(0,0)	0.5	20.5	0.03 - 0.1	225	217
00ImYoEs [139]	δ(1,0)	0.5	18.5	0.03 - 0.1	261	205
06YoThMu	δ(2,0)	0.5	21.5	0.03 - 0.15	250	210
06YoThMu	δ(3,0)	0.5	18.5	0.03 - 0.08	138	109

a. Number of measured (A) and validated (V) Transitions

Source	Band	J''_{min}	J''_{max}	Uncertainty[cm^{-1}]	No. of Trans.^{a} (A)	(V)
58LaMi	$\delta(4,0)$	0.5	11.5	0.2 - 0.6	130	120
82AmVe [144]	Heath(0,0)	0.5	11.5	0.01	361	360

a. Number of measured (A) and validated (V) Transitions

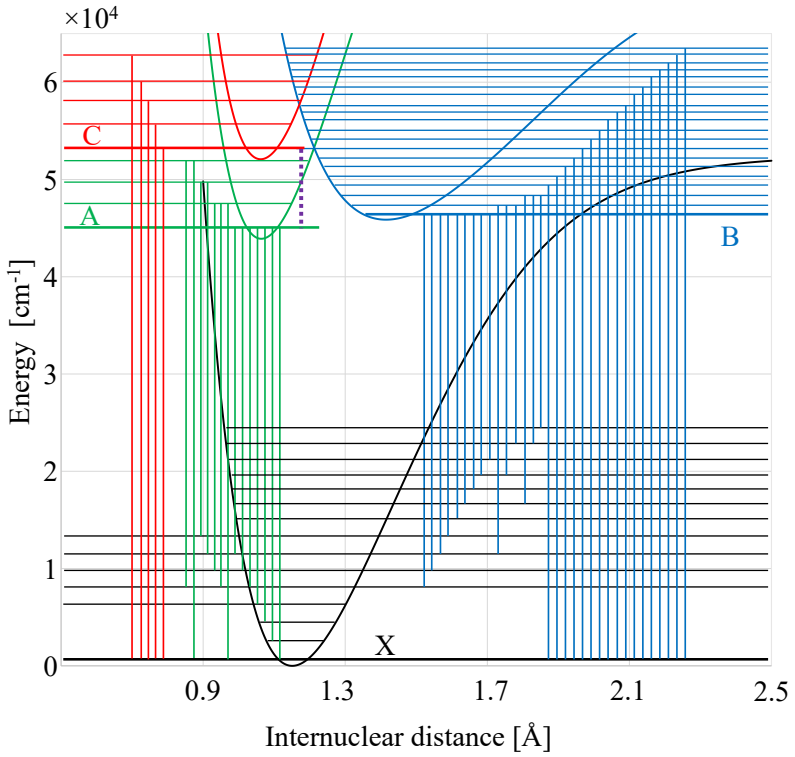

Figure 4.5: Vibronic structure of the MARVEL analysis. The vertical solid lines in green, blue and red illustrate the bands of γ, β and δ systems, respectively. The vertical dash line in purple represents the Heath(0,0) band.

The spectroscopic network in MARVEL [145] is established in accordance with the upper and lower quantum numbers of the transitions. We used five quantum numbers, as shown in Table 4.3, to uniquely label the rovibronic energy levels. The quantum numbers of some transitions were improperly assigned. New assignments plus some other comments on the sources are given below:

- In some cases (*e.g.* for the $A\,^2\Sigma^+$ state, the Q_{21} branch is indeed a copy of R_{11} branch as listed in 97DaDoKe [116]) duplicate transitions are provided in source data. In 27JeBaMu [1], 58LaMi [115], *etc.*, Λ - doubling fine structures of many transitions are not resolved; therefore we simply created two

transitions differing in e/f parity with the same frequency in the MARVEL dataset.

- The uncertainties of the transitions of 27JeBaMu [1] and 58LaMi [115] were given by combination difference tests, referring to the energies of the $X^2\Pi$ state [114].

- The uncertainties of most validated transitions are close to the lower bounds listed in Table 4.2.

- The transitions of $\gamma(3,0)$, $\beta(6,0)$ and $\beta(11,0)$ bands extracted from 02ChLoLe [140], 02ChLoLe [140] and 02RuYoTh [141] were increased by $0.083\,cm^{-1}$, $0.083\,cm^{-1}$ and $0.067\,cm^{-1}$, respectively, as suggested in 05ThRuYo [146]. The uncertainties of these transitions should be $0.1\,cm^{-1}$ because the absolute frequencies were not calibrated [146]. However, we used a relative accuracy, *i.e.*, $0.03\,cm^{-1}$, as the lower bound of uncertainty to constrain the MARVEL analysis. The uncertainties should be adjusted to $0.1\,cm^{-1}$ if data of higher accuracy are included in the future.

- In the $\beta(10,0)$ band of 06YoThMu [7], $R_{11}(3.5)$ and $P_{11}(3.5)$ were exchanged; the R_{21} and P_{21} branches were exchanged.

- In the $\delta(0,0)$ band of 94MuYoEs [138], $P_{12}(15.5)_e$ and $P_{12}(16.5)_f$ should be $P_{22}(15.5)_e$ and $P_{22}(16.5)_e$, respectively.

- In the $\delta(1,0)$ band of 00ImYoEs [139], the wavenumbers of $R_{12}(15.5)_e$ and $R_{12}(15.5)_f$ should be exchanged; the wavenumbers of $P_{11}(5.5)$ and $P_{11}(16.5)_f$ should be $54\,668.636\,cm^{-1}$.

- In the $\delta(2,0)$ band of 06YoThMu [7], the wavenumbers of $Q_{22}(5.5)_e$ and $Q_{22}(6.5)_e$ should be 56 967.72 and 56 966.61 cm^{-1}, respectively.

- The transitions, $R_{22}(0.5)_{ff}$, $Q_{22}(0.5)_{fe}$, $R_{12}(0.5)_{ee}$ of 97DaDoKe [116] and $R_{22}(0.5)$ of 02ChLoLe [140], are related to unknown lower states ($J = 0.5$ and $\Omega = 1.5$). Those transitions were not validated.

The most serious issue we encountered concerned the 2020 measurements of Ventura and Fellows (20VeFe[147]) who published a new line list for the γ system containing 6436 transitions. The transitions of 20VeFe disagree with those measured by Danielak *et al.* (97DaDoKe) [116]. MARVEL and combination difference analysis indicates that their data set is self-consistent within the claimed accuracy, *i.e.* $0.005\,\mathrm{cm}^{-1}$ to $0.06\,\mathrm{cm}^{-1}$. However, it is inconsistent with the ground state MARVEL energies of Wong *et al.* [114]. Combination difference tests show that the standard deviations of most energy levels calculated by the data set are greater than $0.1\,\mathrm{cm}^{-1}$.

In contrast, the line list of 97DaDoKe [116] is consistent with others. The measurements of 20VeFe differ from those of 97DaDoKeby up to $0.7\,\mathrm{cm}^{-1}$, as acknowledged by 20VeFe. The transitions of the $\gamma(3,4)$ band measured by 97DaDoKe are consistent with the transitions in the $\gamma(3,0)$ band measured by Cheung *et al.* (02ChLoLe) [140]. Furthermore, use of the Heath band potentials provides a closed loop or cycle by following $\gamma(0,0)$-Heath$(0,0)$-$\delta(0,0)$. The measurements of 97DaDoKe gave consistency in this cycle, within the stated uncertainties of the various measurements, but 20VeFe did not. Analyzing the ground state data and 20VeFe individually, we observed an average $0.43\,\mathrm{cm}^{-1}$ shift for the lower three vibrational levels of the $A\,^2\Sigma^+$ state; these energy differences are plotted in Fig. 4.6. We were therefore forced to conclude that the measurements of 20VeFe are not consistent with the other measurements and these data were excluded from our MARVEL analysis.

Table 4.3: Quantum numbers used in the MARVEL analysis

Quan. No.	Meaning
State	Electronic state label, *e.g.*, X stands for $X\,^2\Pi$
J	Total angular momentum
parity	+ or -
v	Vibration quantum number
Ω	Projection of the total angular momentum on the internuclear axis

The 20293 validated transitions (including 3141 γ, 4795 β, 861 δ and 360 Heath transitions) yielded 327, 1400 and 466 energy levels of the $A\,^2\Sigma^+$, $B\,^2\Pi$ and

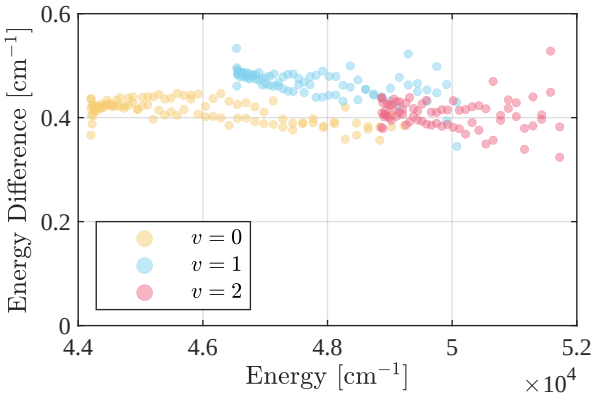

Figure 4.6: The differences between the $A\,^2\Sigma^+$ state MARVEL energies corresponding to 20VeFe and those obtained from the sources of Table 4.2. The average energy shift is 0.43 cm^{-1}.

$C\,^2\Pi$ states, respectively. These levels are plotted as a function of total angular momentum J in Fig. 4.7.

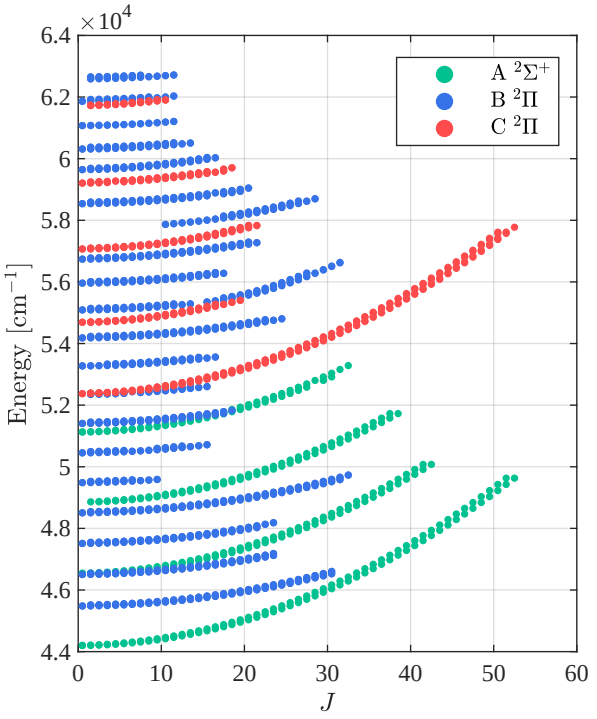

Figure 4.7: $A\,^2\Sigma^+$, $B\,^2\Pi$ and $C\,^2\Pi$ state energy levels generated by MARVEL analysis.

Sulakshina and Borkov compared the ground state energies calculated by their RITZ code [5] with our previous MARVEL result [114]. The MARVEL analysis here updates the energy values of the $X\,^2\Pi$ state by including new rovibronic tran-

sitions; as shown in Fig.4.8, the energy gaps between the results of the MARVEL and RITZ analysis are narrowed as a result of this. This is especially true for high J levels belonging to the $\Omega = \frac{3}{2}$ series (see Fig. 8(b) of Sulakshina and Borkov's [5]). The majority of levels agree within the uncertainty of their determination.

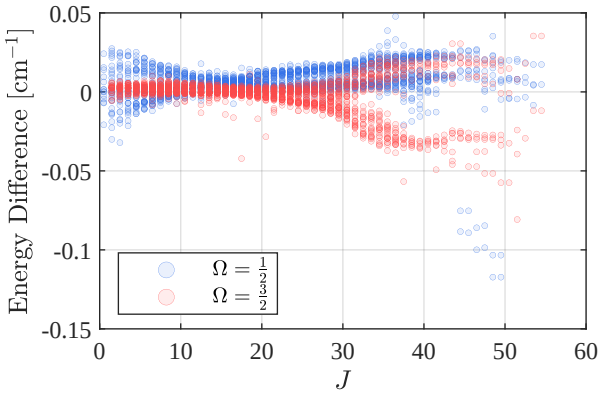

Figure 4.8: Energy difference of the $X\,^2\Pi$ state between MARVEL result in this thesis and the RITZ result in the work of Sulakshina and Borkov [5].

4.4 Refinement of curves for $^{14}N^{16}O$

4.4.1 Calculation setup

The PECs of the $A\,^2\Sigma^+$, $B\,^2\Pi$ and $C\,^2\Pi$, as well as other coupling curves, were refined based on the empirical energy levels obtained by the MARVEL analysis in Section 4.3; the PEC for the $X\,^2\Pi$ state was left unchanged from that of Wong *et al.* [114] The refinement was executed in Duo which is a general variational nuclear-motion program for calculating spectra of diatomic molecules [42].

Duo solves the diatomic molecular Schrödinger equation in two steps. Firstly the rotation-free radial equation of each electronic state is solved to get the vibrational energy levels, E_v, and wavefunctions, $\psi_v(R)$:

$$-\frac{\hbar^2}{2\mu}\frac{\mathrm{d}^2}{\mathrm{d}R^2}\psi_v(R) + V_{\text{state}}(R)\psi_v(R) = E_v\psi_v(R)\,, \tag{4.1}$$

where μ is the reduced mass of the molecule and $V_{\text{state}}(r)$ is the potential energy curve. This step creates vibrational basis functions, $|\text{state}, v\rangle$. Secondly, the fully-coupled, rovibronic Hamiltonian is diagonalized under the Hund's case (a) rovi-

bronic basis set defined by:

$$|\text{state}, J, \Omega, \Lambda, S, \Sigma, v\rangle = |\text{state}, \Lambda, S, \Sigma\rangle\, |J, \Omega, M\rangle\, |\text{state}, v\rangle\,, \tag{4.2}$$

where $|\text{state}, \Lambda, S, \Sigma\rangle$ and $|J, \Omega, M\rangle$ represent the electronic and rotational basis functions, respectively.[48] The quantum number M is the projection of the total angular momentum along the laboratory Z-axis.

Users are asked to set up some super-parameters to get the correct solution. The calculation setup for the refinement of $^{14}N^{16}O$ is summarized below.

- Equation (4.1) was solved by the Sinc-DVR method [148].
- The calculation range was from 0.6 to 4.0 Å.
- The number of grids points was 701, uniformly spaced.
- The numbers of vibrational basis sets for $X\,^2\Pi$, $A\,^2\Sigma^+$, $B\,^2\Pi$ and $C\,^2\Pi$ were 60, 15, 30 and 10, respectively.
- The maximum total angular momentum considered here was $52\frac{1}{2}$.
- The upper bound of the total energy was 65 000 cm^{-1}.

4.4.2 Refinement results of the $A\,^2\Sigma^+$ state

The PEC of $A\,^2\Sigma^+$ state represented by a fourth-order Extended Morse Oscillator (EMO) function [149]. The EMO is defined as a function of internuclear distance, R:

$$V(R) = T_e + (D_e - T_e)\left[1 - \exp\left(-\beta_{\text{EMO}}(R)\,(R - R_e)\right)\right]^2, \tag{4.3}$$

where the distance-dependent coefficient β_{EMO} is expressed as

$$\beta_{\text{EMO}}(R) = \sum_{i=0}^{N} b_i y_p^{\text{eq}}(R)^i. \tag{4.4}$$

The reduced variable $y_p^{\text{eq}}(R)$ has the formula:

$$y_p^{\text{eq}}(R) = \frac{R^p - (R_e)^p}{R^p + (R_e)^p}, \tag{4.5}$$

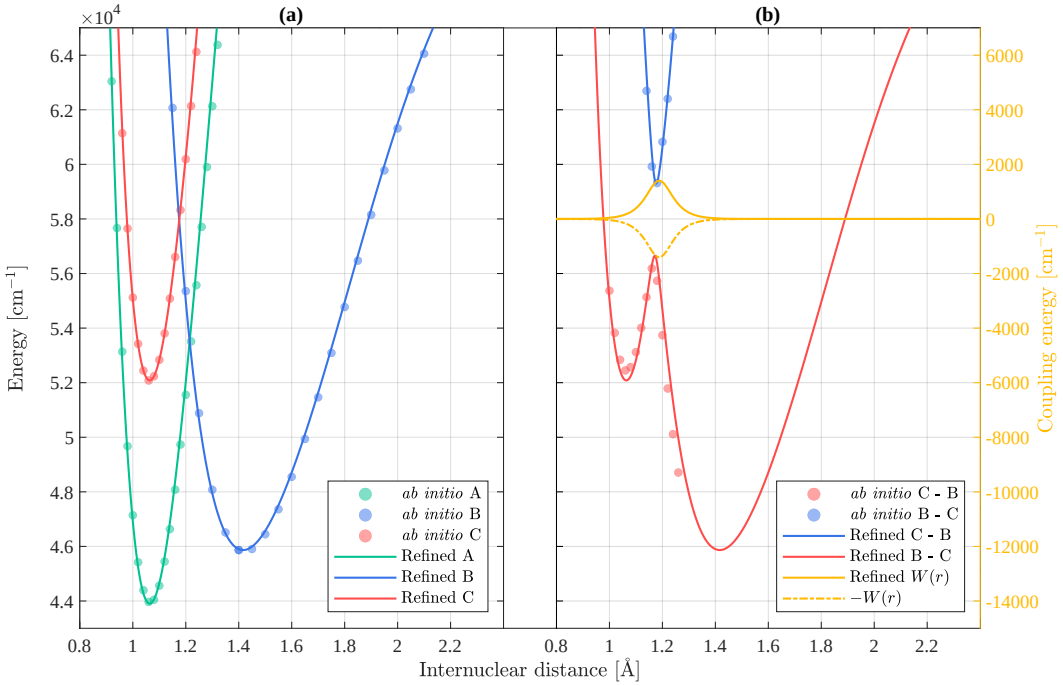

Figure 4.9: The *ab initio* and refined PECs of the $A\,^2\Sigma^+$, $B\,^2\Pi$ and $C\,^2\Pi$ states as well as the refined B - C interaction term $W(R)$. (a) diabatic and (b) adiabatic representations. The refined potential curves in panel (b) are calculated using Eqs. (4.10) and (4.11). The *ab initio* curves are shifted using empirical T_e values.

where p controls the shape of $y_p^{\text{eq}}(R)$. The programmed EMO function in Duo is not exactly the same as defined by Eq. 4.3. A reference point R_{ref} (usually the equilibrium internuclear distance) divides the curve into left and right parts. The numbers of terms N, as well as p, for the left and right parts can be assigned different values, *i.e.*, N_{L}, N_{R}, p_{L} and p_{R}. The unknown dissociation energy of the state is regarded as a dummy parameter in the refinement. The initial guess of D_e was given by a pure Morse function and the value was fine-tuned in each iteration. The optimal parameters of the EMO function are listed in Table 4.4. The *ab initio* and refined PECs of the $A\,^2\Sigma^+$ state are compared in panel (a) of Fig. 4.9.

In addition, our model of the $A\,^2\Sigma^+$ state contains a spin-rotational term. In Duo, the nonzero diagonal and off-diagonal matrix elements of spin-rotation operator $\hat{H}_{\text{SR}}$[48] are given by

$$\left\langle \Lambda,S,\Sigma\middle|\hat{H}_{\text{SR}}\middle|\Lambda,S,\Sigma\right\rangle = \frac{\hbar^2}{2\mu R^2}\gamma^{\text{SR}}(R)\left[\Sigma^2 - S(S+1)\right], \tag{4.6}$$

Table 4.4: The optimized EMO parameters of the PECs of $A\,^2\Sigma^+$, $B\,^2\Pi$, $C\,^2\Pi$ states and the spin-orbit (SO) coupling within the $B\,^2\Pi$ state.

Parameter	$A\,^2\Sigma^+$	$B\,^2\Pi$	$C\,^2\Pi$	$\left\langle B\,^2\Pi\middle\vert\hat{H}_{SO}\middle\vert B\,^2\Pi\right\rangle$
T_e [cm^{-1}]	$4.390\,299\,27\times10^4$	$4.586\,704\,51\times10^4$	$5.208\,197\,36\times10^4$	8.497 424 00
r_e, r_{ref} [Å]	1.063 666 00	1.416 639 77	1.063 704 70	1.1
D_e [cm^{-1}]	$1.292\,051\,39\times10^5$	7.1627×10^4	$1.271\,773\,19\times10^5$	$5.774\,077\,92\times10^1$
p	4	4	4	4
N_l	2	4	2	4
N_r	4	8	4	4
b_0 [$Å^{-1}$]	2.704 913 98	2.150 144 13	2.863 985 60	2.015 987 56
b_1 [$Å^{-1}$]	$2.073\,903\,44\times10^{-2}$	$9.835\,900\,99\times10^{-2}$	$5.525\,275\,33\times10^{-1}$	0
b_2 [$Å^{-1}$]	$8.149\,010\,09\times10^{-2}$	$4.118\,983\,73\times10^{-1}$	3.452 639 96	−3.768 976 84
b_3 [$Å^{-1}$]	$-9.539\,702\,89\times10^{-1}$	0	$-3.788\,700\,19\times10^1$	0
b_4 [$Å^{-1}$]	2.050 677 38	$-4.436\,396\,75\times10^{-1}$	$8.286\,317\,43\times10^1$	6.672 511 52
b_5 [$Å^{-1}$]		$1.215\,719\,27\times10^1$		
b_6 [$Å^{-1}$]		$-1.784\,795\,35\times10^1$		
b_7 [$Å^{-1}$]		3.127 784 54		
b_8 [$Å^{-1}$]		5.403 077 72		

$$\left\langle \Lambda, S, \Sigma \middle| \hat{H}_{\mathrm{SR}} \middle| \Lambda, S, \Sigma \pm 1 \right\rangle = \frac{\hbar^2}{4\mu R^2} \gamma^{\mathrm{SR}}(R) \sqrt{S(S+1) - \Sigma(\Sigma \pm 1)} \times \sqrt{J(J+1) - \Omega(\Omega \pm 1)}. \tag{4.7}$$

The dimensionless spin-rotation coefficient $\gamma^{\mathrm{SR}}(R)$ of the $\mathrm{A}\,^2\Sigma^+$ state was modeled as a constant whose value is

$$\gamma_{\mathrm{A}}^{\mathrm{SR}}(R) = -2.08043004 \times 10^{-3}. \tag{4.8}$$

4.4.3 Refinement results of the $\mathrm{B}\,^2\Pi$ - $\mathrm{C}\,^2\Pi$ coupled states

4.4.3.1 Deperturbation of the $\mathrm{B}\,^2\Pi$ - $\mathrm{C}\,^2\Pi$ interaction

For this thesis we only consider coupling between two electronic states. The interaction between two electronic states belong to the same irreducible representation of the molecular point group directly depends on the avoided crossing of their diabatic PECs. Thus, it is possible to model the coupled states by introducing two adiabatic potentials. This could be accomplished by diagonalizing the matrix:

$$\begin{pmatrix} V_1(R) & W(R) \\ W(R) & V_2(R) \end{pmatrix}, \tag{4.9}$$

where $V_1(R)$ and $V_2(R)$ are two diabatic potentials and $W(R)$ is the coupling curve. The adiabatic PECs, *i.e.* the eigenvalues of the matrix, are

$$V_{\mathrm{low}}(R) = \frac{V_1(R) + V_2(R)}{2} - \frac{\sqrt{[V_1(R) - V_2(R)]^2 + 4W^2(R)}}{2}, \tag{4.10}$$

$$V_{\mathrm{upp}}(R) = \frac{V_1(R) + V_2(R)}{2} + \frac{\sqrt{[V_1(R) - V_2(R)]^2 + 4W^2(R)}}{2}. \tag{4.11}$$

EMO potential functions are used to model $V_1(R)$ and $V_2(R)$ in Eqs. (4.10) and (4.11) while $W(R)$ is given by:

$$W(R) = \frac{\sum_{i \geq 0} w_i (R - R_0)^i}{\cosh(b(R - R_0))}. \tag{4.12}$$

The function rapidly decreases to W_0 when R moves away from R_0. Alghough the non-adiabatic coupling term obtained via strict diabatization would be a smooth curve with no special feature at the crossing point, we prefer to use the bell-shape for robust fitting here. Its formulae have negligible effect on final energy levels.

The coupled PECs of the $X\,^1\Sigma_g^+$ and $B'\,^1\Sigma_g^+$ states of C_2 were represented by an adiabatic potential in our previous work [150], producing accurate line list. Nevertheless, this method is not optimal for NO where the avoided crossing between the B and C states is very sharp. Thus, for example, the adiabatic B – X and C – X transition dipole moment curves (TDMCs) change dramatically around the crossing point making them hard to use in any reliable calculation of transition intensities and a slight shift of the crossing point, R_0, during refinement may significantly change the intensities of nearby lines. We therefore adopt the following procedure for generating line lists involving these coupled electronic states:

1. Solve the radial equations established with diabatic PECs of different electronic states to get vibrational basis.

2. Construct rovibronic Hamiltonian matrix with all necessary elements, including the electronic interaction terms.

3. Diagonalize the matrix in the rovibronic basis set to get the rovibronic energy levels and the corresponding wavefunctions.

4. Refine the diabatic PECs, electronic interaction terms and other coupling curves by fitting the energies to observed energy levels.

5. Calculate the Einstein A coefficients with the diabatic TDMCs and let the wavefunctions determine the weights of TDMCs for each rovibronic state at different geometries.

This method not only rescues us from the dilemma of constructing adiabatic TDMCs but also improves the flexibility of our program. For instance, it is convenient to model the $B\,^2\Pi$ - $C\,^2\Pi$ - $L\,^2\Pi$ coupled states of NO by adding new defini-

Table 4.5: Optimized Lorentz parameters for the B - C interaction curve.

Parameter	Value
b [Å^{-1}]	$2.217\,076\,31 \times 10^{1}$
r_0 [Å]	1.188 085 74
w_0 [cm^{-1}]	$1.401\,731\,79 \times 10^{3}$

Table 4.6: Optimized values of the spin-orbit (SO) and spin-rotation (SR) coupling terms.

Term	Value
$\left\langle \mathrm{C}\,^2\Pi \middle\vert \hat{H}_{\mathrm{SO}} \middle\vert \mathrm{C}\,^2\Pi \right\rangle$ [cm^{-1}]	1.817 667 72
$\left\langle \mathrm{C}\,^2\Pi \middle\vert \hat{H}_{\mathrm{SO}} \middle\vert \mathrm{B}\,^2\Pi \right\rangle$ [cm^{-1}]	2.282 063 75
$\gamma_{\mathrm{C}}^{\mathrm{SR}}$	$2.705\,930\,62 \times 10^{-3}$

tions of the potential of L $^2\Pi$ and coupled term between C $^2\Pi$ and L $^2\Pi$ in the input file of Duo, without changing its code.

4.4.3.2 Refined curves

The diabatic PECs of the B $^2\Pi$ and C $^2\Pi$ states were modeled using EMO functions whose optimal parameters are listed in Table 4.4. The *ab initio* and refined PECs of the B $^2\Pi$ and C $^2\Pi$ states are compared in panel (a) of Fig. 4.9. Its optimal parameters of the function are listed in Table 4.5. Although not used in this thesis, the adiabatic curves were calculated as defined by Eqs. (4.10) and (4.11). They are compared with the *ab initio* adiabatic PECs in panel (b) of Fig. 4.9. The dissociation energy of C $^2\Pi$ state is also a dummy parameter. The refined PECs of A $^2\Sigma^+$ and C $^2\Pi$ states are physically meaningless outside the our calculation range (*i.e.*, when energy is greater than 65 000 cm^{-1}).

The spin-orbit coupling curve (SOC) of the B $^2\Pi$ state was also fitted to an EMO function whose optimal parameters are listed in the last column of Table 4.4. Figure 4.10 compares the *ab initio* and refined SOCs. The diagonal spin-orbital term of the C $^2\Pi$ state and the off-diagonal term between the B $^2\Pi$ and C $^2\Pi$ states were determined empirically by fitting to constants. The spin-rotational coefficient of the C $^2\Pi$ state was also modelled as a constant. The values of these terms are listed in Table 4.6.

The Λ - doubling fine structures of the β and δ system bands were observed

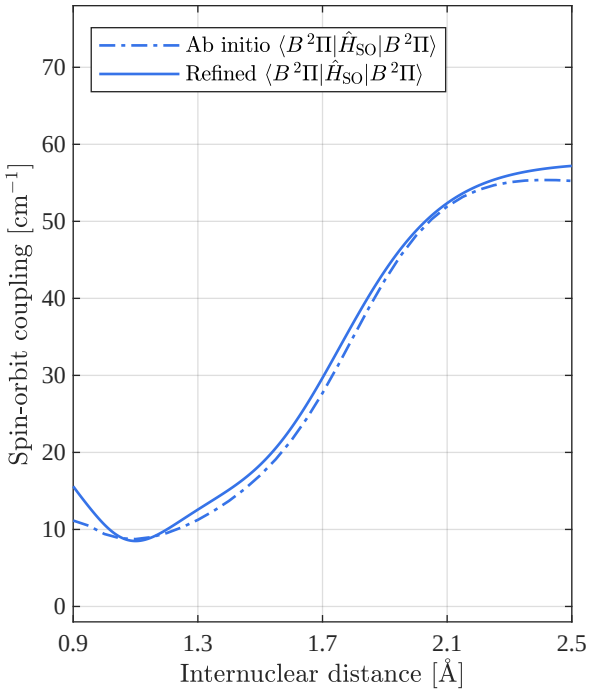

Figure 4.10: The spin-orbit coupling curves of the B $^2\Pi$ state.

in most of the work listed in Table 4.2. Duo calculates the Λ-doubling matrix elements, *i.e.*, $\langle \Lambda'\Sigma' J'\Omega'|\hat{H}_{\rm LD}|\Lambda''\Sigma'' J''\Omega''\rangle$, according to the terms given by Brown and Merer, [151]:

Table 4.7: Optimized polynomial parameters of the Λ - doubling curves of the $B\,^2\Pi$ and $C\,^2\Pi$ states

state	Parameter	$p+2q$	q
$B\,^2\Pi$	r_0 [Å]	1.416 504 703 5	1.416 504 703 5
	a_0 [cm^{-1}]	$1.065\,516\,70\times10^{-2}$	$6.453\,326\,91\times10^{-5}$
	a_1 [cm^{-1} Å^{-1}]	$-2.921\,142\,81\times10^{-1}$	$-1.189\,741\,08\times10^{-2}$
	a_2 [cm^{-1}Å^{-2}]	$5.095\,170\,16\times10^{-1}$	$3.040\,771\,80\times10^{-2}$
$C\,^2\Pi$	r_0 [Å]	0	1.064 436 05
	a_0 [cm^{-1}]	$-3.660\,394\,01\times10^{-2}$	$-1.612\,437\,38\times10^{-2}$
	a_1 [cm^{-1} Å^{-1}]	0	$3.003\,216\,09\times10^{-2}$

$$\left\langle \mp1,\Sigma\pm2,J,\Omega\middle|\hat{H}_{\mathrm{LD}}\middle|\pm1,\Sigma,J,\Omega\right\rangle = \frac{1}{2}(o_v+p_v+q_v)\times \sqrt{[S(S+1)-\Sigma(\Sigma\pm1)][S(S+1)-(\Sigma\pm1)(\Sigma\pm2)]}, \tag{4.13}$$

$$\left\langle \mp1,\Sigma\pm1,J,\Omega\mp1\middle|\hat{H}_{\mathrm{LD}}\middle|\pm1,\Sigma,J,\Omega\right\rangle = -\frac{1}{2}(p_v+2q_v)\times \sqrt{[S(S+1)-\Sigma(\Sigma\pm1)][J(J+1)-\Omega(\Omega\mp1)]}, \tag{4.14}$$

$$\left\langle \mp1,\Sigma,J,\Omega\mp2\middle|\hat{H}_{\mathrm{LD}}\middle|\pm1,\Sigma,J,\Omega\right\rangle = \frac{1}{2}q_v\times \sqrt{[J(J+1)-\Omega(\Omega\mp1)][J(J+1)-(\Omega\mp1)(\Omega\mp2)]}. \tag{4.15}$$

For the $B\,^2\Pi$ and $C\,^2\Pi$ states, $\Sigma = \pm1/2$. Therefore, the matrix elements described in Eq. (4.13) are zero and only the coefficient curves of Eqs. (4.14) and (4.15) were fitted to polynomials, *i.e.*,

$$P(r) = a_0 + \sum_{i\geq0} a_i(r-r_0)^i. \tag{4.16}$$

The optimized parameters of the Λ - doubling terms are listed in Table 4.7.

4.4.3.3 Fitting residuals of the rovibronic energy levels

The fitting residuals of the $A\,^2\Sigma^+$ state are shown in panel (a) of Fig. 4.11. The high-J energies of $v = 3$ vibrational levels are mainly determined by blended lines of 97DaDoKe.NO [116]. The fitting residuals of the $B\,^2\Pi$ and $C\,^2\Pi$ states are shown in panel (b) of Fig. 4.11, where the cold colors represent the $B\,^2\Pi$ state and the warm

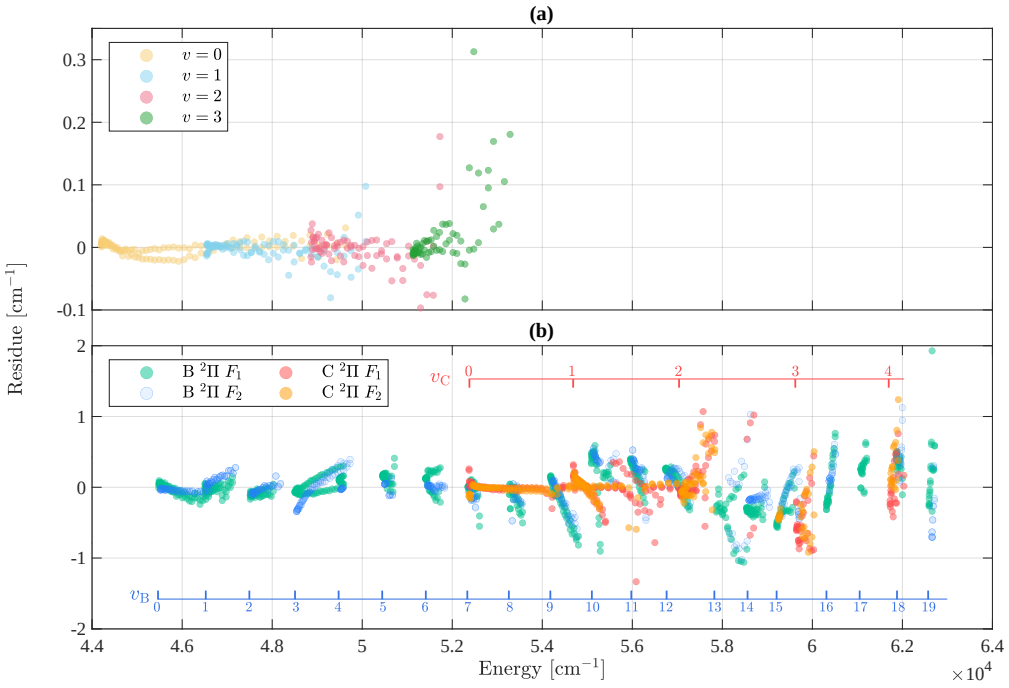

Figure 4.11: Fitting residuals of the (a) $A\,^2\Sigma^+$ state, and (b) $B\,^2\Pi$ - $C\,^2\Pi$ coupled states.

Table 4.8: Overall comparison of uncertainty and residual.

All in cm^{-1}	$A\,^2\Sigma^+$	$B\,^2\Pi$ - $C\,^2\Pi$
RMS uncertainty	0.04284	0.07927
RMS residual	0.03390	0.27217
Average uncertainty	0.02453	0.05753
Average absolute residual	0.01599	0.18603

ones represent the $C\,^2\Pi$ state. The F_1 (*i.e.*, $\Omega = \frac{1}{2}$) and F_2 (*i.e.*, $\Omega = \frac{3}{2}$) levels are also distinguishable. The residual distributions indicate a J-dependent systematic error of our model, which may result from some off-diagonal couplings, *e.g.*, the coupling between $C\,^2\Pi$ and $D\,^2\Sigma^+$ states [144].

The residuals of all rovibronic energy levels are plotted against their corresponding uncertainties in Fig.4.12. The root-mean-square and average value of the uncertainties and the residuals are compared in Table 4.8.

The accuracy of our model is definitely higher than those of Lagerqvist and Miescher [115], or Gallusser and Dressler [77]. On one hand, the most recent measurements (*e.g.*, the works of Yoshino *et al.* [7]) and spectroscopic analysis techniques (MARVEL [122]) helped us reconstruct reliable spectroscopic networks

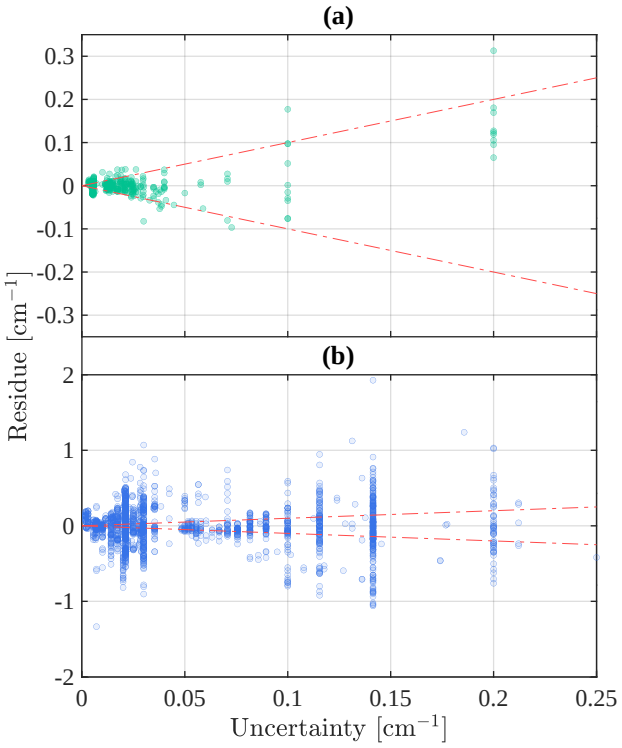

Figure 4.12: Residuals against uncertainties of the (a)A $^2\Sigma^+$ state, and (b) B - C coupled states with vibrational states given in the bars.

and energy levels. On the other hand, our model was directly fitted to the observed rovibronic levels. The vibronic residuals given by Gallusser and Dressler [77] are greater than our rovibronic residuals. Unlike Gallusser and Dressler, we did not include higher electronic states, such as the L $^2\Pi$ and K $^2\Pi$ states, in our model, which reduces its range of applicability where the state energy is greater than 63 000 cm^{-1}. However, thanks to the diabatic coupling strategy of Duo, the model can easily be updated in a future study.

We note that some of the assignments to B or C electronic states differ between Duo and our MARVEL analysis. Duo uses three good quantum number, namely the total angular momentum J, the total parity and the counting number of the levels with the same values of J and parity. The other quantum numbers such as state, v, Ω, are estimated using the contribution of the basis functions to a given wavefunction. It is to be anticipated that in regions of heavily mixed wavefunctions this may lead to differences compared to other assignment methods. The MARVEL and Duo energy levels of B (v = 13) - C (v = 2) coupled series are plotted in Fig. 4.13. Table 4.9 lists

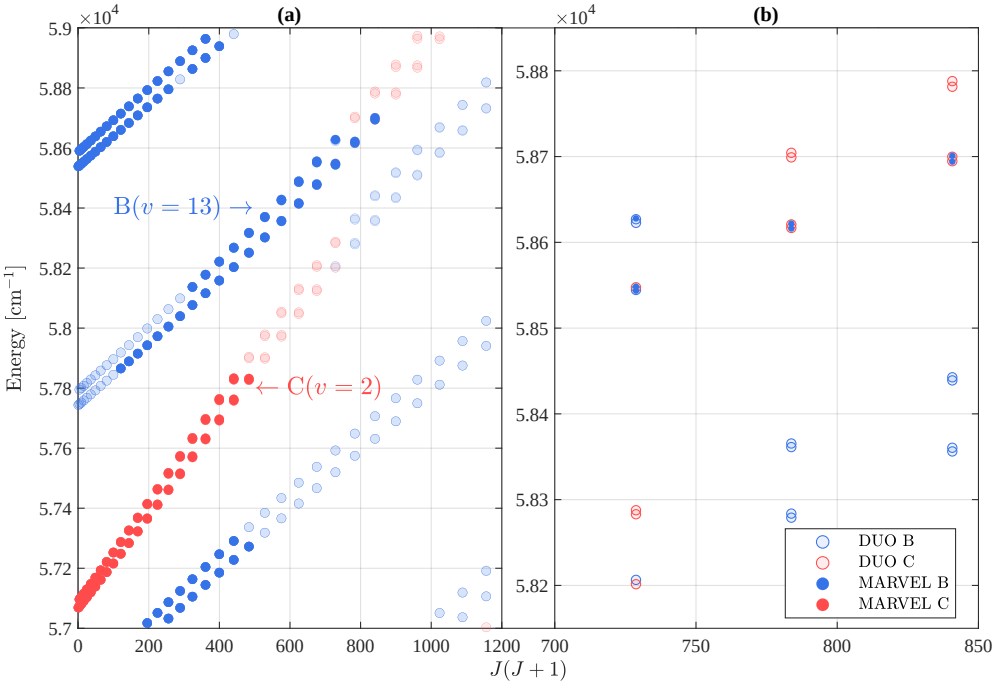

Figure 4.13: Calculated and observed energy levels of the B(v = 13) - C(v = 2) coupled series. The right hand panel is a blow up of the avoided crossing between the states which gives a clearer view of the Λ - doubling splittings and the difference between the quantum numbers given by MARVEL and Duo.

some energy levels in the output `.en` file of Duo. Both of them demonstrate the differences between the quantum numbers of MARVEL and Duo results.

4.5 Conclusion

In this chapter, potential energy curves and couplings for the low-lying electronic states of NO are calculated using quantum chemistry package MOLPRO. The strong interaction between Rydberg and valence states makes the *ab initio* calculation challenging. We obtain both adiabatic and diabatic PECs and SOCs for the $A\,^2\Sigma^+$, $B\,^2\Pi$ and $C\,^2\Pi$ states. The curves were refined by fitting the rovibronic energy levels calculated by the variational nuclear motion program Duo to those reconstructed by MARVEL analysis. The RMS error of the $A\,^2\Sigma^+$ state fitting and $B\,^2\Pi$ - $C\,^2\Pi$ coupled states fitting are 0.033 90 cm^{-1} and 0.272 17 cm^{-1}, respectively. The energies were determined by our use of a MARVEL procedure and the best available measurements. The success of fitting the $B\,^2\Pi$ - $C\,^2\Pi$ coupled states validates our

Table 4.9: Sample lines extracted from the output `.en` file of Duo.

				MARVEL	Duo			Duo					MARVEL				
N	N^a	J	Parity	Energy	Energy	residual	Weight	state[2]	v	Λ	Σ	Ω	state[b]	v	Λ	Σ	Ω
39	39	1.5	+	52349.0418	52349.0274	0.0144	9.50E-05	3	7	1	-0.5	0.5	3	7	1	-0.5	0.5
40	40	1.5	+	52373.2372	52373.3626	-0.1255	1.40E-03	4	0	1	0.5	1.5	3	7	1	0.5	1.5
41	41	1.5	+	52380.1912	52380.1101	0.0810	1.30E-03	4	0	1	-0.5	0.5	4	0	1	-0.5	0.5
42	42	1.5	+	52392.3007	52392.3172	-0.0165	1.30E-03	3	7	1	0.5	1.5	4	0	1	0.5	1.5
64	64	2.5	-	59217.4976	59217.9730	-0.4754	9.50E-05	3	15	-1	0.5	-0.5	4	3	-1	0.5	-0.5
65	65	2.5	-	59250.3720	59250.8248	-0.4528	9.50E-05	4	3	-1	-0.5	-1.5	4	3	-1	-0.5	-1.5
66	66	2.5	-	59654.3005	59654.8551	-0.5546	3.70E-06	4	3	-1	0.5	-0.5	3	15	-1	0.5	-0.5
67	67	2.5	-	59692.2845	59692.6292	-0.3447	4.80E-06	3	15	-1	-0.5	-1.5	3	15	-1	-0.5	-1.5

a. The counting numbers (N) were manually assigned to match the corresponding MARVEL energy level.

b. In these columns, '3' and '4' indicate the $B\,^2\Pi$ and $C^2\Pi$ states, respectively.

deperturbation method for treating the coupled electronic state. This chapter, when combined with the earlier $X^2\Pi$ study of Wang *et al.*,[114] provides a comprehensive spectroscopic model for the lowest four electronic states of NO and thus a good starting point for the generation of a NO UV line list. This line list will be presented in the next chapter.

Chapter 5

A Line List for the Lowest Four Doublet States of NO

5.1 Introduction

There are several available high-resolution infra-red line lists of the NO $X^2\Pi$ ground state. The HITRAN database [117] is widely used for investigations of the Earth's atmosphere and other room temperature studies. For higher temperature applications, the NO line list in the HITEMP database has been recently updated [8] based upon use of the ExoMol NOname line list [114]. The CDMS database [32] contains long-wavelength data including lines with hyperfine-structure; data on two vibrational bands of $^{14}N^{16}O$ are available on the CDMS website. Wong *et al.* published the NOname line list [114] as a part of the ExoMol database [25]. NOname, available for six isotopologues, contains 21 688 states and 2 409 810 transitions for $^{14}N^{16}O$.

A spectroscopic model has been developed of NO in Chapter 4, which gives an accurate description of the $A^2\Sigma^+$, $B^2\Pi$ and $C^2\Pi$ states for levels up to 63 000 cm^{-1} above the ground state; the previous NOname line list already provides a good spectroscopic model for the $X^2\Pi$ state. This chapter demonstrates the calculation of a IR-VIS-UV NO line list which is both accurate and complete covering the rovibrational transitions within its $X^2\Pi$ state and the rovibronic transitions belonging to the other three important band systems, i.e., γ, β and δ as shown in Fig. 5.1.

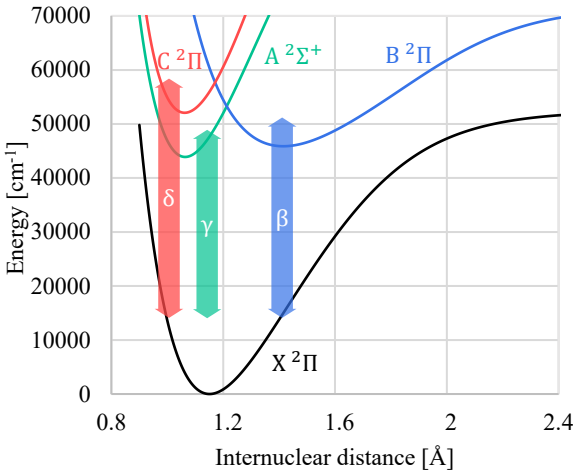

Figure 5.1: The band systems of NO involved in this thesis and their names. For a comprehensive diagram, see Ref. [3].

5.2 Transition dipole moments

Chapter 4 has explored the difficulty of preforming *ab initio* calculations of NO in some detail; fundamentally the problem arises because the $A\,^2\Sigma^+$ and $C\,^2\Pi$ states are effectively Rydberg-like in character which means their curves follow that of the tightly bound NO^+ ion [152], while the $B\,^2\Pi$ state is a valence state with a much flatter curve which crosses the others, see Fig. 5.2 (a). Discontinuities arise in the potential energy curves (PECs) and other curves due to the state (avoided) crossings and interactions. The quality of transition dipole moment curves (TDMC) is strongly affected by the complicated behaviour of the excited state wavefunctions which were computed at the complete active space self-consistent field (CASSCF) and multi-reference configuration interaction (MRCI) levels using MOLPRO [126]. We therefore adopted a pragmatic approach to determining the TDMCs in which the TDMCs were modified through a comparison with experimental data.

5.2.1 Range of calculation

The calculation setup is consistent with those of Ref. [114] and Chapter 4: the internuclear distance, R, varied from 0.6 Å to 4 Å, which in Duo was discretised by 701 uniformly spaced grid points as part of the Sinc-DVR (discrete variable representation) basis set. In the final calculations, 60, 15, 30, and 10 contracted vibrational basis functions were retained for the $X\,^2\Pi$, $A\,^2\Sigma^+$, $B\,^2\Pi$ and $C\,^2\Pi$ states, respectively.

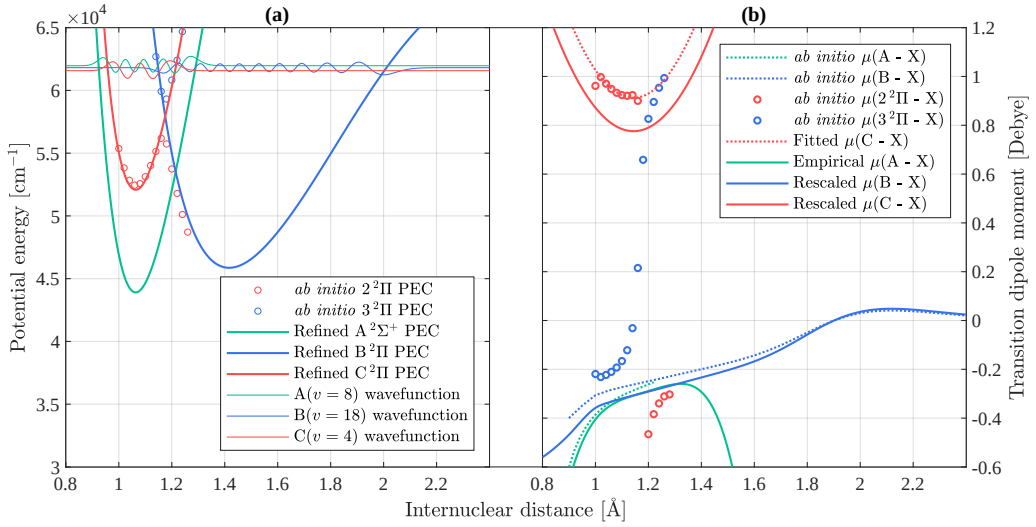

Figure 5.2: (a) *Ab initio* and refined PECs as well as vibrational wavefunctions and (b) corresponding transition dipole moments, $\mu(\cdot)$. In panel (a), the wavefunctions are plotted in arbitrary units. $2\,^2\Pi$ is the adiabatic $C\,^2\Pi$ to $B\,^2\Pi$ state and $3\,^2\Pi$ is the adiabatic $B\,^2\Pi$ to $C\,^2\Pi$ state. In panel (b), 'Fitted $\mu(C-X)$' is a quadratic polynomial which was fitted to the values of red and blue circles it passes through. 'Empirical $\mu(A-X)$' was calculated with the parameters determined in Ref. [6].

As we do not include interactions with higher electronic states [77] in our model, the highest vibrational levels of the $A\,^2\Sigma^+$, $B\,^2\Pi$ and $C\,^2\Pi$ states were limited to 8, 18, and 4, respectively. The vibrational wavefunctions of these levels are shown in Fig. 5.2 (a), where they are vertically shifted to their vibrational energies. The global energy limit was chose to be $65\,000\,\mathrm{cm}^{-1}$.

5.2.2 $A\,^2\Sigma^+$ state

For the $A\,^2\Sigma^+ - X\,^2\Pi$ transitions, we used the empirical TDMC [6] as a fourth-order polynomial (see the green solid curve shown in Fig. 5.2 (b)). We chose not to use an *ab initio* TDMC of $A\,^2\Sigma^+ - X\,^2\Pi$ although the one depicted by the green dash curve in Fig. 5.2 (b) looks very similar to the empirical one. We found that the use of different active spaces in MOLPRO gave TDMCs that were very different in both shape and amplitude; this behaviour has been discussed in Ref. [153]. We thus had to compare these curves with the empirical TDMC and select a similar one; this procedure is neither '*ab initio*' nor 'empirical'. The empirical TDMC function of Ref. [6] was based on the lower vibrational levels of the $A\,^2\Sigma^+$ state. As a result, their polynomial diverges at distances $R > 1.3\,\text{Å}$. We chose to use

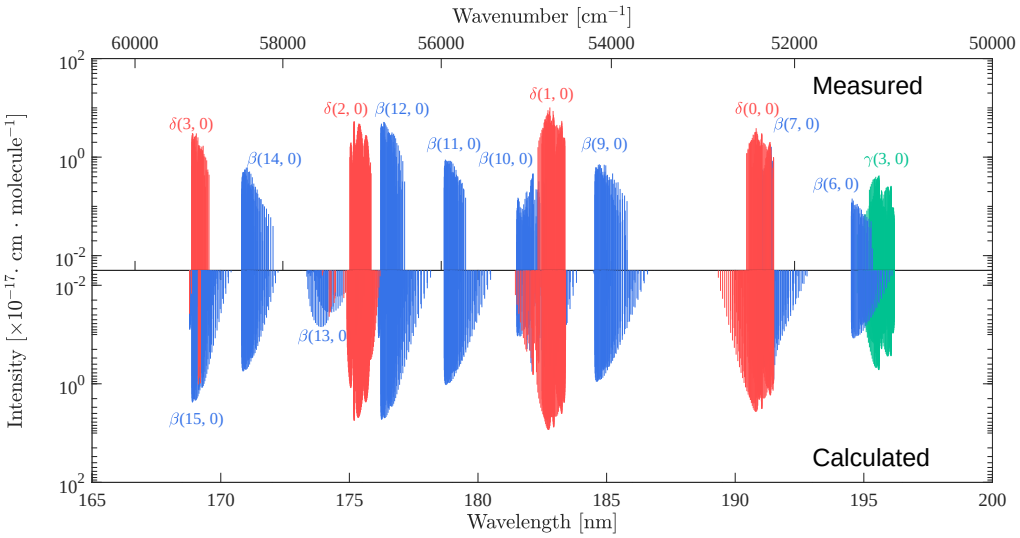

Figure 5.3: Calculated absorption intensities at 295 K compared with the values given in Ref. [7]. As the fine-structure doublets for more than half the transitions were not resolved in the experiment, all doublets are removed by averaging the positions of the two lines and adding their intensities, for both measured and calculated transitions.

this TDMC unaltered as the vibrational wavefunctions decay rapidly to zero in this region so our line list is insensitive to the behaviour of the TDMC at these values of R.

Settersten *et al.* updated the TDMC polynomial coefficients using radiative lifetimes of the NO $A\,^2\Sigma^+$ ($v = 0, 1, 2$) states [154] which they measured using time-resolved laser-induced fluorescence. Their transition dipole moment is larger in magnitude than that of Luque and Crosley. We use the TDMC of Luque and Crosley as a balance between measured radiative lifetimes [6, 154] and the intensities ('integrated cross section') of the $\gamma(3,0)$ measured by Yoshino *et al.* [7]; see Fig. 5.3.

5.2.3 $B\,^2\Pi$-$C\,^2\Pi$ coupled states

The adiabatic PECs $B\,^2\Pi$ and $C\,^2\Pi$ have the same symmetry and therefore form an avoided crossing as shown by our *ab initio* PECs computed using MOLPRO, see circles in Fig. 5.2(a). In order to avoid discontinuities in the various curves, including the TDMCs, here we follow our diabatic model [155] with the PECs shown in Fig. 5.2 (a). Off-diagonal matrix elements were introduced to represent

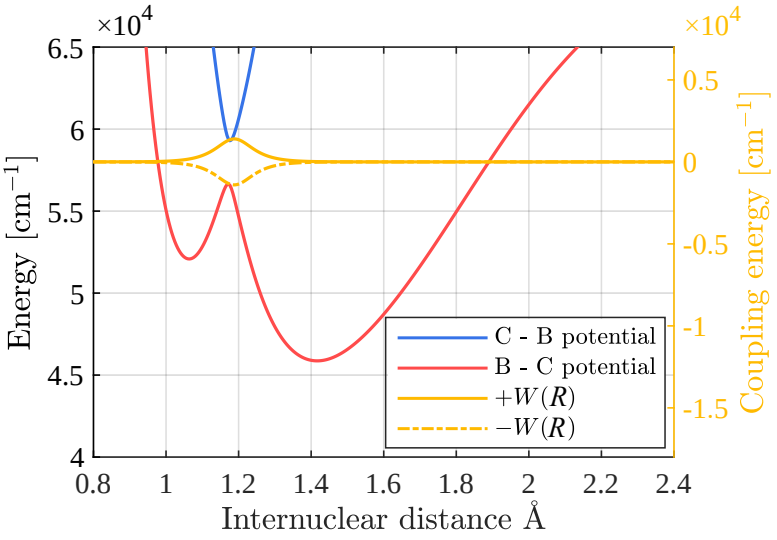

Figure 5.4: Eigenvalue curves of Eq. (5.1)

the electronic state interaction as follows:

$$\begin{pmatrix} V_{\mathrm{B}}(R) & W(R) \\ W(R) & V_{\mathrm{C}}(R) \end{pmatrix}, \tag{5.1}$$

where $V_{\mathrm{B}}(R)$ and $V_{\mathrm{C}}(R)$ are two diabatic potentials, and $W(R)$ is a bell-shaped coupling curve. The effect of this representation is illustrated in Fig. 5.4, although the above matrix elements are introduced into the rovibronic Hamiltonian matrix rather than directly diagonalizing Eq. (5.1) to generate adiabatic potentials shown in this figure.

Due to the (adiabatic) avoided crossing between the $\mathrm{B}\,^2\Pi$ and $\mathrm{C}\,^2\Pi$ states, the adiabatic TDMCs $\mathrm{B}\,^2\Pi$– $\mathrm{X}\,^2\Pi$ and $\mathrm{C}\,^2\Pi$– $\mathrm{X}\,^2\Pi$ exhibit erratic behaviour in the interaction region with their values rising and dropping sharply near 1.18 Å, as shown by the blue and red circles in Fig. 5.2 (b). The interaction center (about 1.18 Å) is close to the equilibrium bond length (about 1.15 Å) of the $\mathrm{X}\,^2\Pi$ state. Thus, even a slight change in the TDMC in this region along the internuclear distance axis can dramatically change the calculated transition intensities.

In the diabatic model, the $\mathrm{B}\,^2\Pi$– $\mathrm{X}\,^2\Pi$ and $\mathrm{C}\,^2\Pi$– $\mathrm{X}\,^2\Pi$ TDMCs are smooth curves (see Fig. 5.2 (b)) which do not show erratic behaviour in the interaction region and therefore are no longer the most sensitive factor in intensity calculations.

The coupling between states in this model is controlled by and relies on the quality of the rovibronic $B\,^2\Pi$ and $C\,^2\Pi$ wavefunctions, which can be accurately determined by our technique of fitting theoretical curves using experimental energies.

The original *ab initio* PECs for $X\,^2\Pi$ and $B\,^2\Pi$ and the corresponding TDMC of $B\,^2\Pi$– $X\,^2\Pi$ were computed using a high level of theory, CASSCF&MRCI+Q/cc-pVQZ with the $[(6,2,2,0) - (2,0,0,0)]$ active space, where $[(n_1,n_2,n_3,n_4) - (n'_1,n'_2,n'_3,n'_4)]$ indicates the occupied and closed orbitals in the irreducible representations a_1, b_1, b_2 and a_2 of the C_{2v} point group (shown as red and blue circles in Fig. 5.2). These adiabatic data were then diabatized to produce curves shown in Fig. 5.2 as dotted curves. In order to improve the quality of the intensity calculations, the diabtaic TDMCs were then further empirically adjusted as follows. The $B\,^2\Pi$– $X\,^2\Pi$ TDMC was scaled using a combination of the measured lifetimes [118] and integrated cross sections [7]. The scaling factor of 1.17 was chosen as a balance between these two experiments. The scaled $B\,^2\Pi$– $X\,^2\Pi$ TDMC is shown as a blue solid line in Fig 5.2. Although the $B\,^2\Pi$– $X\,^2\Pi$ TDMC diverges from its original trend for the internuclear distances shorter than 1 Å, this does not affect our calculation as the corresponding $B\,^2\Pi$ vibrational wavefunctions nearly vanish there.

The TDMC of $C\,^2\Pi$– $X\,^2\Pi$ required special care; we first fitted a quadratic polynomial to the adiabatic *ab initio* values, shown as the red dash curve in Fig. 5.2, and then scaled it based on the measured absorption intensities [7]. Since the TDMC of $C\,^2\Pi$– $X\,^2\Pi$ influences the intensities of higher β bands (i.e. $v_B \geq 7$), it was important to obtain a global agreement for all intensities, including the β system. This is illustrated in Fig. 5.3, where the calculated spectrum of NO in the region of 200 nm is compared to the experimental intensities [7].

5.3 Line list calculation

A rovibronic line list XABC for NO was constructed using the Duo program and the spectroscopic model described above.

The XABC line list consists of 4 596 666 transitions between 30 811 states of

the four low-lying electronic states $X\,^2\Pi$, $A\,^2\Sigma^+$, $B\,^2\Pi$ and $C\,^2\Pi$, (21 668, 1209, 6873 and 1041, respectively), covering $J \leq 184.5$ with rovibronic wavenumber cutoffs of 53 000 cm^{-1} ($X\,^2\Pi$, same as in Ref. [114]) and 63 000 cm^{-1} (all other states). These energy cutoffs are smaller than the basis set limit to avoid any truncation problems near 63 000 cm^{-1}. In line with the ExoMol data structure [156], the line list is represented by two files, a `.states` (states) file and a `.trans` (transitions) file. Table 5.1 gives an extract of the XABC `.states` file. The `.trans` (transitions) file contains the Einstein-*A* coefficients calculated with the Duo spectroscopic model and constitutes our new XABC line list. Table 5.2 gives an extract from the `.trans` file.

The current spectroscopic model uses improved Λ - doubling parameters for the $X\,^2\Pi$ state compared to NOname. As a consequence, the new model shows better agreement with the effective Hamiltonian SPFIT/SPCAT energies of NO also presented in Ref. [114], see Fig. 5.5. Due to the change in the model and consequently the wavefunctions, the Einstein-*A* coefficients between the states of the $X\,^2\Pi$ state as well as the corresponding lifetimes have also changed. The energies of the lower rovibronic states ($v \leq 29$ and $J \leq 99.5$) of the $X\,^2\Pi$ state were replaced with the NOname ones which were calculated by Wong *et al.* [114] using the programs SPFIT and SPCAT [37], based on the previous work [157]. These states are labeled with `EH` to indicate that they were calculated from an effective Hamiltonian, which replaces the label `e` (i.e. empirical) used in NOname for these `EH` levels. The energies of the other states of the $X\,^2\Pi$ potential were shifted from the results of Duo, using the same strategy as NOname, to avoid energy jumps above $v = 29$ or $J = 99.5$. These shifted states were labeled with `Sh` while they were labeled with `c` (*i.e.*, calculated) in NOname.

We also replaced the Duo energies of the $A\,^2\Sigma^+$, $B\,^2\Pi$ and $C\,^2\Pi$ states with MARVEL energies where available, these states are labeled `Ma` in the `.states` file. The jumps between MARVEL and Duo energies in the excited electronic states are negligible. Therefore, we did not shift the other calculated energies of the $A\,^2\Sigma^+$, $B\,^2\Pi$ or $C\,^2\Pi$ states and labeled these states with `Ca`.

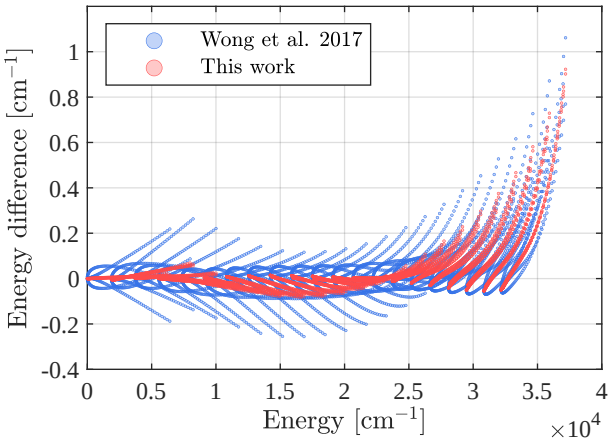

Figure 5.5: Energy differences between the results of Duo and SPFIT/SPCAT for $J \leq 60.5$, $v \leq 20$ states of X $^2\Pi$.

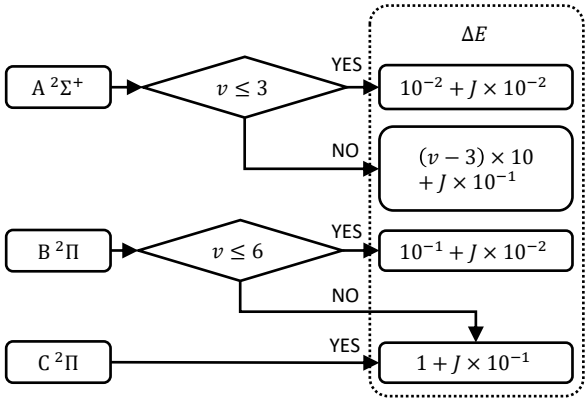

Figure 5.6: The uncertainties assigned to the calculated energies of A $^2\Sigma^+$, B $^2\Pi$ and C $^2\Pi$ in cm^{-1}.

For this line list we also introduced an extra column containing the energy uncertainties (*i.e.*, Column 5, ΔE) for each state. The uncertainties of A $^2\Sigma^+$, B $^2\Pi$ and C $^2\Pi$ were taken from MARVEL analysis where available. Otherwise, they were constructed according to corresponding vibrational and rotational quantum numbers using the algorithm shown in Fig. 5.6. The estimation of uncertainties of the X $^2\Pi$ state is a bit more complicated but is based on the same idea, see Fig. 5.7.

The partition function was computed using the standard summation over energies using levels from our final line list. Figure 5.8 compares the Total Internal Partition Sums (TIPS) partition functions, $Q(T)$, of Ref. [9] and this work. As can be seen from the red curve, i.e., $(Q_{\text{XABC}} - Q_{\text{Gamache}})/Q_{\text{Gamache}}$, the partition func-

Table 5.1: Extract from NO XABC `.states` file.

i	E	g_i	J	ΔE	τ	g_J	$+/-$	e/f	state	v	Λ	Σ	Ω	label	E_{Duo}
61	51869.286798	6	0.5	20.000000	4.8551E-02	-0.000767	+	e	X2Pi	49	1	-0.5	0.5	Sh	51871.759731
62	51970.104351	6	0.5	21.000000	4.3477E-02	-0.000767	+	e	X2Pi	50	1	-0.5	0.5	Sh	51972.577284
63	52081.384882	6	0.5	22.000000	3.9557E-02	-0.000767	+	e	X2Pi	51	1	-0.5	0.5	Sh	52083.857815
64	52345.934940	6	0.5	1.050000	5.1915E-07	-0.000767	+	e	B2Pi	7	1	-0.5	0.5	Ca	52345.934940
65	52372.741033	6	0.5	0.007071	4.4075E-08	-0.000767	+	e	C2Pi	0	1	-0.5	0.5	Ma	52372.500922
66	53273.412094	6	0.5	0.141421	8.2023E-07	-0.000767	+	e	B2Pi	8	1	-0.5	0.5	Ma	53273.523369
68	54183.455941	6	0.5	0.020000	5.8924E-07	-0.000767	+	e	B2Pi	9	1	-0.5	0.5	Ma	54183.325295
69	54690.017247	6	0.5	0.030000	4.0148E-08	-0.000767	+	e	C2Pi	1	1	-0.5	0.5	Ma	54689.759899
70	55090.440941	6	0.5	0.030000	5.1073E-07	-0.000767	+	e	B2Pi	10	1	-0.5	0.5	Ma	55090.115548

i	Counting number
E	State energy in cm^{-1}
g_i	Total state degeneracy
J	Total angular momentum
ΔE	Energy uncertainty in cm^{-1}
τ	Lifetime in s
g_J	Lande g-factor
$+/-$	Total parity
e/f	Rotationless parity
state	Electronic state
v	Vibrational quantum number
Λ	Projection of electronic angular momentum
Σ	Projection of the electronic spin
Ω	Projection of the total angular momentum
label	`Sh` for shifted, `Ca` for calculated, `EH` for effective Hamiltonian, `Ma` for MARVEL
E_{Duo}	State energy in cm^{-1} calculated with Duo

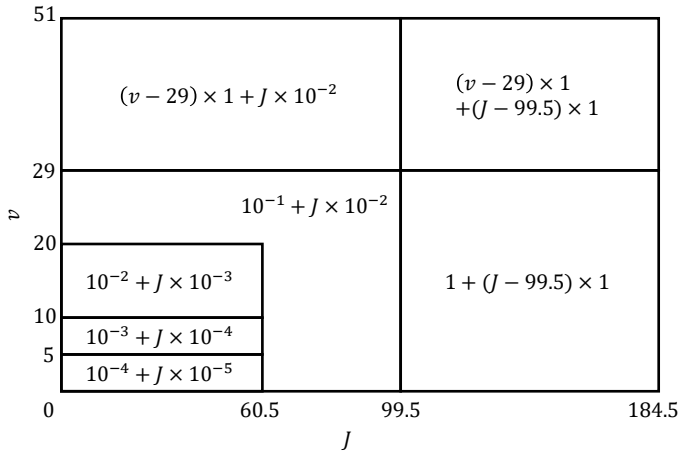

Figure 5.7: Uncertainties assigned to the energy levels of $X^2\Pi$ state in cm^{-1}. The values are consistent with the recent HITEMP Uncertainty Codes given for NO [8].

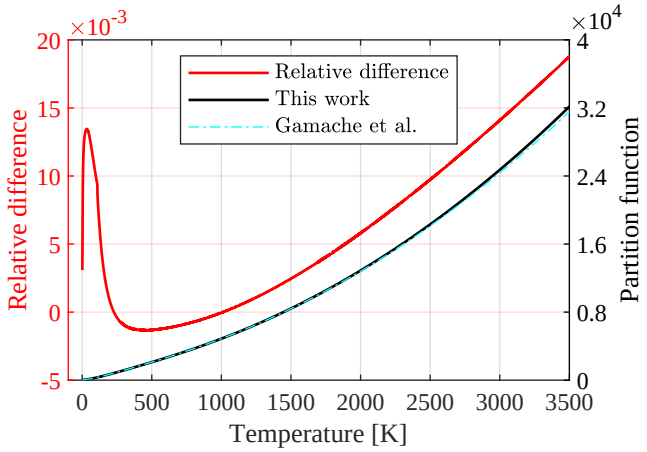

Figure 5.8: Partition function calculated using the XABC state energies in comparison with the TIPS values of Ref. [9]. The red curve illustrates the relative difference between them.

tion difference is very small because the thermodynamic properties are generally not very sensitive to small variations of higher-lying energies as in the $X^2\Pi$ state, while the $A^2\Sigma^+$, $B^2\Pi$ and $C^2\Pi$ energies (not considered in TIPS) are too high to make an obvious difference for the temperature below 3500 K considered here.

With the assumption of local thermal equilibrium, we calculated absorption spectra of NO using the new line list XABC. An overview of the XABC absorption spectrum for different temperatures below 63 000 cm^{-1} or greater than 1600 Å is shown in Fig. 5.9.

Table 5.2: Extract from the NO XABC `.trans` file.

f	i	A_{fi}	ν_{fi}
117	1	3.1174E+05	44203.001767
129	1	6.4207E+05	48854.091482
162	1	2.0740E+05	58538.988402
151	1	1.0243E+05	53273.417513
156	1	2.5855E+04	55586.090674
150	1	1.4370E+06	52372.686268
149	1	2.3080E+05	52345.937733
134	1	1.4276E+04	50452.598447
122	1	1.3786E+02	46503.348087
168	1	5.2902E+05	61721.081024

f Counting number of the upper state
i Counting number of the lower state
A_{fi} Einstein-A coefficient in s^{-1}
ν Transition wavenumber in cm^{-1}.

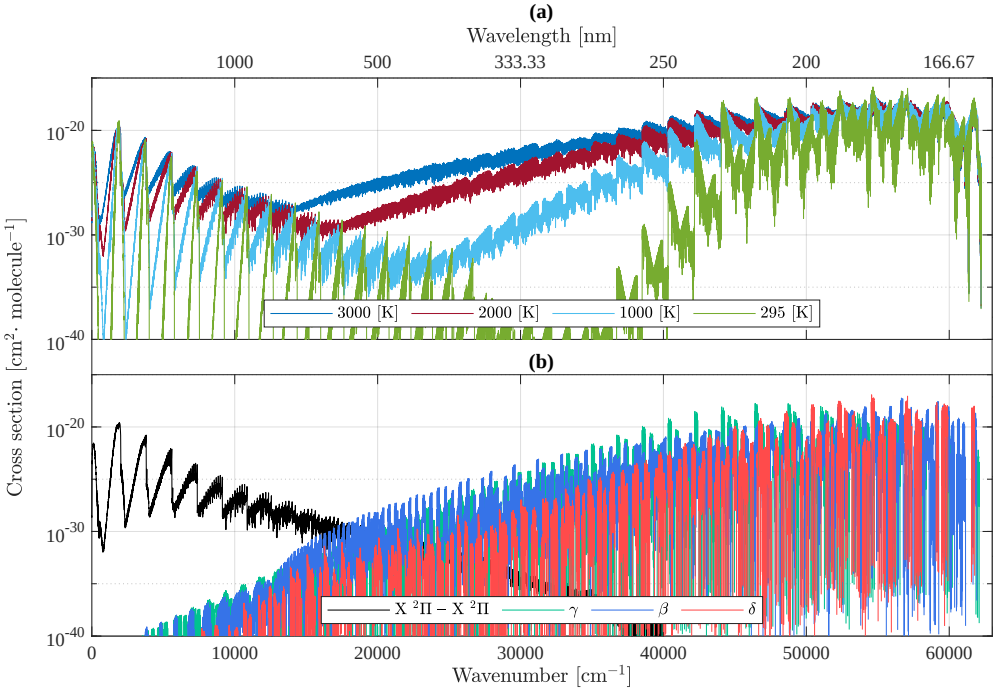

Figure 5.9: $^{14}N^{16}O$ cross sections below 63 000 cm^{-1} calculated using the XABC line list and a Gaussian lineshape function with a HWHM of 1 cm^{-1}: (a) Calculated cross sections of NO at different temperatures; (b) $X\,^2\Pi$– $X\,^2\Pi$, γ, β and δ cross sections at 2000 K.

5.4 Comparisons

Unless otherwise indicated, the following calculations were executed with ExoCross [43], which is a program for generating lifetimes, spectra, partition function etc., from molecular line lists.

5.4.1 Lifetimes

Lifetimes for individual states of $X\,^2\Pi$, $A\,^2\Sigma^+$, $B\,^2\Pi$ and $C\,^2\Pi$ are plotted against the energies in Fig. 5.10. The vibronic lifetimes of$A\,^2\Sigma^+$ ($v = 0$ to 3) and $B\,^2\Pi$ ($v = 0$ to 6) are compared with experimental values (where available) in Tables 5.3 and 5.4, respectively. The calculated lifetimes of the $A\,^2\Sigma^+$ state agree well with those measured by Luque and Crosley [6]. As we used their TDMC, the agreement means that Duo gave similar vibrational wavefunctions as the RKR (Rydberg- Klein-Rees) ones they used. Our computed lifetimes for the $B\,^2\Pi$ state are larger than those of previous works.

The funnel-like shapes of the dependence of lifetimes on the energy shown in Fig. 5.10 (b) are caused by the interactions between the $B\,^2\Pi$ and $C\,^2\Pi$ vibronic levels. The lifetimes decrease to much smaller values when rotational states are trapped in these funnels. Apart from the electronic state interaction, the observed lifetimes are further shortened by predissociation. The dot-dash lines in Fig. 5.10 illustrate the first dissociation limit of NO. As the current version of Duo does not allow for predissociation, the calculated lifetimes to the right of the dot-dash lines are expected to be larger than the observed ones. For example, the calculated lifetimes of $C\,^2\Pi$ are of order 10 ns whereas the measured ones can be as short as several nanoseconds [158].

5.4.2 Absorption spectra

Figure 5.11 compares the experimental absorption intensities of $\gamma(3,0)$ measured by Yoshino *et al.* [7] and theoretical intensities calculated with Duo. With the TDMC of Luque and Crosley [6], our calculations gives higher intensities than the observed ones for the transitions of the $R_{11} + Q_{21}$ and $P_{21} + Q_{11}$ branches. Thus, if we had used the TDMC of Ref. [154], Duo would further amplify the intensities of

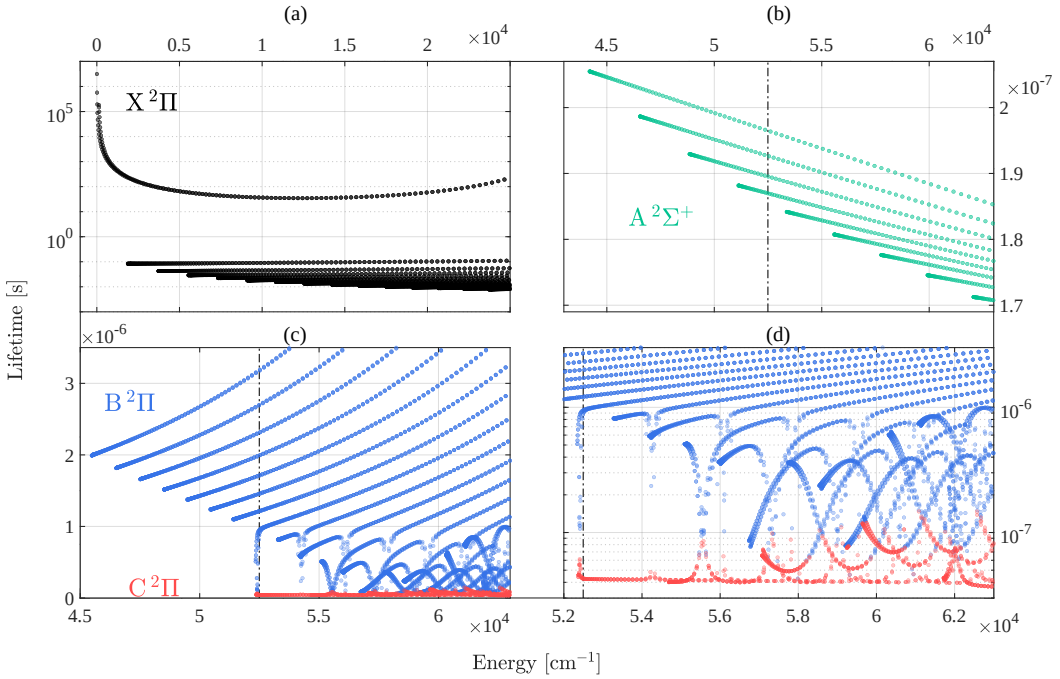

Figure 5.10: Calculated lifetimes of (a) $X^2\Pi$, (b) $A^2\Sigma^+$, and (c)&(d) $B^2\Pi$-$C^2\Pi$ coupled states. The lifetimes of the two lowest states ($X^2\Pi$, $v = 0$, $J = 1/2$, $\Omega = 1/2$, e/f) are respectively infinity and 2.3×10^{14} s^{-1} and are omitted from panel (a). The vertical dot-dash lines in panels (b), (c) and (d) indicate the first dissociation limit of NO. panel (d) is a blow up of panel (c).

Table 5.3: Vibronic radiative lifetimes for the $A^2\Sigma^+$ state.

	Measured [ns]		Calculated [ns]	
v	Ref. [119]	Ref. [154]	Ref. [6]	This work
0	205 ± 7	192.6 ± 0.2	206	205.5
1	200 ± 7	186.2 ± 0.4	199	198.6
2	192 ± 7	179.4 ± 0.7	193	192.9
3	184 ± 7		188	188.1
4	157 ± 10		184	184.1
5	136 ± 10		180	180.8

Table 5.4: Vibronic radiative lifetimes of $B^2\Pi$ state

	Measured [μs]	Calculated [μs]	
v	Ref. [159]	Ref. [118]	This work
0	2.00	2.00	2.00
1	1.82	1.77	1.84
2	1.52	1.56	1.68
3	1.46	1.39	1.53
4	1.19	1.24	1.38
5	1.07	1.11	1.24
6	0.85	0.99	1.11

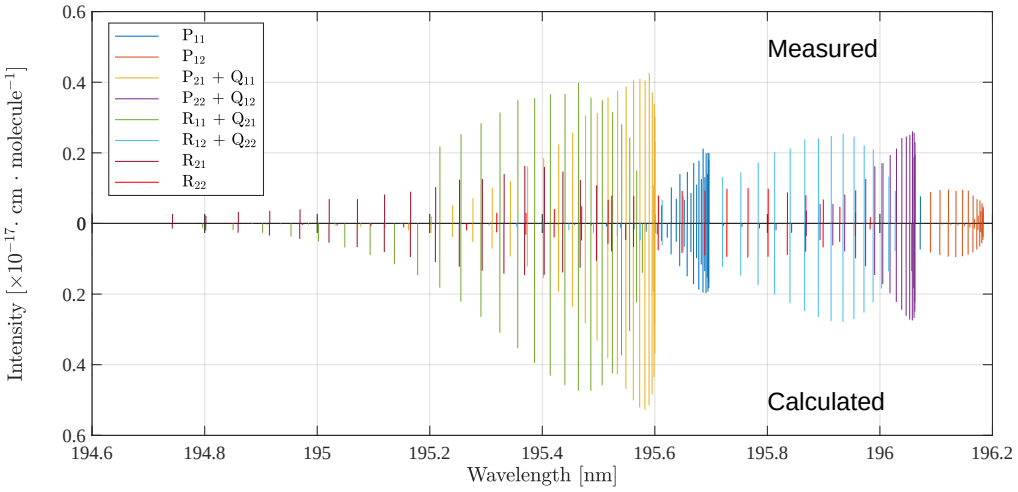

Figure 5.11: Calculated absorption intensities of the NO $\gamma(3,0)$ band at 295 K compared with the published values [7]. As no spin-rotational fine structure was observed in the experiment, the wavelengths of the calculated doublets are averaged and their intensities summed, to also give blended lines.

all branches, worsening agreement with observation.

The $B\,^2\Pi$ - $C\,^2\Pi$ interaction has small effect on the intensities of the lower seven $\beta(v',0)$ bands. Figure 5.12 compares the experimental intensities of $\beta(6,0)$ measured by Yoshino *et al.* [7] and theoretical intensities calculated with Duo. The relative cross section values calculated by LIFBASE [34] are compared with Duo values in Fig. 5.13. The values of LIFBASE are scaled according to the peak of the $\beta(6,0)$ band.

The $\delta(1,0)$ band is the strongest one at 295 K in the $B\,^2\Pi - C\,^2\Pi$ interaction region and the intensities of the transitions in this band are plotted in Fig. 5.14. The figure demonstrates the overall agreement between experimental and theoretical values but also exposes defects in our model showing the interaction model for $B\,^2\Pi - C\,^2\Pi$ is not perfect.

Note that the spectra in Figs. 5.11, 5.12 and 5.14 were calculated using the pure Duo energies before they were replaced by MARVEL or effective Hamiltonian values. However the difference between the experimental and calculated lines is indistinguishable at this scale.

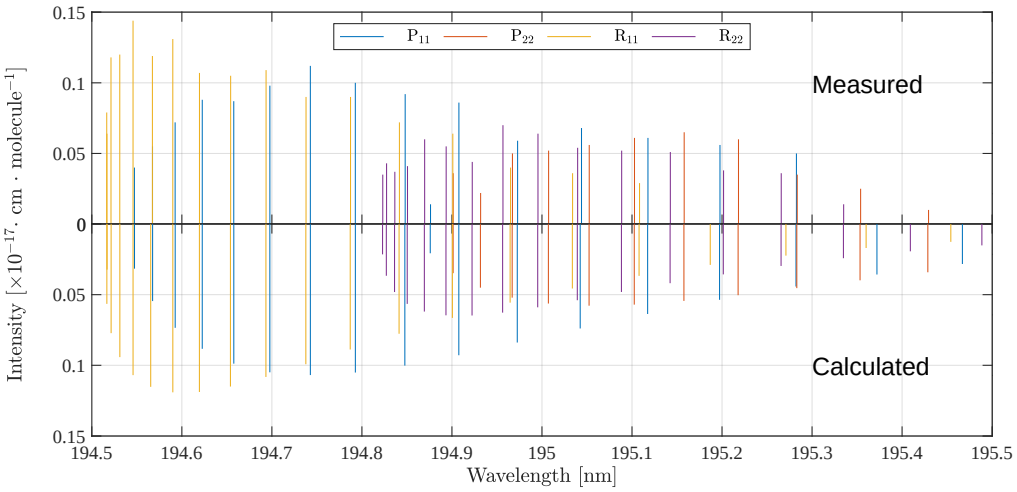

Figure 5.12: Calculated absorption intensities for the $\beta(6,0)$ band at 295 K in comparison with the values given by Yoshino *et al.* [7]. The line intensities of this band are weak and the experiment only resolved the Λ-doublets of high J lines in the P_{11} and R_{11} branches. To achieve higher signal-noise ratio, we averaged the wavelengths of the e and f doublets and added up their intensities to create blended transitions for all branches.

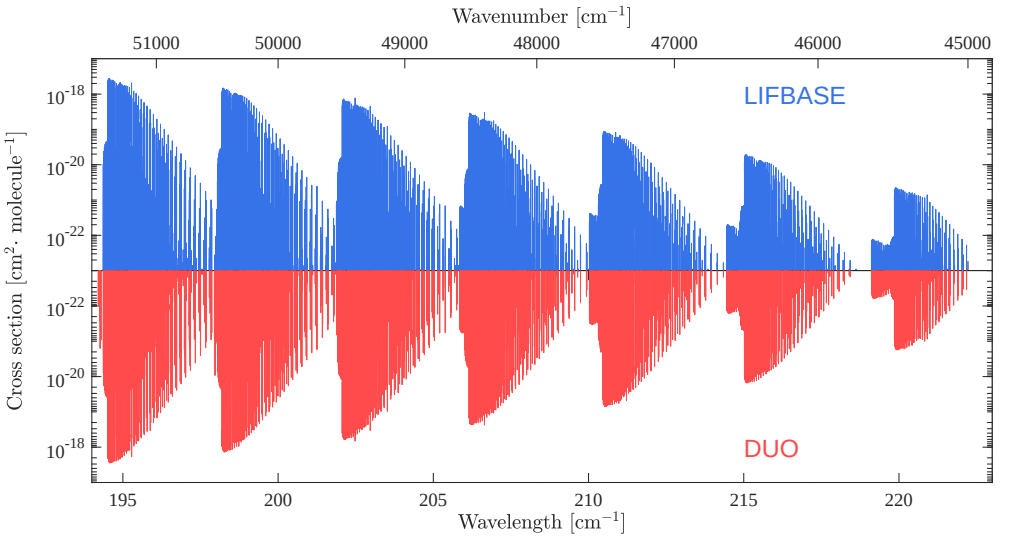

Figure 5.13: Calculated cross section of the NO $\beta(v',0)$ ($v'=6$ to 0 from left to right) bands of at 295 K in comparison with the data from LIFBASE. The spectrum was computed assuming a Gaussian profile with a half-width-at-half-maximum (HWHM) of 0.2 cm. The relative spectrum simulated by LIFBASE is normalised to the peak of the $\beta(6,0)$ band.

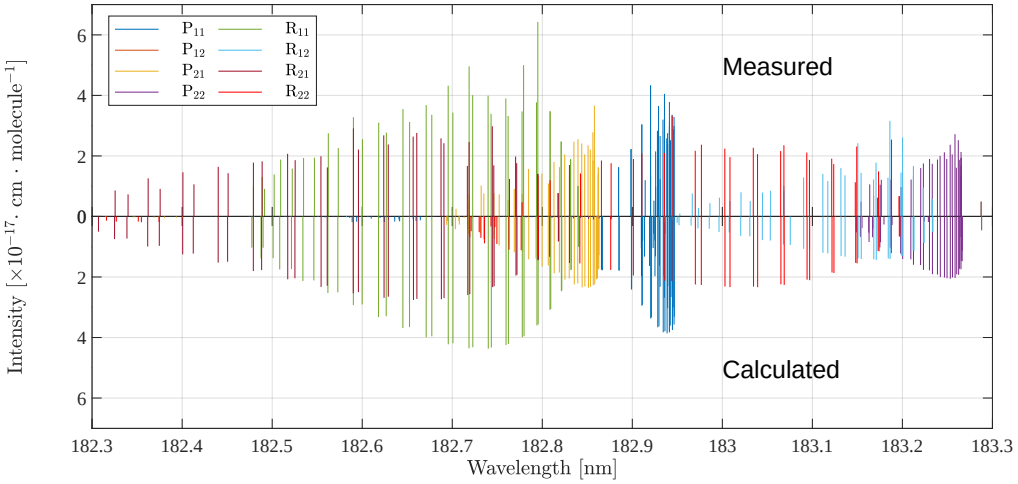

Figure 5.14: Calculated absorption intensities of the δ(1,0) band at 295 K in comparison with the intensities published by Yoshino *et al.* [7]. This is a strong band and most of the Λ-doublets were resolved in the experiment. To allow comparisons of the fine-structure, we evenly divided the measured intensities of any blended lines to created effective e/f transitions.

5.5 Conclusions

In this chapter, we present a new line list for $^{14}N^{16}O$ called XABC which covers transitions between the ground electronic state, $X\,^2\Pi$, and the four lowest-lying states, $X\,^2\Pi$, $A\,^2\Sigma^+$, $B\,^2\Pi$ and $C\,^2\Pi$. The line list combines an effective Hamiltonian (SPFIT), MARVEL and calculated (Duo) energies, providing high-accuracy line positions. Combined with our $A\,^2\Sigma^+$– $X\,^2\Pi$, $B\,^2\Pi$– $X\,^2\Pi$ and $C\,^2\Pi$– $X\,^2\Pi$ transition dipole moments, the diabatic model predicts the transition intensities which agree well with the measured values. The line list is part of ExoMol project [24] and available from (www.exomol.com) and CDS database (cdsarc.u-strasbg.fr).

Chapter 6

A Variational Model for the Hyperfine Resolved Spectrum of VO in its Ground Electronic State

6.1 Introduction

Vanadium monoxide (VO) is an open shell diatomic molecule which absorbs strongly in the near infrared and visible region of the spectrum. These absorptions are of importance for astrophysics where VO is known to be an important component of the atmosphere of cool stars. [160] Recently attention has turned to the possible role of VO in the atmospheres of exoplanets where it has been suggested that alongside TiO, VO absorption can change the temperature profile of the planet's atmosphere.[161] Some tentative detections of VO in exoplanet atmospheres have been reported [162, 163, 164, 165, 166, 167] but none of these can be regarded as secure. There are two reasons for this. First, the spectra of VO and TiO are heavily overlapped making them very hard to disentangle at low resolution. Secondly, while the availability of a high-resolution TiO line list suitable for high-resolution spectroscopic studies [168] has led to the confirmation of TiO in exoplanetary atmospheres, [169, 170, 171] the corresponding VO line list [53] is not of sufficient accuracy to be used in similar studies.[172] Both the TiO and VO line lists cited were produced using similar methodology by the ExoMol project [25] but a major

difference between them is due to the underlying atomic physics. While ^{16}O and ^{40}Ti both have nuclear spin, I, equal zero, the dominant isotope of vanadium, ^{51}V, has $I = 7/2$. The interaction between the spin of unpaired electrons and the nuclear spin, yields a very pronounced hyperfine structure which manifests itself at even moderate resolution. This hyperfine structure reduces parts of the ^{51}V^{16}O spectra to "blurred chaos at Doppler-limited resolution" [173]. Progress in identifying VO in exoplanetary atmospheres using high-resolution spectroscopy requires the development of a model which includes a treatment of these hyperfine effects. These effects were not considered in the ExoMol VOMYT line list.[53]

A full survey of available high resolution spectroscopic data for VO has recently been completed by Bowesman *et al.* [174] as part of a MARVEL (measured active rotation vibration energy levels) study of the system. The nuclear hyperfine structure of ^{51}V^{16}O has been measured [175, 176, 177, 178, 10] and modeled by effective Hamiltonians.[179, 10] However, for the $X\,^4\Sigma^-$ electronic state, the experiments only gave the hyperfine constants for the lowest ($v = 0$) vibrational level and therefore provide limited information for the observations of hot VO spectra involving higher vibrational levels.

Hyperfine structure in molecular spectra are usually treated using perturbation-theory based effective Hamiltonians; these are usually accurate enough to reconstruct the energy levels using the assumption that hyperfine effects arise from small perturbations. Thus, effective Hamiltonians are widely used for fitting measured hyperfine-resolved energies or transitions, see Refs.[179, 10] for examples involving VO. However, the VOMYT line list [53] shows that interactions between the electronic states reshape the line positions and intensities of VO. Although we focus on the $X\,^4\Sigma^-$ electronic ground state of VO in this chapter, the spin-orbit couplings between the low-lying $X\,^4\Sigma^-$ and $1\,^2\Sigma^+$ states as well as the $X\,^4\Sigma^-$ and $A\,^4\Pi$ states are also included in our model with the aim of obtaining the correct spin splittings for the $X\,^4\Sigma^-$ state. This allows us to construct a full, predictive spectroscopic model of the ground state which can be used as input to the variational, diatomic spectroscopic program Duo [42] which we have recently extended to give a full variational

treatment of hyperfine effects.[180] This chapter presents the development of this model.

6.2 Computational details

The electronic structure of VO has been investigated in numerous works. [181, 182, 183, 184, 185, 186, 187, 188, 189, 190, 191] Among them, the results for excited states represented by multi-reference configuration interaction (MRCI) wavefunctions are more accurate. [188, 189, 190, 191] The most recent one by McKemmish *et al.* [190] laid the basis of the ExoMol VO linelist, VOMYT [53]. We also perform MRCI level calculations in this work to get the potential and spin-orbit coupling curves for the electronic states of interest. The electron spin-dipolar interaction and hyperfine coupling curves of $X^4\Sigma^-$ were obtained at the complete active space self consistent field (CASSCF) level.

6.2.1 Quartet states

In this work, the potential energy and spin-orbit coupling curves are calculated using MOLPRO 2015 [124] at the MRCI plus Davidson correction (+Q) level.

First, the ground $X^4\Sigma^-$ state was calculated on its own to avoid effects from other electronic states. The active space used is larger than employed by McKemmish *et al.*, [190] as the work of Miliordos *et al.* [188] shows that the occupation of 4p orbitals of vanadium is not negligible. In this work, the 1s orbital of oxygen and the 1s, 2s, 2p, 3s, 3p orbitals of vanadium were treated as doubly occupied. The active space includes the 2s, 2p orbitals of oxygen and 4s, 3d, 4p orbitals of vanadium. In the four irreducible representations of C_{2v} group, *viz.* a_1, b_1, b_2, a_1, the numbers of occupied orbitals are $(12,5,5,1)$ while the numbers of closed orbitals are $(6,2,2,0)$. The basis set used in our calculation is aug-cc-pVnZ $n = 3,4,5$ [136] so that we can estimate the potential energy curve at the complete basis set (CBS) limit by extrapolation.

According to Miliordos *et al.*,[188] ionic avoided crossings are expected around 2.75 Å. While we came across a discontinuity of dipole moment around 1.9 Å. We tried to add a second $^4\Sigma^-$ state but failed to find an avoided crossing

structure in that region.

The off-diagonal spin-orbit interaction between the $X^4\Sigma^-$ and $A^4\Pi$ states contributes to the spin splitting of the $X^4\Sigma^-$ state. As $A'^4\Phi$ and $A^4\Pi$ has the same irreducible representations in the C_{2v} group, it is impossible to omit the $A'^4\Phi$ state in MRCI calculations. Therefore, we calculated the $A^4\Pi$ and $A'^4\Phi$ states together with the $X^4\Sigma^-$ state using the same active space but only with the aug-cc-pVQZ basis set.

6.2.2 Interaction of doublet states with the $X^4\Sigma^-$ state

Previous studies [190, 53] show that, the spin splitting of the $X^4\Sigma^-$ state of VO is dominated by the off-diagonal spin-orbit interaction between the $X^4\Sigma^-$ and $1^2\Sigma^+$ states.

The $1^2\Sigma^+$ state of VO, designated $a^2\Sigma^+$ in the experimental work of Adam *et al.*,[192] is easily obtained in a CASSCF calculation with MOLPRO when its `LQUANT` is assigned. However, in the MOLPRO MRCI calculation, it may converge to the $1^2\Gamma$ state, which has degenerate A_1 and A_2 representations. The $1^2\Delta$ state also has the same irreducible representations and is lower in energy than the $1^2\Sigma^+$ state. In principle, the three states, $1^2\Sigma^+$, $1^2\Gamma$ and $1^2\Delta$ should be optimized simultaneously in the $^2A_1$ symmetry block. Our calculation therefore included these three low-lying doublet states of VO together with its ground state. The two higher $^2\Pi$ states were also included in the work of McKemmish *et al.* [190] but are not considered here.

We must provide a reasonable CASSCF reference for the MRCI calculations. The $1^2\Sigma^+$ and $1^2\Gamma$ states have the same electron configuration as the $X^4\Sigma^-$ while the $1^2\Delta$ state has a different one.[193] Thus, we initially calculated only the $1^2\Delta$ and ground state, and then subsequently added one $^2\Gamma$ state and one $^2\Sigma^+$ state. Nonetheless, we could not obtain the correct $1^2\Delta$ state in a state-average CASSCF calculation including $^4\Sigma^-$, $^2\Gamma$, $^2\Delta$ and $^2\Sigma^+$ when the closed orbitals were set to $(6,2,2,0)$. To make the reference wavefunctions physically appropriate, we closed more orbitals, $(8,2,2,0)$, in the CASSCF calculation, while we still used the a closed $(6,2,2,0)$ space in the subsequent icMRCI calculation. Again we used an aug-cc-pVQZ basis

set.

6.2.3 Electron spin dipolar coupling and nuclear hyperfine coupling curves

The electron spin-spin coupling was treated as an empirical fine tuning factor by McKemmish *et al.* [53] Using the quantum chemistry program ORCA,[194] we calculated the electron spin-spin dipolar contribution to the zero-field splitting $\boldsymbol{D}$ tensor, of the ground state at the CASSCF level with eleven electrons distributed in ten active orbitals.

Fully-resolved hyperfine splittings have been observed in the $v = 0$ vibrational levels of the $X^4\Sigma^-$ state. We calculated the nuclear hyperfine $\boldsymbol{A}$ tensor and the nuclear electric quadrupole coupling constant in ORCA,[194] with the aim of predicting the hyperfine structure in vibrationally-excited levels of VO.

The zero-field splitting tensor was calculated with an aug-cc-pVTZ basis set. The nuclear magnetic $\boldsymbol{A}$-tensor and electric quadrupole coupling constant were calculated with an aug-cc-pwCVQZ basis set.

The nuclear spin-rotation coupling constants were calculated with another quantum chemistry program, DALTON [87] 2020.0, at the CASSCF level with an aug-cc-pVQZ basis set. The active space is the same as used in ORCA.

We failed to find a quantum chemistry program which calculates the electron spin-rotation constant γ and therefore used the constant empirical value determined for $v = 0$ instead.

6.3 Ab initio results

6.3.1 $X^4\Sigma^-$ potential energy curve

The dashed curves in Fig. 6.1 are the *ab initio* potentials of the $X^4\Sigma^-$ state of VO. We estimated its potential energies at the CBS limit using the formula

$$E(n) = E_{\mathrm{CBS}} + \alpha \exp(-\beta n)$$

and obtained the solid potential energy curve shown in the left panel of Fig. 6.1.

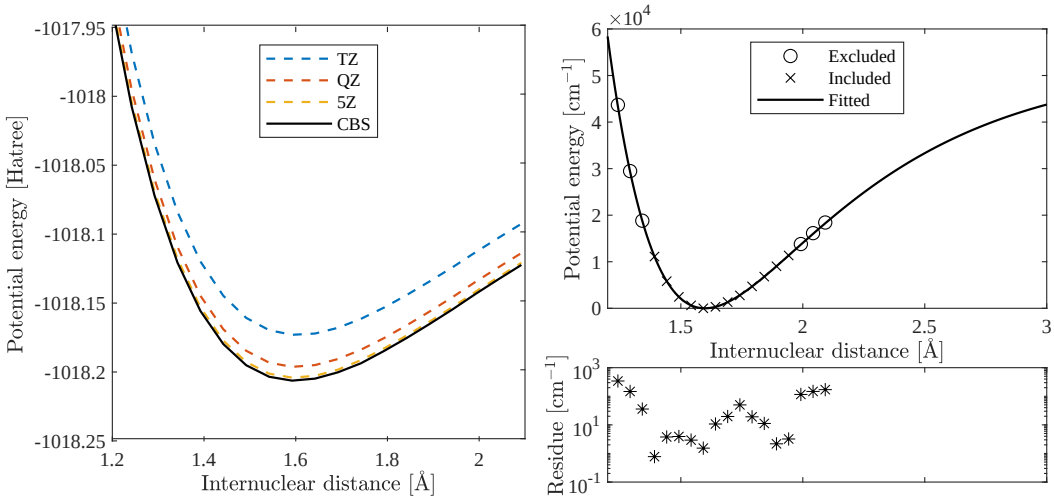

Figure 6.1: MRCI+Q potential energy curves of the $X^4\Sigma^-$ state calculated with aug-cc-pVnZ basis sets and the estimated one at the complete basis set limit.

The *ab initio* curves were calculated to build the spectroscopic model of VO. For numerical stability purposes, we fitted the discrete points with continuous curves. The extrapolated potential energy curve at the CBS limit was fitted to a second-order extended Morse oscillator (EMO) function:[42]

$$V(r) = T_e + (A_e - T_e)\left[1 - \exp\left(-\beta_{EMO}(R)(R - R_e)\right)\right]^2, \tag{6.1}$$

where R and R_e are the internuclear distance and its value at the equilibrium point, and A_e is the asympotic energy relative to the minimum of the ground electronic state. β_{EMO} is expressed as

$$\beta_{EMO}(R) = b_0 + b_1\, y(R) + b_2\, y^2(R), \tag{6.2}$$

where $y(R)$ is given by:

$$y(R) = \frac{R^4 - R_e^4}{R^4 + R_e^4}. \tag{6.3}$$

Only the points given as crosses in the righthand panel of Fig. 6.1 were included in the fit to give a better approximation of the lower vibrational levels. Although the calculated potential energies marked by circles were excluded, they are still well represented by the fitted curve. The EMO parameters are listed in Table 6.1.

Table 6.1: Optimized EMO parameters of the $X\,^4\Sigma^-$ state.

Parameter	$E(n) = E_{\mathrm{CBS}} + \frac{\alpha}{(n+1/2)^4}$	$E'(n) = E_{\mathrm{CBS}} + \alpha e^{-\beta n}$
T_e [cm^{-1}]	0	0
R_e [Å]	1.598 438 63	1.598 355 33
D_e [cm^{-1}]	52790	52790
b_0 [Å^{-1}]	1.837 543 49	1.840 427 24
b_1 [Å^{-1}]	$-9.626\,810\,17 \times 10^{-3}$	$-1.623\,770\,24 \times 10^{-2}$
b_2 [Å^{-1}]	$-1.484\,134\,84 \times 10^{-1}$	$-1.802\,404\,76 \times 10^{-1}$

The fitted PEC is not sensitive to the extrapolation formula in the region of interest (*i.e.* $E \leq 10\,000\,\mathrm{cm}^{-1}$). Figure 6.2 compares the fitted EMO PECs of two extrapolation formulae: $E'(n) = E_{\mathrm{CBS}} + \alpha/n^3$ and $E(n) = E_{\mathrm{CBS}} + \alpha \exp(-\beta n)$. The EMO parameters corresponding to $E'(n)$ are listed in Table 6.1 too.

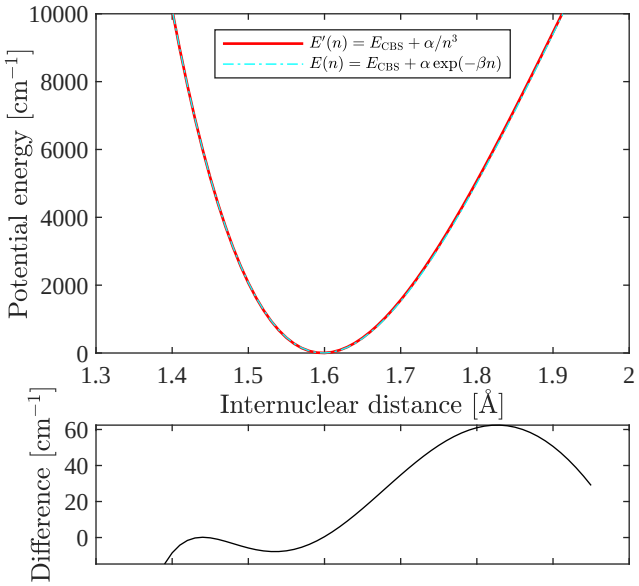

Figure 6.2: Fitted PECs corresponding to two different extrapolation formulae as shown in the legend. The bottom panels show the energy difference between the two curve.

6.3.2 Potentials of $A\,^4\Pi$ and $1\,^2\Sigma^+$

The calculated potential energies curves for the quartet and doublet states are shown in Fig. 6.3. The energies are shifted such that the corresponding $X\,^4\Sigma^-$ ground state of each set has the same energy zero. The potentials of the $A\,^4\Pi$ and $1\,^2\Sigma^+$ states were fitted with second order EMO functions whose parameters are listed in

Table 6.2: Optimized EMO parameters of the excited states.

Parameter	$A\,^4\Pi$	$1\,^2\Sigma^+$
T_e [cm^{-1}]	$9.634\,452\,79\times10^3$	$1.097\,399\,04\times10^4$
R_e [Å]	1.649 119 57	1.593 447 21
D_e [cm^{-1}]	52790	52790
b_0 [Å^{-1}]	1.818 147 51	2.126 803 13
b_1 [Å^{-1}]	$-8.353\,850\,40\times10^{-2}$	$3.162\,274\,70\times10^{-1}$
b_2 [Å^{-1}]	$-3.145\,101\,29\times10^{-1}$	$1.982\,856\,41\times10^{-1}$

Table 6.2.

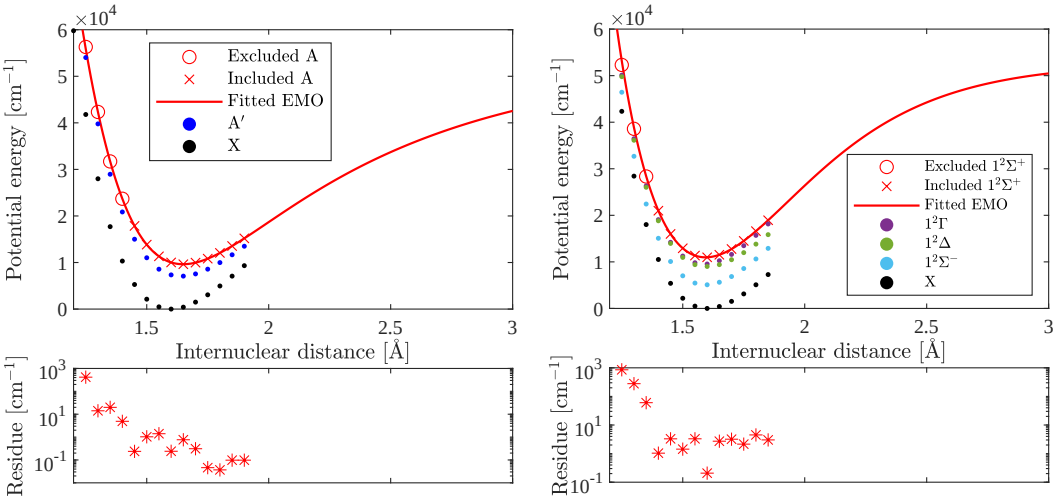

Figure 6.3: Calculated potential energy curves of the quartet states (left) and doublet states (right) of VO. The curves for the $A\,^4\Pi$ and $1\,^2\Sigma^+$ states were fitted with EMO functions.

6.3.3 Spin-orbit couplings

The calculated spin-orbit coupling curves are shown in the left panel of Fig. 6.4. Note that the spin-orbit coupling constant has a phase of i as MOLPRO uses a Cartesian representation. The figure demonstrates the real curves multiplied an extra constant −i, which were fitted with polynomials

$$p(R) = \sum_i a_i R^i. \tag{6.4}$$

The polynomial coefficients a_i are given in Table 6.3.

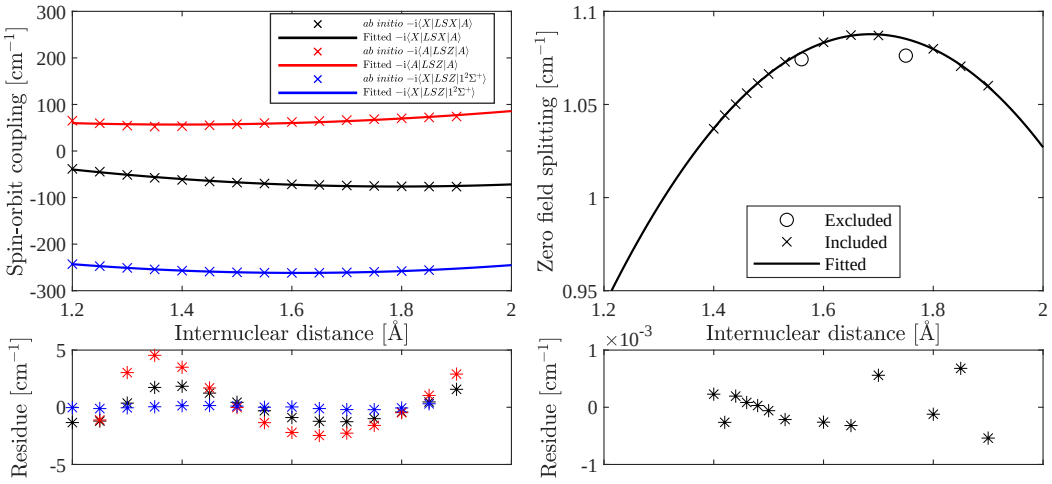

Figure 6.4: The calculated spin-orbit coupling curves (left) and zero field splitting curve due to the spin-spin coupling (right) of VO which were fitted with polynomials.

Table 6.3: Polynomial coefficients of the *ab initio* spin-orbit coupling curves.

Coefficients	$-\mathrm{i}\left\langle \mathrm{X}\,^4\Sigma^- \middle\vert \mathcal{H}_{\mathrm{LSX}} \middle\vert \mathrm{A}\,^4\Pi \right\rangle$	$-\mathrm{i}\left\langle \mathrm{A}\,^4\Pi \middle\vert \mathcal{H}_{\mathrm{LSZ}} \middle\vert \mathrm{A}\,^4\Pi \right\rangle$	$-\mathrm{i}\left\langle \mathrm{X}\,^4\Sigma^- \middle\vert \mathcal{H}_{\mathrm{LSZ}} \middle\vert 1\,^2\Sigma^+ \right\rangle$
a_0 [cm^{-1}]	$1.042\,001\,54\times10^{2}$	$2.116\,610\,61\times10^{1}$	$2.625\,988\,16\times10^{1}$
a_1 [cm^{-1}Å^{-1}]	$-3.735\,161\,08\times10^{2}$	$-2.217\,690\,98\times10^{2}$	$-3.574\,895\,37\times10^{2}$
a_2 [cm^{-1}Å^{-2}]	$2.585\,182\,47\times10^{2}$	$7.943\,250\,83\times10^{1}$	$1.109\,148\,62\times10^{2}$

6.3.4 Electron spin dipolar coupling

In a Cartesian representation, the zero-field splitting Hamiltonian is:[195]

$$\mathcal{H}_{\mathrm{ZFS}} = \boldsymbol{S}^{\mathsf{T}}\boldsymbol{D}\boldsymbol{S}. \tag{6.5}$$

where $\boldsymbol{S} = (S_x, S_y, S_y)$ is the spin vector operator and $\boldsymbol{D}$ is a dipolar interaction tensor. In principal axes of the zero-field splitting tensor, $\boldsymbol{D}$ is diagonal and

$$\mathcal{H}_{\mathrm{ZFS}} = D_{xx}S_x^2 + D_{yy}S_y^2 + D_{zz}S_z^2. \tag{6.6}$$

As a dipolar interaction tensor, $\boldsymbol{D}$ is traceless, $\mathcal{H}_{\mathrm{ZFS}}$ only has two degrees of freedom. In electron spin resonance spectroscopy, it is usual to define two constants, D and E, to describe zero-field splitting:

$$D = \frac{3}{2}D_{zz}, \tag{6.7}$$

Table 6.4: Polynomial coefficients of the *ab initio* zero-field splitting curve $D(R)$ and the empirical spin-rotation curve $\gamma(R)$

Coefficients	$D(R)$	$\gamma(R)$
a_0 [cm^{-1}]	−0.66632402	0.02242111
a_1 [$\mathrm{cm}^{-1}\text{Å}^{-1}$]	2.08037245	
a_2 [$\mathrm{cm}^{-1}\text{Å}^{-2}$]	−0.61684666	

$$E = \frac{1}{2}(D_{xx} - D_{yy}). \tag{6.8}$$

The Hamiltonian can then be rewritten as

$$\mathcal{H}_{\mathrm{ZFS}} = D\left[S_z^2 - \frac{1}{3}\boldsymbol{S}^2\right] + E(S_x^2 - S_y^2), \tag{6.9}$$

with the principal axis chosen such that

$$|E| \leq \frac{1}{3}|D|.$$

For the $\mathrm{X}\,^4\Sigma^-$ state of VO, $E = 0$, and hence $D_{xx} = D_{yy}$.

The calculated zero-field splitting curve is shown in the right panel of Fig. 6.4. The two points marked by circles were excluded from the fit. The other points were fitted with a parabolic curve whose coefficients are given in Table 6.4.

We used the constant experimental value [10] for the spin-rotation coupling curve, as shown in the last column of Table 6.4.

6.3.5 Nuclear hyperfine couplings

In a Cartesian representation, the Hamiltonian describing the nuclear spin – electron spin magnetic interaction is:[195]

$$\mathcal{H}_{\mathrm{HFS}} = \boldsymbol{S}^{\intercal}\boldsymbol{A}\,\boldsymbol{I}. \tag{6.10}$$

The hyperfine coupling tensor can be divided into an isotropic term A^{iso} and a dipolar term $\boldsymbol{A}^{\mathrm{dip}}$:

$$\mathcal{H}_{\mathrm{HFC}} = A^{\mathrm{iso}}\,\boldsymbol{S}\cdot\boldsymbol{I} + \boldsymbol{S}^{\intercal}\boldsymbol{A}^{\mathrm{dip}}\,\boldsymbol{I}. \tag{6.11}$$

A^{iso} is also known as the Fermi-contact interaction constant. The isotropic hyperfine coupling constant is given by

$$A^{\mathrm{iso}} = \frac{1}{3}\left(A_{xx} + A_{yy} + A_{zz}\right). \tag{6.12}$$

The calculated curve A^{iso} is shown in the left panel of Fig. 6.5. The points were fitted with a linear function, whose coefficients are given in Table 6.5.

In the principal axis representation, the off-diagonal matrix elements of the dipolar interaction tensor $\boldsymbol{A}^{\mathrm{dip}}$ vanish. Since $\boldsymbol{A}^{\mathrm{dip}}$ is also traceless, we obtain

$$A_{xx}^{\mathrm{dip}} + A_{yy}^{\mathrm{dip}} + A_{zz}^{\mathrm{dip}} = 0. \tag{6.13}$$

Moreover,

$$A_{xx}^{\mathrm{dip}} = A_{yy}^{\mathrm{dip}}, \tag{6.14}$$

for the $\mathrm{X}\,^4\Sigma^-$ state. Thus, there is only one independent parameter of $\boldsymbol{A}^{\mathrm{dip}}$. The calculated A_{zz}^{dip} term is plotted in the right panel of Fig. 6.5, which was fitted with a parabolic curve whose coefficients are given in Table 6.5.

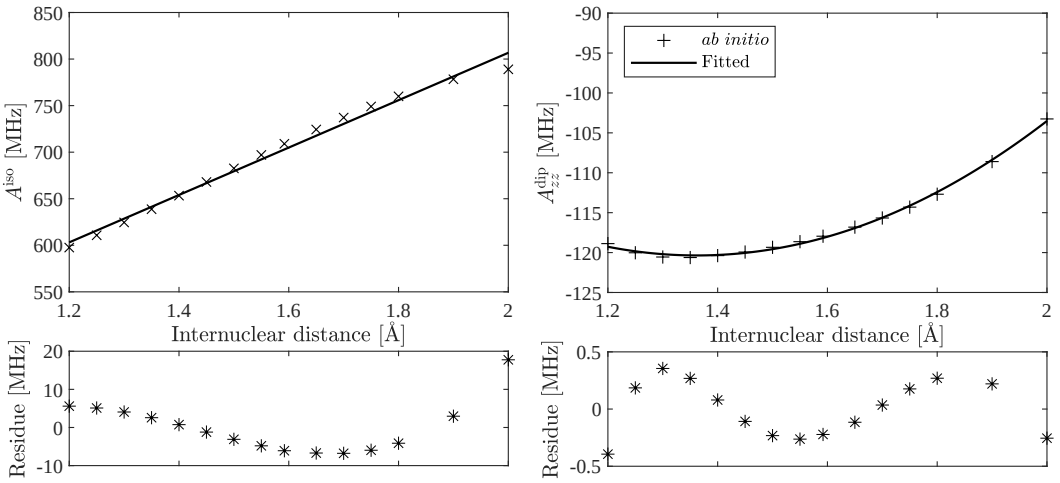

Figure 6.5: The calculated A^{iso} and A_{zz}^{dip} curves of the $\mathrm{X}\,^4\Sigma^-$ state which were fitted with polynomials.

The nuclear electric quadrupole coupling and nuclear spin-rotation coupling are relatively weak for the $\mathrm{X}\,^4\Sigma^-$ state as shown in Fig. 6.6. They were fitted by

Table 6.5: Polynomial coefficients of the *ab initio* hyperfine coupling curves.

Coefficients	A_{zz}^{dip}	A^{iso}
a_0 [MHz]	$-4.353\,746\,34\times10^{1}$	$2.952\,221\,35\times10^{2}$
a_1 [MHz Å^{-1}]	$-1.127\,992\,91\times10^{2}$	$2.566\,354\,89\times10^{2}$
a_2 [MHz Å^{-2}]	$4.140\,638\,43\times10^{1}$	

Table 6.6: Polynomial coefficients of the *ab initio* hyperfine coupling curves.

Coefficients	eQq_0	c_I
a_0 [MHz]	$-3.672\,145\,82\times10^{3}$	$3.773\,228\,18\times10^{4}$
a_1 [MHz Å^{-1}]	$1.003\,490\,24\times10^{4}$	$-1.315\,887\,01\times10^{5}$
a_2 [MHz Å^{-2}]	$-1.091\,669\,36\times10^{4}$	$1.825\,385\,09\times10^{5}$
a_3 [MHz Å^{-3}]	$5.915\,071\,64\times10^{3}$	$-1.262\,342\,03\times10^{5}$
a_3 [MHz Å^{-4}]	$-1.600\,684\,27\times10^{3}$	$4.351\,974\,09\times10^{4}$
a_4 [MHz Å^{-5}]	$1.733\,554\,38\times10^{2}$	$-5.995\,321\,61\times10^{3}$

polynomials, see eq. 6.4, whose coefficients are listed in Table 6.6.

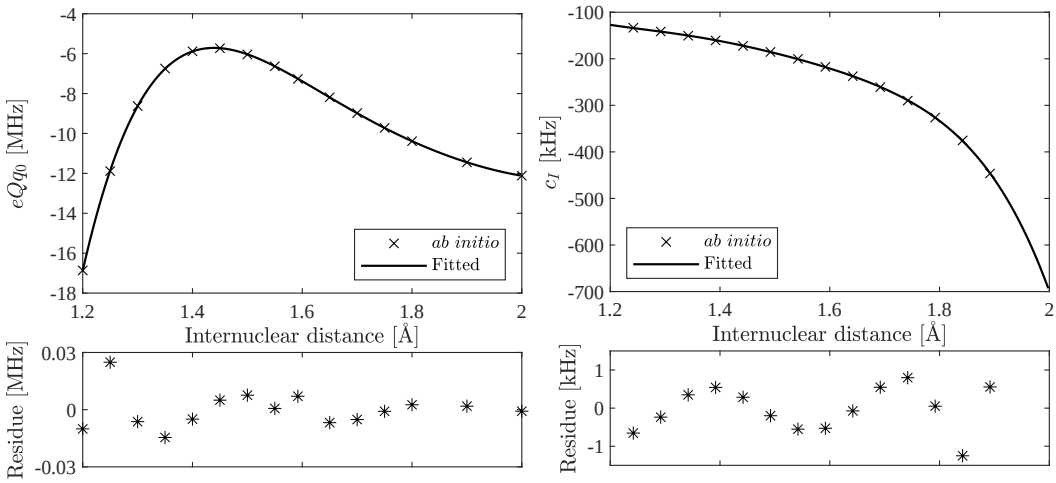

Figure 6.6: The calculated nuclear electric quadrupole and nuclear spin-rotation coupling curves of the $X\,^4\Sigma^-$ state which were fitted with polynomials.

6.4 Infrared spectra

6.4.1 Spectroscopic model

A spectroscopic model considering the $X\,^4\Sigma^-$, $A\,^4\Pi$ and $1\,^2\Sigma^+$ states of VO was developed for the diatomic variational nuclear motion program Duo.[42] The equi-

librium bond length of $X^4\Sigma^-$ *ab initio* PEC was shifted about 0.009 Å so that

$$R_e = 1.58948094 \text{ Å}, \tag{6.15}$$

resulting in the correct rotational constant.

For the basis set in Duo we used 20 vibrationally contracted basis functions for the ground electronic states and 10 for the other two electronic states based on 401 Sinc-DVR grid points, covering the internuclear distance range from 1.2 to 4 Å. The upper limit of the energy calculations was set to $50000\,\text{cm}^{-1}$, which is just below the first dissociation limit of VO; the energy levels of interest for this work are below $10000\,\text{cm}^{-1}$ which is close to the T_e value of the $A^4\Pi$ state and is also below the discontinuity point in the PEC of the $X^4\Sigma^-$ state. This range covers vibrational levels up to $v = 10$. Thus, the 20 vibrational contracted basis functions are enough to give converged energy levels.

The coupling constants used in Duo follow the definitions generally adopted in experimental studies.[180] Some constants have the same definition as those given by quantum chemistry programs. For example, the Fermi-contact coupling constant is just A^{iso}

$$b_{\text{F}} = A^{\text{iso}}. \tag{6.16}$$

Definitions of others are differ and we give the relevant interconversion formulae below.

In a Cartesian representation, the Hamiltonian of the diagonal electron spin-spin dipolar interaction in a diatomic molecule is

$$\mathcal{H}_{\text{SS}} = \frac{2}{3}\lambda\left(3S_z^2 - \boldsymbol{S}^2\right), \tag{6.17}$$

where $\boldsymbol{S}$ is the electron spin angular momentum and S_z is its z component. Comparing $\mathcal{H}_{\text{SS}}$ with $\mathcal{H}_{\text{ZFS}}$, we have

$$\lambda = \frac{1}{2}D. \tag{6.18}$$

In a Cartesian representation, the Hamiltonian of the nuclear spin-electron spin

dipolar interaction is given by

$$\begin{aligned}\mathcal{H}_{\text{dip}} = &\frac{1}{3}c\,(3I_zS_z - \boldsymbol{I}\cdot\boldsymbol{S}) \\ &+ \frac{1}{2}d\left[S_+I_+\exp(-2\mathrm{i}\phi) + S_-I_-\exp(2\mathrm{i}\phi)\right] \\ &e\Big[(S_-I_z + S_zI_-)\exp(\mathrm{i}\phi) \\ &\quad + (S_+I_z + S_zI_+)\exp(-\mathrm{i}\phi)\Big],\end{aligned} \tag{6.19}$$

where c, d and e are three nuclear spin-electron spin dipolar interaction constants; $\boldsymbol{I}$ is the nuclear spin angular momentum; I_z, I_+ and I_- are the components of $\boldsymbol{I}$; S_z, S_+ and S_- are the components of $\boldsymbol{S}$. Comparing the Hamiltonian with the matrix elements of $\boldsymbol{I}^\intercal \boldsymbol{A}^{\text{dip}} \boldsymbol{S}$, we have:

$$A_{xx}^{\text{dip}} = -\frac{c}{3} + d\cos(2\phi), \tag{6.20}$$

$$A_{yy}^{\text{dip}} = -\frac{c}{3} - d\cos(2\phi), \tag{6.21}$$

$$A_{zz}^{\text{dip}} = \frac{2c}{3}. \tag{6.22}$$

For the ground state, we have $A_{xx}^{\text{dip}} = A_{yy}^{\text{dip}}$. The only non-vanishing constant is

$$c = \frac{3}{2}A_{zz}. \tag{6.23}$$

We used the finite-field $\mathrm{X}^4\Sigma^-$ permanent electric dipole moment calculated by McKemmish *et al.* [190] to compute Einstein-A coefficients and hence transition intensities.

6.4.2 Hyperfine matrix elements

We use a fully variational method to calculated the hyperfine structure of the VO $\mathrm{X}^4\Sigma^-$ state. The final wavefunctions have non-zero projections on all contracted vibrational basis functions. The absolute values of the Fermi-contact matrix elements $\langle v|b_{\text{F}}(R)|v'\rangle$ are plotted in Fig. 6.7. The values decrease dramatically with the difference between v' and v, *i.e.*, the diagonal matrix element $\langle v|b_{\text{F}}(R)|v\rangle$ domi-

nates the Fermi-contact interaction in the vibrational states. The reason for the phenomenon is that the lowest 11 vibrational levels of $X^4\Sigma^-$ do not interact with other vibronic levels in our model. Thus, the diagonal Fermi-contact matrix elements in the VO $X^4\Sigma^-$ state provided should be equivalent to the spectroscopic coupling constants used in effective Hamiltonian methods. We list all the diagonal hyperfine matrix elements of the lowest 11 vibrational levels of the $X^4\Sigma^-$ state in Table 6.7. Compared to the measured constants of the $v = 0$ level[10], the absolute values of the calculated Fermi-contact matrix elements are smaller while the nuclear spin-electron spin dipolar matrix elements are larger. For VO, the nuclear spin-rotation and nuclear electric quadrupole interactions are much weaker than the other hyperfine interactions. The corresponding matrix elements are of similar magnitude to the experimental values.

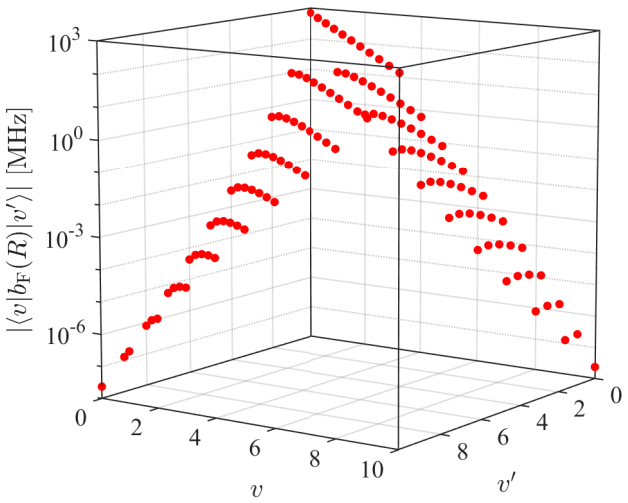

Figure 6.7: Absolute values of Fermi-contact matrix elements $\langle v|b_F(R)|v'\rangle$ of $X^4\Sigma^-$ for $v \leq 10$ and $v' \leq 10$.

6.4.3 Hyperfine eigenstates and transitions

A hyperfine-resolved line list was generated based on the spectroscopic model. Duo provides data in ExoMol format[156] which means energies with quantum numbers in a `.states` file and the Einstein-A coefficients for each transition in a `.trans` file. Examples of calculated energies and transitions extracted from the output files

Table 6.7: The empirical hyperfine coupling constants for $v = 0$ given in Table 4 of Ref. [10] and the calculated diagonal hyperfine matrix elements of $v = 0$ levels of the $X\,^4\Sigma^-$ state. All values are given in MHz.

Empirical [10]	b_F	c	c_I	eQq_0
$v = 0$	778.737(66)	-129.84(19)	0.1928(51)	-2.5(1.3)
Ab initio	$\langle v\|b_F(R)\|v\rangle$	$\langle v\|c(R)\|v\rangle$	$\langle v\|c_I(R)\|v\rangle$	$\langle v\|eQq_0(R)\|v\rangle$
$v = 0$	703.2540	-177.1301	-0.2191	-7.2987

are given in Tables 6.9 and 6.10. In Duo's outputs, the eigenstates are printed in the increasing order of final angular momentum, which is F here. All energies are given relative to the non-hyperfine zero-point energy *i.e.*, the value corresponds to $J = 0.5, +, v = 0$.

A hyperfine-resolved set of empirical energies of VO has recently been obtained [174] using the MARVEL (measured active vibration-rotation energy levels) procedure, which includes 6603 validated transitions from three experimental sources [196, 192, 10] and gives 1256 hyperfine-resolved energy term values for the $v = 0$ state of $X\,^4\Sigma^-$. We compare our calculated energies with all the MARVEL ones, as illustrated in the left panel of Fig. 6.8. The energy differences indicate that the *ab initio* fine and hyperfine coupling curves require further refinement to give accurate electron and nuclear spin splittings.

In order to illustrate the potential of such refinement on the quality of the energy calculations, we shifted some fine and hyperfine coupling curves in our model such that the corresponding diagonal matrix elements $\langle v = 0|\cdot|v = 0\rangle$ have the same values as those determined using experimentally obtained spectroscopic constants [10]. The shifted parameters are listed in Table 6.8. The right panel of Fig. 6.8 demonstrates the differences between the calculated and MARVEL energies in this case. The calculation accuracy improved significantly with use of the shifted curves.

There are four states (shown as red circles in the lefthand panel) whose calculation errors are greater than 0.1 cm^{-1}, so outside the range of the righthand panel of Fig. 6.8. The energy levels between 100 to 200 cm^{-1} have lager uncertainties than the others, as shown in the right panel. As discussed previously,[196, 192, 10] this behavior arises from the internal perturbations near $N = 15$. Figure 6.9 illustrates the

Table 6.8: Final a_0 values for four shifted curves: the $X^4\Sigma^-$-$1^2\Sigma^+$ spin-orbit interaction, $\gamma(R)$, $A^{\rm iso}(R)$ and $A^{\rm dip}_{zz}(R)$.

Curve	State	a_0 value [cm^{-1}]
Spin-orbit	$X^4\Sigma^- - 1^2\Sigma^+$	$5.968\,341\,65\times10^{1}$
$\gamma(R)$	$X^4\Sigma^-$	$2.218\,113\,85\times10^{-2}$
$A^{\rm iso}(R)$	$X^4\Sigma^-$	$1.270\,963\,58\times10^{-2}$
$A^{\rm dip}_{zz}(R)$	$X^4\Sigma^-$	$-4.006\,617\,87\times10^{-4}$

interactions of states in the F_2 series of $X^4\Sigma^-$. The interactions mix energy levels which makes it difficult to assign quantum numbers to these states. The globally J-dependent systematic error can be attributed to inaccurate spin-orbit, spin-spin and spin-rotation coupling curves. We plan to refine these curves in our future work.

Examples of hyperfine resolved transitions (line positions, Einstein A coefficients and line strengths) generated from our model are listed in Table 6.10. The upper and lower states of a transition are labelled with the counting numbers as shown in Table 6.9.

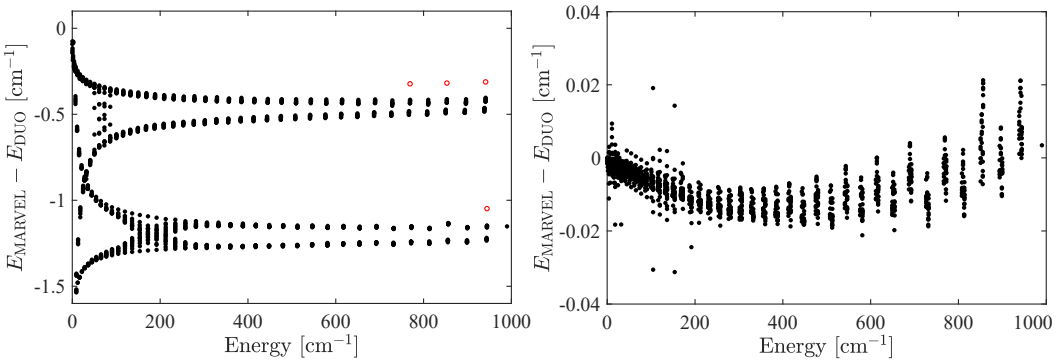

Figure 6.8: Energy differences between results of Duo and MARVEL analysis when using *ab initio* curves. Left: only the R_e value of the $X^4\Sigma^-$ state was shifted to give correct rotational constants. Right: several other curves were also shifted to reproduce the coupling constants given in Table 4 of Ref. [10].

6.4.4 Transition intensities and lifetime

The hyperfine resolved VO line list was used to generate spectra of the $X^4\Sigma^-$ band using the program ExoCross.[43] The left panel of Fig. 6.10 compares cross sections calculated in this work at $T = 2200$ K. We used a Gaussian lineshape function for each isolated line and the linewidth was chosen as 0.2 cm^{-1}. The linewidth is

Table 6.9: Sample of the hyperfine-resolved states extracted from the output file of Duo in the form of an ExoMol states file.

N^1	E^2 [cm^{-1}]	g^3	F^4	I^4	parity	J^4	state	v^4	Λ^4	Σ^4	Ω^4
1	10.66186900	1	0	3.5	+	3.5	X,4Sigma-	0	0	-0.5	-0.5
2	18.18786576	1	0	3.5	+	3.5	X,4Sigma-	0	0	-1.5	-1.5
3	993.75562451	1	0	3.5	+	3.5	X,4Sigma-	1	0	-0.5	-0.5
4	1001.24681027	1	0	3.5	+	3.5	X,4Sigma-	1	0	-1.5	-1.5
5	1966.37762972	1	0	3.5	+	3.5	X,4Sigma-	2	0	-0.5	-0.5
6	1973.83406770	1	0	3.5	+	3.5	X,4Sigma-	2	0	-1.5	-1.5
7	2928.55096185	1	0	3.5	+	3.5	X,4Sigma-	3	0	-0.5	-0.5
8	2935.97211848	1	0	3.5	+	3.5	X,4Sigma-	3	0	-1.5	-1.5
9	3880.31709854	1	0	3.5	+	3.5	X,4Sigma-	4	0	-0.5	-0.5
10	3887.69879342	1	0	3.5	+	3.5	X,4Sigma-	4	0	-1.5	-1.5

[a] Counting number: the calculated energy levels are sorted in the increasing orders of F, parity (+ comes first) and energy term values and then, labeled by the counting number.

[b] Energy term value.

[c] Total degeneracy, $g = 2F + 1$.

[d] F, I, J are the quantum numbers of $\boldsymbol{F}$, $\boldsymbol{I}$, $\boldsymbol{J}$; v indicates the vibrational level; Λ, Σ, Ω are the projections of $\boldsymbol{L}$ (electron orbit angular momentum), $\boldsymbol{S}$ and $\boldsymbol{J}$ on the internuclear axis.

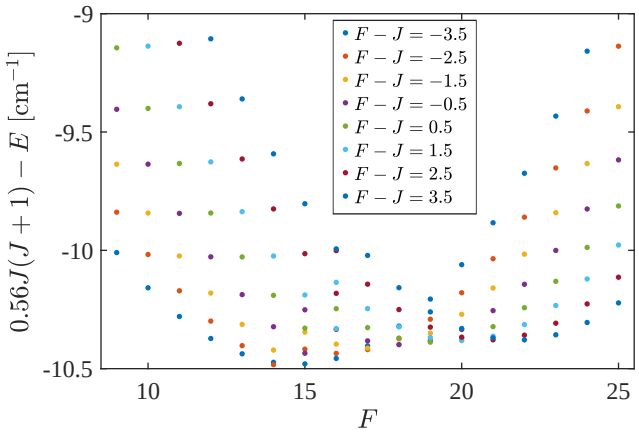

Figure 6.9: Mixing of energy levels in the F_2 series of the X$^4\Sigma^-$ state.

Table 6.10: Sample of the calculated hyperfine-resolved transitions in the form of an ExoMol trans file.

N_{upper}[1]	N_{lower}[2]	A[3] [s^{-1}]	ν[4] [cm^{-1}]
1	451	2.38332335E-05	6.96204647
2	451	1.66833579E-06	14.48804323
3	451	4.70812172E-01	990.05580197
4	451	4.09305033E-03	997.54698774
5	451	2.42692129E-02	1962.67780719
6	451	2.29484807E-04	1970.13424517
7	451	8.52218528E-04	2924.85113931
8	451	8.74951065E-06	2932.27229595
9	451	2.90007987E-05	3876.61727601
10	451	3.10964384E-07	3883.99897089

wider than hyperfine splittings and thus, the cross section profiles are blended. As a result, the hyperfine resolved and unresolved cross sections agree well with each other. Note that, in this work, we only calculated the transitions within the ground state of VO without considering the A-X transition dipole moment contribution to line strengths. In practice, A-X spin-orbit coupling mixes the wavefunctions of the two electronic states meaning spectra are increasingly determined by both the X-X and the A-X electric dipole moment curves; transitions above 6000 cm^{-1} are much stronger when the A-X transition dipole moment is included. We do not attempt to properly model the A state here so we leave the discussion of the interaction of this and other electronic states to future work.

Only hyperfine transitions with narrow broadening parameters are distinguish-

able in high-resolution experiments. We simulated the spectra of the eight hyperfine transitions near 9.73 cm^{-1} with different line widths. As shown in the top-right panel of Fig. 6.10, the hyperfine transitions are completely blended when the half width at half maximum is 0.002 cm^{-1}. However, due to the uneven line strength distribution of hyperfine transitions, the shape and center of the blended profile differs from the one simulated from the line list without considering the nuclear hyperfine couplings, which is shown in the bottom-right panel of Fig. 6.10. Similar conclusions were drawn from the VO MARVEL study [174] where attempts to deperturb the hyperfine-resolved energies by setting the hyperfine constants to zero were found to give poor results.

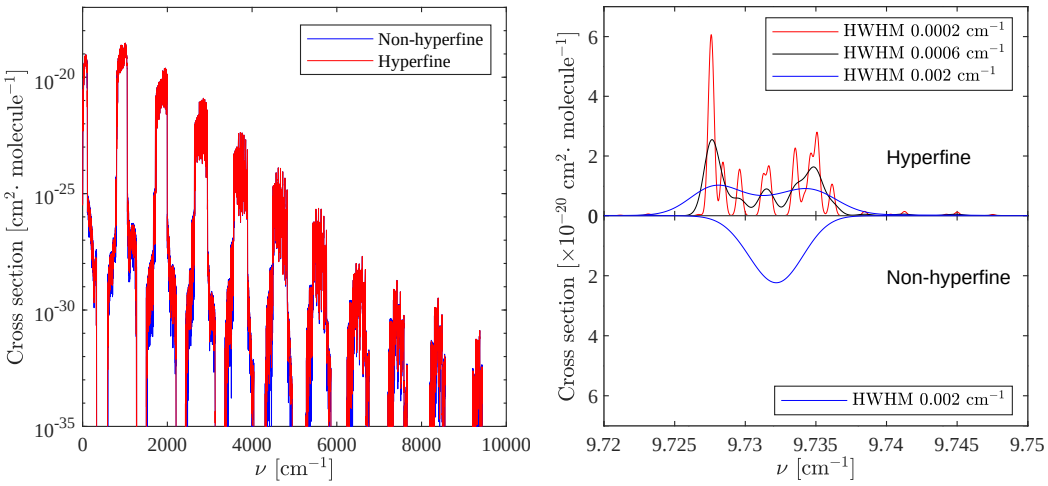

Figure 6.10: Comparison of VO IR cross sections at 2200 K. Left: the cross sections were calculated with Gaussian profiles whose linewidths are 0.2 cm^{-1}. Right: the cross sections were calculated with Gaussian profiles of different line widths in a narrow range. 'Non-hyperfine' in this and following figures is a short notation which means that the spectra were simulated without considering nuclear hyperfine couplings.

Figure 6.11 illustrates the hyperfine splitting of non-hyperfine transitions near 9.77 cm^{-1}. Due to the nuclear spin, both the upper and lower non-hyperfine energy levels split into several hyperfine levels and the combinations of them give a lot of hyperfine transitions as shown in the top panel. In the middle panel, we plot the two strongest non-hyperfine transitions in this region. The intensity of each non-hyperfine transition is approximately the sum of the intensities of the eight strong hyperfine transitions nearby but not rigorously equal to it. These strong hyperfine

transitions were observed [10]. Our calculated positions agree well with the measured values. Note that, the hyperfine transitions are not necessarily distributed around the non-hyperfine transitions, as the transitions near 9.8 cm^{-1} indicate. We emphasize again that in this thesis the word 'non-hyperfine' is used as shorthand notation for the terms given without considering nuclear hyperfine interactions. The word has a different meaning from 'hyperfine unresolved' which is used to describe blended hyperfine transitions.

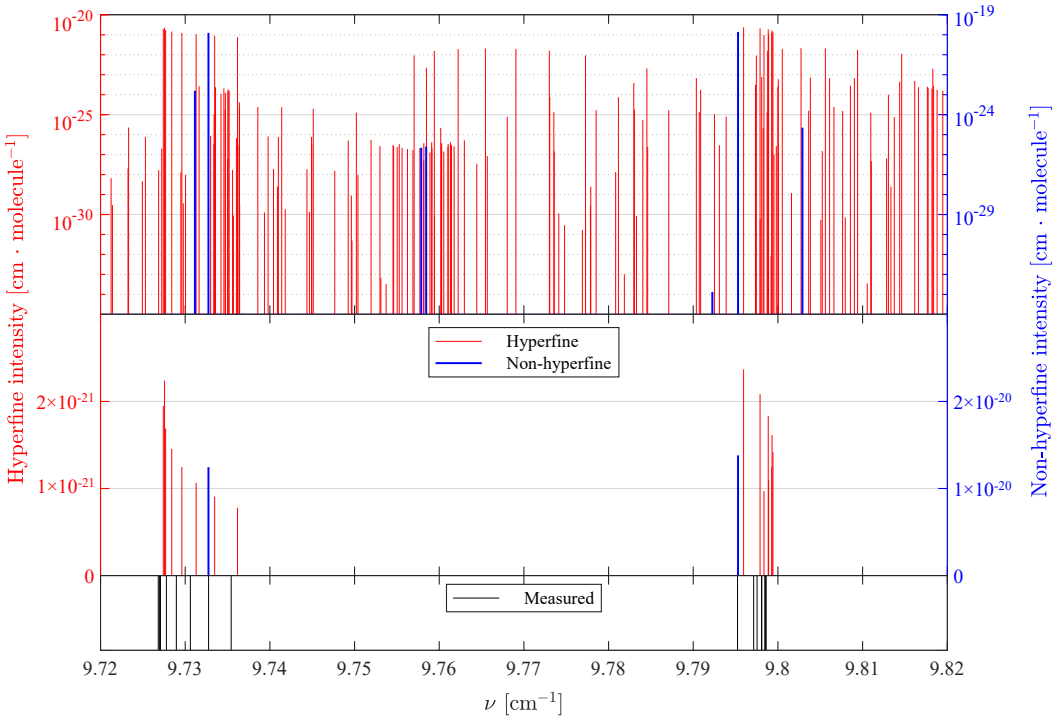

Figure 6.11: Comparison of the calculated (top and middle) and measured (bottom) transitions near 9.77 cm^{-1}. The line intensities in the top and middle panels were calculated at 208 K. The middle panel only shows the strong transitions. The hyperfine resolved line positions in the bottom panel were measured [10].

As the nuclear spin of $^{51}V^{16}O$ is 7/2, theoretically, one can get 'forbidden' dipole transitions up to $|\Delta J| = 8$. Table 6.11 lists eight transitions corresponding to $|\Delta J| = 1, 2, \cdots 8$. As J is no longer a good quantum number for hyperfine structure, the J' and J'' values here are the values of the dominant basis functions. The higher $|\Delta J|$ transitions are much weaker while transitions with $|\Delta J| = 2$ or 3 have Einstein-A coefficients of similar magnitude to the 'allowed' $|\Delta J| = 1$ one. We are not aware of the observation of such forbidden lines within the $X\,^4\Sigma^-$ state. However, $|\Delta J| =$

2 (O and S branches) driven by hyperfine couplings have been observed in both hyperfine-resolved [196, 192] and unresolved [179, 197] rovibronic spectra.

The lifetimes of hyperfine and non-hyperfine eigenstates of the lowest vibrational level of $X^4\Sigma^-$ were calculated by using ExoCross, and compared in Fig. 6.12. The hyperfine states have similar lifetimes as the corresponding non-hyperfine state.

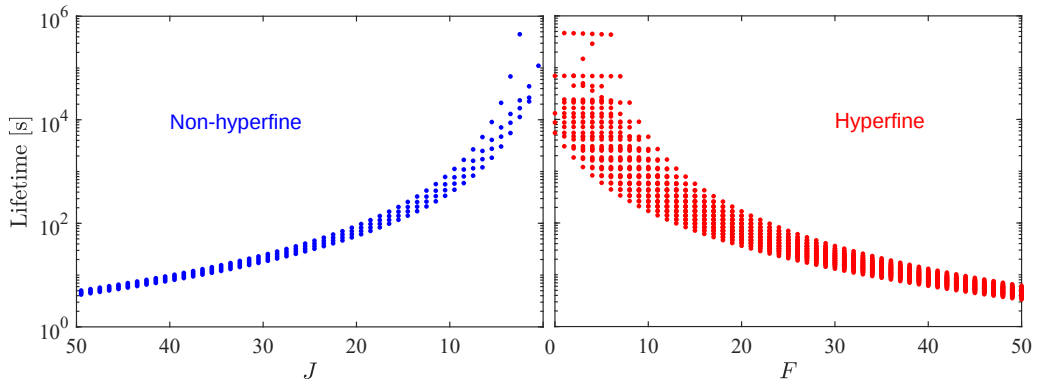

Figure 6.12: Comparison of lifetimes corresponding to the lower rotational levels of $X^4\Sigma^-$, $v = 0$. The $J = 0.5$ levels which have much longer lifetimes were not plotted in this figure.

6.5 Conclusion

In this work, we investigate the hyperfine-resolved infra-red spectra of VO in the $X^4\Sigma^-$ electronic state. The fine and hyperfine coupling curves required to construct the spectroscopic model were calculated *ab initio* where possible but to reproduce the observed hyperfine structure, they were scaled. The hyperfine splitting of the $X^4\Sigma^-$ state is mainly determined by the Fermi-contact and electron spin-nuclear spin dipolar interactions. Nevertheless, we also included the nuclear spin-rotation and nuclear electric quadrupole coupling curves in our calculations. The hyperfine resolved and unresolved cross sections show good consistence with each other when using wide line broadening parameters.

Table 6.11: Transitions corresponding to $|\Delta J| = 1 \cdots 8$.

$\|\Delta J\|$	ν [cm^{-1}]	A [s^{-1}]	E' [cm^{-1}]	F'	parity$'$	J'	v'	Ω'	E'' [cm^{-1}]	F''	parity$''$	J''	v''	Ω''
1	890.2463	6.7981E+01	9370.8835	0	-	3.5	10	0.5	8480.6371	1	+	4.5	9	0.5
2	880.4238	5.6402E+01	8635.9538	14	+	16.5	9	1.5	7755.5299	15	-	18.5	8	1.5
3	921.1696	2.3566E+01	9975.2714	37	-	35.5	10	0.5	9054.1018	36	+	32.5	9	1.5
4	942.0396	2.1003E-01	3909.3168	9	-	6.5	4	0.5	2967.2771	10	+	10.5	3	0.5
5	925.0690	6.9014E-06	9437.0199	11	+	11.5	10	1.5	8511.9509	10	-	6.5	9	0.5
6	923.5723	1.6667E-09	9435.5233	11	+	12.5	10	0.5	8511.9509	10	-	6.5	9	0.5
7	950.5501	1.8763E-15	9462.5010	11	+	13.5	10	1.5	8511.9509	10	-	6.5	9	0.5
8	949.0735	1.6573E-18	9461.0244	11	+	14.5	10	0.5	8511.9509	10	-	6.5	9	0.5

Chapter 7

Summary and Outlook

7.1 Summary of this thesis

The thesis develops methods for the variational calculation of fine and hyperfine resolved rovibronic spectra of diatomic molecules and demonstrates the accuracy and efficiency of these methods in representing complex diatomic systems with two challenging cases, NO and VO.

The variational method for calcualtions of fine structure of diatomic molecules is explained in the Theoretical Background chapter. To keep the consistency of theoretical derivations, an algorithm for the variational calculation of hyperfine structure and spectra of diatomic molecules is immediately discussed in Chapter 3. The algorithm is derived by using irreducible spherical tensors. Hyperfine coupling terms considered in this thesis are the Fermi-contact, nuclear spin-electron spin dipole-dipole, nuclear spin-orbit, nuclear spin-rotation and nuclear electric quadrupole interactions. The algorithm is implemented in Duo and tested with two cases, $^{14}N^{16}O$ and ^{24}MgH. The results are compared to experiment and shown to be consistent with those given in PGOPHER.

A spectroscopic model for the lowest four doublet states of NO, *i.e.*, the $X\,^2\Pi$, $A\,^2\Sigma^+$, $B\,^2\Pi$ and $C\,^2\Pi$ states, is developed in Chapter 4. This model introduces a diabatic coupling between the $B\,^2\Pi$ and $C\,^2\Pi$ states to describe the avoided crossing structure of B-C coupled states. A spectroscopic network is built containing more than 20000 transitions of NO. Energies levels are reconstructed from the network

by MARVEL analysis. The potential and coupling curves are refined such that the model can reproduce eigenvalues that are consistent with the empirical energy levels.

Based on the model, an accurate line list, called XABC, has been computed in Chapter 5, which covers the pure rotational, vibrational and rovibronic spectra of $^{14}N^{16}O$. A mixture of empirical and theoretical electronic transition dipole moments are used for the calculation of transition intensities. The diabatic coupling scheme is adopted in the spectroscopic model to successfully predict the line positions and intensities for the transitions in the B-C interaction region, which agree well with the experimental values.

In Chapter 6, hyperfine resolved infra-red spectra of VO have been calculated using a variational model, which aims to accurately predict the hyperfine structure within the VO $X^4\Sigma^-$ electronic state. *Ab initio* calculated nuclear hyperfine coupling curves, including the Fermi-contact interaction, electron spin-nuclear spin dipolar interaction, nuclear spin-rotation interaction and nuclear electric quadrupole interaction, are considered. The calculated hyperfine-resolved cross sections show good agreement with the hyperfine unresolved cross sections when using appropriate lineshape broadening parameters. This and other comparisons validate both our model and the implemented hyperfine modules in Duo.

7.2 Future work

7.2.1 Modules for hyperfine structure

Our current implementation of hyperfine modules in Duo only allows for nuclear spin effects in one atom and neglects coupling between electronic states. The hyperfine coupling between two electronic states is known to be important for some molecules. For instance, to analyse the spectrum of $I^{35}Cl$, Slotterback *et al.* also included the hyperfine coupling terms between the $X\,^1\Sigma^+$ and $A\,^3\Pi$ states [198]. Implementing this effect in Duo would require some further work on the matrix elements but should not be a major undertaking. Treating the case where both atoms possess a nuclear spin introduces another source of angular momentum and

the interaction between the two nuclei also introduces new matrix elements [71]. Here there are two possibilities, homonuclear systems, such as $^{1}H_2$ or $^{14}N_2$, can be treated by generalizing the scheme given in this thesis. Heteronuclear systems, such as $^{1}H^{14}N$, are a little more complicated as they give rise to different possible coupling schemes [72]. Our plan is to gradually update Duo for each of these cases as the need arises.

7.2.2 Line list of NO

The XABC line list covers the transitions of three main band systems of NO in the ultraviolet spectral region, *i.e.* the γ, β and δ systems, connecting its lowest four electronic states. However, experiments show that there are also strong absorption lines between the $D^2\Sigma^+$ and $X^2\Pi$ states of NO, *i.e.*, within the ϵ band system. Emissions between excited states of NO have also been observed. A more comprehensive line list can be further generated after a detail MARVEL analysis and *ab initio* calculations.

7.2.3 Line list of VO

The MARVEL analysis of the VO molecule by Bowesman *et al.* [174] included 15 electronic states . An update model for VO can be developed based on this work and further quantum chemistry investigations. The potential energy curves and coupling curves of the 13 electronic states in the model of McKemmish *et al.* [190] can be further refined. The model is expected to give a more accurate line list compared with VOMYT [53]

Bibliography

[1] Francis A. Jenkins, Henry A. Barton, and Robert S. Mulliken. The β Bands of Nitric Oxide. I. Measurements and Quantum Analysis. *Phys. Rev.*, 30:150–174, 1927.

[2] C. Amiot. The infrared-emission spectrum of NO: Analysis of the $\Delta v = 3$ sequence up to $v = 22$. *J. Mol. Spectrosc.*, 94:150–172, 1982.

[3] D. C. Cartwright, M. J. Brunger, L. Campbell, B. Mojarrabi, and P. J. O. Teubner. Nitric oxide excited under auroral conditions: Excited state densities and band emissions. *J. Geophys. Res.*, 105:20857–20867, 2000.

[4] H. Shi and A. L. L. East. Improved results for the excited states of nitric oxide, including the B/C avoided crossing. *J. Chem. Phys.*, 125:7, 2006.

[5] O. N. Sulakshina and Yu. G. Borkov. Critical evaluation of measured line positions of $^{14}N^{16}O$ in $X^2\Pi$ state. *J. Quant. Spectrosc. Radiat. Transf.*, 209:171–179, 2018.

[6] J. Luque and D. R. Crosley. Transition probabilities and electronic transition moments of the $A^2\Sigma^+$ - $X^2\Pi$ and $D^2\Sigma^+$ - $X^2\Pi$ systems of nitric oxide. *J. Chem. Phys.*, 111:7405–7415, 1999.

[7] K. Yoshino, A. P. Thorne, J. E. Murray, A. S.-C. Cheung, A. L. Wong, and T. Imajo. The application of a vacuum-ultraviolet fourier transform spectrometer and synchrotron-radiation source to measurements of bands of no. vii. the final report. *J. Chem. Phys.*, 124:054323, 2006.

[8] R. J. Hargreaves, I. E. Gordon, L. S. Rothman, S. A. Tashkun, V. I. Perevalov, A. A. Lukashevskaya, S. N. Yurchenko, J. Tennyson, and H. S. P. Müller. Spectroscopic line parameters of NO, NO_2, and N_2O for the HITEMP database. *J. Quant. Spectrosc. Radiat. Transf.*, 232:35 – 53, 2019.

[9] R. R. Gamache, C. Roller, E. Lopes, I. E. Gordon, L. S. Rothman, O. L. Polyansky, N. F. Zobov, A. A. Kyuberis, J. Tennyson, S N Yurchenko, A. G. Császár, T. Furtenbacher, Xinchuan Huang, David W. Schwenke, Timothy J. Lee, B J Drouin, S. A. Tashkun, V. I. Perevalov, and R V. Kochanov. Total Internal Partition Sums for 167 isotopologues of 53 molecules important in planetary atmospheres: application to HITRAN2016 and beyond. *J. Quant. Spectrosc. Radiat. Transf.*, 203:70–87, 2017.

[10] M. A. Flory and L. M. Ziurys. Submillimeter-wave spectroscopy of VN ($X^3\Delta_r$) and VO ($X^4\Sigma^-$): A study of the hyperfine interactions. *J. Mol. Spectrosc.*, 247:76–84, 2008.

[11] L M Ziurys, W L Barclay, and M A Anderson. The millimeter-wave spectrum of the MgH and MgD radicals. *Astrophys. J.*, 402:L21–L24, 1993.

[12] J.-C. Gérard, C. Cox, A. Saglam, J.-L. Bertaux, E. Villard, and C. Nehmé. Limb observations of the ultraviolet nitric oxide nightglow with SPICAV on board Venus Express. *J. Geophys. Res.*, 113:E00B03, 2008.

[13] J.-C. Gérard, C. Cox, L. Soret, A. Saglam, G. Piccioni, J.-L. Bertaux, and P. Drossart. Concurrent observations of the ultraviolet nitric oxide and infrared O_2 nightglow emissions with Venus Express. *J. Geophys. Res.*, 114:E00B44, 2009.

[14] Jonathan Tennyson. *Astronomical spectroscopy : an introduction to the atomic and molecular physics of astronomical spectra*. World Scientific, Singapore, 3 edition, 2019.

[15] J. Lelieveld, K. Klingmüller, A. Pozzer, R. T. Burnett, A. Haines, and V. Ramanathan. Effects of fossil fuel and total anthropogenic emission removal on

public health and climate. *Proc. Natl. Acad. Sci. U. S. A.*, 116:7192–7197, 2019.

[16] Matti Barthel, Marijn Bauters, Simon Baumgartner, Travis W. Drake, Nivens Mokwele Bey, Glenn Bush, Pascal Boeckx, Clement Ikene Botefa, Nathanaël Dériaz, Gode Lompoko Ekamba, Nora Gallarotti, Faustin M. Mbayu, John Kalume Mugula, Isaac Ahanamungu Makelele, Christian Ekamba Mbongo, Joachim Mohn, Joseph Zambo Mandea, Davin Mata Mpambi, Landry Cizungu Ntaboba, Montfort Bagalwa Rukeza, Robert G. M. Spencer, Laura Summerauer, Bernard Vanlauwe, Kristof Van Oost, Benjamin Wolf and Johan Six. Low N_2O and variable CH_4 fluxes from tropical forest soils of the congo basin. *Nat. Commun.*, 13:1–8, 2022.

[17] Jan Laufer, Clare Elwell, Dave Delpy, and Paul Beard. In vitro measurements of absolute blood oxygen saturation using pulsed near-infrared photoacoustic spectroscopy: accuracy and resolution. *Phys. Med. Biol.*, 50:4409, 2005.

[18] Ronald K. Hanson, R. Mitchell Spearrin, and Christopher S. Goldenstein. *Spectroscopy and Optical Diagnostics for Gases*. Springer International Publishing, 2016.

[19] Ignas Snellen. High-dispersion spectroscopy of extrasolar planets: from CO in hot jupiters to O_2 in exo-earths. *Phil. Trans. R. Soc. Lond. A*, 372:20130075, 2014.

[20] J. Tennyson and S. N. Yurchenko. Molecular line lists for studies exoplanet and other hot atmospheres. *Frontiers Astron. Space Sci.*, 8:218, 2022.

[21] I. E. Gordon, L. S. Rothman, R. J. Hargreaves, R. Hashemi, E. V. Karlovets, F. M. Skinner, E. K. Conway, C. Hill, R. V. Kochanov, Y. Tan, P. Wcisło, A. A. Finenko, K. Nelson, P. F. Bernath, M. Birk, V. Boudon, A. Campargue, K. V. Chance, A. Coustenis, B. J. Drouin, J.–M. Flaud, R. R. Gamache, J. T. Hodges, D. Jacquemart, E. J. Mlawer, A. V. Nikitin, V. I. Perevalov, M. Rotger, J. Tennyson, G. C. Toon, H. Tran, V. G. Tyuterev, E. M. Adkins,

A. Baker, A. Barbe, E. Canè, A. G. Császár, A. Dudaryonok, O. Egorov, A. J. Fleisher, H. Fleurbaey, A. Foltynowicz, T. Furtenbacher, J. J. Harrison, J.–M. Hartmann, V.–M. Horneman, X. Huang, T. Karman, J. Karns, S. Kassi, I. Kleiner, V. Kofman, F. Kwabia–Tchana, N. N. Lavrentieva, T. J. Lee, D. A. Long, A. A. Lukashevskaya, O. M. Lyulin, V. Yu. Makhnev, W. Matt, S. T. Massie, M. Melosso, S. N. Mikhailenko, D. Mondelain, H. S. P. Müller, O. V. Naumenko, A. Perrin, O. L. Polyansky, E. Raddaoui, P. L. Raston, Z. D. Reed, M. Rey, C. Richard, R. Tóbiás, I. Sadiek, D. W. Schwenke, E. Starikova, K. Sung, F. Tamassia, S. A. Tashkun, J. Vander Auwera, I. A. Vasilenko, A. A. Vigasin, G. L. Villanueva, B. Vispoel, G. Wagner, A. Yachmenev, and S. N. Yurchenko. The HITRAN2020 molecular spectroscopic database. *J. Quant. Spectrosc. Radiat. Transf.*, 277:107949, 2022.

[22] S. N. Yurchenko, J. Tennyson, Jeremy Bailey, Morgan D J Hollis, and Giovanna Tinetti. Spectrum of hot methane in astronomical objects using a comprehensive computed line list. *Proc. Nat. Acad. Sci.*, 111:9379–9383, 2014.

[23] L. S. Rothman, I. E. Gordon, R. J. Barber, H. Dothe, R. R. Gamache, A. Goldman, V. I. Perevalov, S. A. Tashkun, and J. Tennyson. HITEMP, the High-Temperature Molecular Spectroscopic Database. *J. Quant. Spectrosc. Radiat. Transf.*, 111:2139–2150, 2010.

[24] J. Tennyson and S. N. Yurchenko. ExoMol: molecular line lists for exoplanet and other atmospheres. *Mon. Not. Roy. Astron. Soc.*, 425:21–33, 2012.

[25] J Tennyson, S N Yurchenko, A. F. Al-Refaie, V. H. J. Clark, K. L. Chubb, E. K. Conway, A. Dewan, M. N. Gorman, C. Hill, A. E. Lynas-Gray, T. Mellor, L. K. McKemmish, A. Owens, O. L. Polyansky, M. Semenov, W. Somogyi, G. Tinetti, A. Upadhyay, I. Waldmann, Y. Wang, S. Wright, and O. P. Yurchenko. The 2020 release of the ExoMol database: molecular line lists for exoplanet and other hot atmospheres. *J. Quant. Spectrosc. Radiat. Transf.*, 255:107228, 2020.

[26] N. Jacquinet-Husson, R. Armante, N. A. Scott, A. Chédin, L. Crépeau, C. Boutammine, A. Bouhdaoui, C. Crevoisier, V. Capelle, C. Boonne, N. Poulet-Crovisier, A. Barbe, D. Chris Benner, V. Boudon, L. R. Brown, J. Buldyreva, A. Campargue, L. H. Coudert, V. M. Devi, M. J. Down, B. J. Drouin, A. Fayt, C. Fittschen, J.-M Flaud, R. R. Gamache, J. J. Harrison, C. Hill, Ø. Hodnebrog, S. M Hu, D. Jacquemart, A. Jolly, E. Jiménez, N. N. Lavrentieva, A. W. Liu, L. Lodi, O. M. Lyulin, S. T. Massie, S. Mikhailenko, H. S. P. Müller, O. V. Naumenko, A. Nikitin, C. J. Nielsen, J. Orphal, V. I Perevalov, A. Perrin, E. Polovtseva, A. Predoi-Cross, M. Rotger, A. A. Ruth, S. S Yu, K. Sung, S. A. Tashkun, J. Tennyson, Vl. G. Tyuterev, J. Vander Auwera, B. A. Voronin, and A. Makie. The 2015 edition of the GEISA spectroscopic database. *J. Mol. Spectrosc.*, 327:31–72, 2016.

[27] Michaël Rey, Andrei V. Nikitin, Yurii L. Babikov, and Vladimir G. Tyuterev. TheoReTS – An information system for theoretical spectra based on variational predictions from molecular potential energy and dipole moment surfaces. *J. Mol. Spectrosc.*, 327:138–158, 2016.

[28] Robert L. Kurucz. Including all the lines 1 This article is part of a Special Issue on the 10th International Colloquium on Atomic Spectra and Oscillator Strengths for Astrophysical and Laboratory Plasmas. *Can. J. Phys.*, 89:417–428, 2011.

[29] Peter F. Bernath. MoLLIST: Molecular Line Lists, Intensities and Spectra. *J. Quant. Spectrosc. Radiat. Transf.*, 240:106687, 2020.

[30] Yixin Wang, J Tennyson, and S N Yurchenko. Empirical line lists in the ExoMol database. *Atoms*, 8:7, 2020.

[31] H M Pickett, R L Poynter, E A Cohen, M L Delitsky, J C Pearson, and H S P Müller. Submillimeter, millimeter, and microwave spectral line catalog. *J. Quant. Spectrosc. Radiat. Transf.*, 60:883–890, 1998.

[32] C. P. Endres, S. Schlemmer, P. Schilke, J. Stutzki, and H. S. P. Müller. The Cologne Database for Molecular Spectroscopy, CDMS, in the Virtual Atomic and Molecular Data Centre, VAMDC. *J. Mol. Spectrosc.*, 327:95–104, 2016.

[33] Xinchuan Huang, David W Schwenke, and Timothy J Lee. Quantitative validation of ames ir intensity and new line lists for $^{32/33/34}S^{16}O_2$, $^{32}S^{18}O_2$ and $^{16}O^{32}S^{18}O$. *J. Quant. Spectrosc. Radiat. Transf.*, 225:327–336, 2019.

[34] Jorge Luque and David R Crosley. Lifbase: Database and spectral simulation program (version 1.5). *SRI international report MP*, 99(009), 1999.

[35] John M. Brown and Alan Carrington. *Rotational Spectroscopy of Diatomic Molecules*. Cambridge University Press, 2003.

[36] Colin M. Western. PGOPHER: A program for simulating rotational, vibrational and electronic spectra . *J. Quant. Spectrosc. Radiat. Transf.*, 186:221–242, 2017.

[37] H. M. Pickett. The fitting and prediction of vibration-rotation spectra with spin interactions. *J. Mol. Spectrosc.*, 148:371–377, 1991.

[38] Misato Haze, Hiroyuki Nakata, Kento Inoue, Ryo Shinohara, Peerapat Wangchingchai, Keigo Nagamori, Yuuki Onitsuka, Katsuyoshi Yamasaki, and Hiroshi Kohguchi. Improvement and determination of higher-order centrifugal distortion constants of the $A^2\Sigma^+$-$X^2\Pi$ electronic transition of NO. *J. Mol. Spectrosc.*, 378:111475, 2021.

[39] Sebastian Sinnecker and Frank Neese. Spin- spin contributions to the zero-field splitting tensor in organic triplets, carbenes and biradicals a density functional and ab initio study. *J. Phys. Chem. A*, 110:12267–12275, 2006.

[40] Natalie Gilka, Peter R Taylor, and Christel M Marian. Electron spin-spin coupling from multireference configuration interaction wave functions. *J. Chem. Phys.*, 129:044102, 2008.

[41] Shanshan Yu, Brian J Drouin, and Charles E Miller. High resolution spectral analysis of oxygen. iv. energy levels, partition sums, band constants, RKR potentials, franck-condon factors involving the $x^3\sigma_g^-$, $a^1\delta_g$ and $b^1\sigma_g^+$ states. *J. Chem. Phys.*, 141:174302, 2014.

[42] S. N. Yurchenko, L. Lodi, J. Tennyson, and A. V. Stolyarov. Duo: a general program for calculating spectra of diatomic molecules. *Comput. Phys. Commun.*, 202:262–275, 2016.

[43] Sergei N. Yurchenko, Ahmed F. Al-Refaie, and Jonathan Tennyson. ExoCross: A general program for generating spectra from molecular line lists. *Astron. Astrophys.*, 614:A131, 2018.

[44] Attila Szabo and Neil S Ostlund. *Modern quantum chemistry: introduction to advanced electronic structure theory*. Dover Publications Inc, 1996.

[45] Ira N Levine. *Quantum chemistry: 7th edition*. Pearson, 2013.

[46] Ralph H Young. New proof of the minimum principle for excited states. *Int. J. Quantum Chem.*, 6:596–597, 1972.

[47] A. R. Edmonds. *Angular Momentum in Quantum Mechanics*. Princeton University Press, 1957.

[48] Jonathan Tennyson, Lorenzo Lodi, Laura K McKemmish, and Sergei N Yurchenko. The ab initio calculation of spectra of open shell diatomic molecules. *J. Phys. B-At. Mol. Opt. Phys.*, 49:102001, 2016.

[49] J. Tennyson and S. N. Yurchenko. The ExoMol project: Software for computing molecular line lists. *Int. J. Quantum Chem.*, 117:92–103, 2017.

[50] R. J. Le Roy. Level: A computer program for solving the radial Schrödinger equation for bound and quasibound levels. *J. Quant. Spectrosc. Radiat. Transf.*, 186:167 – 178, 2017.

[51] A. T. Patrascu, J. Tennyson, and S. N. Yurchenko. ExoMol molecular linelists - IX: The spectrum of AlO. *Mon. Not. Roy. Astron. Soc.*, 449:3613–3619, 2015.

[52] S. N. Yurchenko, Audra Blissett, Usama Asari, Marcus Vasilios, Christian Hill, and J. Tennyson. ExoMol Molecular linelists – XIII. The spectrum of CaO. *Mon. Not. Roy. Astron. Soc.*, 456:4524–4532, 2016.

[53] L. K. McKemmish, S. N. Yurchenko, and J. Tennyson. ExoMol Molecular linelists – XVIII. The spectrum of Vanadium Oxide. *Mon. Not. Roy. Astron. Soc.*, 463:771–793, 2016.

[54] L. K. McKemmish, T. Masseron, J Hoeijmakers, V. V. Pérez-Mesa, S. L. Grimm, S. N. Yurchenko, and J. Tennyson. ExoMol Molecular line lists – XXXIII. The spectrum of Titanium Oxide. *Mon. Not. Roy. Astron. Soc.*, 488:2836–2854, 2019.

[55] S. N. Yurchenko, Alexander N. Smirnov, Victor G. Solomonik, and J. Tennyson. Spectroscopy of YO from first principles. *Phys. Chem. Chem. Phys.*, 21:22794–22810, 2019.

[56] S. N. Yurchenko, J. Tennyson, A.-M. Syme, A. Y. Adam, V. H. J. Clark, B. Cooper, C. P. Dobney, S. T. E. Donnelly, M. N. Gorman, A. E. Lynas-Gray, T. Meltzer, A. Owens, Q. Qu, M. Semenov, W. Somogyi, A. Upadhyay, S. Wright, and J. C. Zapata Trujillo. ExoMol line lists – XLIV. IR and UV line list for silicon monoxide (^{28}Si^{16}O). *Mon. Not. Roy. Astron. Soc.*, 510:903–919, 2022.

[57] M. Pezzella, S. N. Yurchenko, and J. Tennyson. A method for calculating temperature-dependent photodissociaiton cross sections and rates. *Phys. Chem. Chem. Phys.*, 23:16390–16400, 2021.

[58] T. Rivlin, L. K. McKemmish, K. E. Spinlove, and J. Tennyson. Low temperature scattering with the R-matrix method: argon-argon scattering. *Mol. Phys.*, 117(21):3158–3170, 2019.

[59] W. Somogyi, S. N. Yurchenko, and A. Yachmenev. Calculation of electric quadrupole linestrengths for diatomic molecules: Application to the H_2, CO, HF, and O_2 molecules. *J. Chem. Phys.*, 155(21):214303, 2021.

[60] Mariusz Puchalski, Jacek Komasa, and Krzysztof Pachucki. Hyperfine Structure of the First Rotational Level in H_2, D_2 and HD Molecules and the Deuteron Quadrupole Moment. *Phys. Rev. Lett.*, 125(25):253001, 2020.

[61] Arthur Fast and Samuel A. Meek. Frequency comb referenced spectroscopy of A-X 0-0 transitions in SH. *J. Chem. Phys.*, 154:114304, 2021.

[62] Mark Brouard, Helen Chadwick, Yuan Pin Chang, Brian J. Howard, Sarantos Marinakis, Nicholas Screen, Scott A. Seamons, and Alessandra La Via. The hyperfine structure of NO($A\,^2\Sigma^+$). *J. Mol. Spectrosc.*, 282:42–49, 2012.

[63] Matthew T. Hummon, Mark Yeo, Benjamin K. Stuhl, Alejandra L. Collopy, Yong Xia, and Jun Ye. 2D magneto-optical trapping of diatomic molecules. *Phys. Rev. Lett.*, 110:1–5, 2013.

[64] Mark Yeo, Matthew T. Hummon, Alejandra L. Collopy, Bo Yan, Boerge Hemmerling, Eunmi Chae, John M. Doyle, and Jun Ye. Rotational State Microwave Mixing for Laser Cooling of Complex Diatomic Molecules. *Phys. Rev. Lett.*, 114:1–5, 2015.

[65] Jeremy J. Harrison, John M. Brown, DeWayne T. Halfen, and Lucy M. Ziurys. Improved Frequencies of Rotational Transitions of ^{52}CrH in the $^6\Sigma^+$ Ground State . *Astron. J.*, 637:1143–1147, 2006.

[66] Robert L. Cook and Frank C. De Lucia. Application of the Theory of Irreducible Tensor Operators to Molecular Hyperfine Structure. *Am. J. Phys.*, 39:1433–1454, 1971.

[67] R. A. Frosch and H. M. Foley. Magnetic hyperfine structure in diatomic molecules. *Phys. Rev.*, 88:1337–1349, 1952.

[68] John M. Brown and Alan Carrington. *Rotational Spectroscopy of Diatomic Molecules*. Cambridge University Press, 2003.

[69] J. Bardeen and C. H. Townes. Calculation of nuclear quadrupole effects in molecules. *Phys. Rev.*, 73:97–105, 1948.

[70] Karl F. Freed. Theory of the Hyperfine Structure of Molecules: Application to $^3\Pi$ States of Diatomic Molecules Intermediate between Hund's Cases (a) and (b). *J. Chem. Phys.*, 45:4214–4241, 1966.

[71] M. Broyer, J. Vigué, and J.C. Lehmann. Effective hyperfine Hamiltonian in homonuclear diatomic molecules. Application to the B state of molecular iodine. *J. Phys.*, 39:591–609, 1978.

[72] H Kato. Energy-levels and line-intensities of diatomic-molecules – application to alkali-metal molecules. *Bull. Chem. Soc. Japan*, 66:3203–3234, 1993.

[73] J. M. Brown and B. J. Howard. An approach to the anomalous commutation relations of rotational angular momenta in molecules. *Mol. Phys.*, 31:1517–1525, 1976.

[74] J. H. Van Vleck. The coupling of angular momentum vectors in molecules. *Rev. Mod. Phys.*, 23:213–227, 1951.

[75] A. Osterwalder, A. Wüest, F. Merkt, and Ch. Jungen. High-resolution millimeter wave spectroscopy and multichannel quantum defect theory of the hyperfine structure in high Rydberg states of molecular hydrogen H_2. *J. Chem. Phys.*, 121:11810–11838, 2004.

[76] A. Deller and S. D. Hogan. Excitation and characterization of long-lived hydrogenic Rydberg states of nitric oxide. *J. Chem. Phys.*, 152:144305, 2020.

[77] R. Gallusser and K. Dressler. Multistate vibronic coupling between the excited $^2\Pi$ states of the NO molecule. *J. Chem. Phys.*, 76:4311–4327, 1982.

[78] James A. J. Fitzpatrick, Frederick R. Manby, and Colin M. Western. The interpretation of molecular magnetic hyperfine interactions. *J. Chem. Phys.*, 122:084312, 2005.

[79] A. Miani and J. Tennyson. Can ortho-para transitions for water be observed? *J. Chem. Phys.*, 120:2732–2739, 2004.

[80] Pekka Pyykkö. Year-2017 nuclear quadrupole moments. *Mol. Phys.*, 116:1328–1338, 2018.

[81] Eizi Hirota. *High-Resolution Spectroscopy of Transient Molecules*, volume 40 of *Springer Series in Chemical Physics*. Springer Berlin Heidelberg, Berlin, Heidelberg, 1985.

[82] Colin M. Western. PGOPHER: A program for simulating rotational, vibrational and electronic spectra. *J. Quant. Spectrosc. Radiat. Transf.*, 186:221–242, 2017.

[83] Andy Wong, Sergei N. Yurchenko, Peter Bernath, Holger S. P. Müller, Stephanie McConkey, and Jonathan Tennyson. ExoMol line list: XXI. Nitric Oxide NO. *Mon. Not. Roy. Astron. Soc.*, 470:882–897, 2017.

[84] B. Yadin, T. Vaness, P. Conti, C. Hill, S. N. Yurchenko, and J. Tennyson. ExoMol Molecular linelists: I The rovibrational spectrum of BeH, MgH and CaH the $X^2\Sigma^+$ state. *Mon. Not. Roy. Astron. Soc.*, 425:34–43, 2012.

[85] I. E. Gordon, L. S. Rothman, R. J. Hargreaves, R. Hashemi, E. V. Karlovets, F. M. Skinner, E. K. Conway, C. Hill, R. V. Kochanov, Y. Tan, P. Wcisło, A. A. Finenko, K. Nelson, P. F. Bernath, M. Birk, V. Boudon, A. Campargue, K. V. Chance, A. Coustenis, B. J. Drouin, J.–M. Flaud, R. R. Gamache, J. T. Hodges, D. Jacquemart, E. J. Mlawer, A. V. Nikitin, V. I. Perevalov, M. Rotger, J. Tennyson, G. C. Toon, H. Tran, V. G. Tyuterev, E. M. Adkins, A. Baker, A. Barbe, E. Canè, A. G. Császár, A. Dudaryonok, O. Egorov, A. J. Fleisher, H. Fleurbaey, A. Foltynowicz, T. Furtenbacher, J. J. Harrison,

J.–M. Hartmann, V.–M. Horneman, X. Huang, T. Karman, J. Karns, S. Kassi, I. Kleiner, V. Kofman, F. Kwabia–Tchana, N. N. Lavrentieva, T. J. Lee, D. A. Long, A. A. Lukashevskaya, O. M. Lyulin, V. Yu. Makhnev, W. Matt, S. T. Massie, M. Melosso, S. N. Mikhailenko, D. Mondelain, H. S. P. Müller, O. V. Naumenko, A. Perrin, O. L. Polyansky, E. Raddaoui, P. L. Raston, Z. D. Reed, M. Rey, C. Richard, R. Tóbiás, I. Sadiek, D. W. Schwenke, E. Starikova, K. Sung, F. Tamassia, S. A. Tashkun, J. Vander Auwera, I. A. Vasilenko, A. A. Vigasin, G. L. Villanueva, B. Vispoel, G. Wagner, A. Yachmenev, and S. N. Yurchenko. The HITRAN2020 molecular spectroscopic database. *J. Quant. Spectrosc. Radiat. Transf.*, 277:107949, 2022.

[86] L R Zink, D A Jennings, K M Evenson, and K R Leopold. Laboratory measurements for the astrophysical identification of mgh. *Astrophys. J.*, 359:L65–L66, 1990.

[87] Kestutis Aidas, Celestino Angeli, Keld L. Bak, Vebjørn Bakken, Radovan Bast, Linus Boman, Ove Christiansen, Renzo Cimiraglia, Sonia Coriani, Pål Dahle, Erik K. Dalskov, Ulf Ekström, Thomas Enevoldsen, Janus J. Eriksen, Patrick Ettenhuber, Berta Fernández, Lara Ferrighi, Heike Fliegl, Luca Frediani, Kasper Hald, Asger Halkier, Christof Hättig, Hanne Heiberg, Trygve Helgaker, Alf Christian Hennum, Hinne Hettema, Eirik Hjertenaes, Stinne Høst, Ida-Marie Høyvik, Maria Francesca Iozzi, Branislav Jansík, Hans Jørgen Aa. Jensen, Dan Jonsson, Poul Jørgensen, Joanna Kauczor, Sheela Kirpekar, Thomas Kjaergaard, Wim Klopper, Stefan Knecht, Rika Kobayashi, Henrik Koch, Jacob Kongsted, Andreas Krapp, Kasper Kristensen, Andrea Ligabue, Ola B. Lutnaes, Juan I. Melo, Kurt V. Mikkelsen, Rolf H. Myhre, Christian Neiss, Christian B. Nielsen, Patrick Norman, Jeppe Olsen, Jógvan Magnus H. Olsen, Anders Osted, Martin J. Packer, Filip Pawlowski, Thomas B. Pedersen, Patricio F. Provasi, Simen Reine, Zilvinas Rinkevicius, Torgeir A. Ruden, Kenneth Ruud, Vladimir V. Rybkin, Pawel Sałek, Claire C. M. Samson, Alfredo Sánchez de Merás, Trond Saue, Stephan P. A. Sauer, Bernd Schimmelpfennig, Kristian Sneskov, Arnfinn H. Stein-

dal, Kristian O. Sylvester-Hvid, Peter R. Taylor, Andrew M. Teale, Erik I. Tellgren, David P. Tew, Andreas J. Thorvaldsen, Lea Thøgersen, Olav Vahtras, Mark A. Watson, David J. D. Wilson, Marcin Ziolkowski, and Hans Ågren. The Dalton quantum chemistry program system. *Wiley Interdiscip. Rev.-Comput. Mol. Sci.*, 4:269–284, 2014.

[88] Michael E. Harding, Thorsten Metzroth, Jurgen Gauss, and Alexander A. Auer. Parallel calculation of CCSD and CCSD(T) analytic first and second derivatives. *J Chem. Theory Comput.*, 4:64–74, 2008.

[89] Donald E. Canfield, Alexander N. Glazer, and Paul G. Falkowski. The evolution and future of earth's nitrogen cycle. *Science*, 330:192–196, 2010.

[90] Peter M. Vitousek, John D. Aber, Robert W. Howarth, Gene E. Likens, Pamela A. Matson, David W. Schindler, William H. Schlesinger, and David G. Tilman. Human alteration of the global nitrogen cycle: Sources and consequences. *Ecol. Appl.*, 7:737–750, 1997.

[91] W. L. Chameides, P. S. Kasibhatla, J. Yienger, and H. Levy. Growth of Continental-Scale Metro-Agro-Plexes, Regional Ozone Pollution, and World Food Production. *Science*, 264:74–77, 1994.

[92] G. E. Likens, C. T. Driscoll, and D. C. Buso. Long-term effects of acid rain: Response and recovery of a forest ecosystem. *Science*, 272:244–246, 1996.

[93] A. Singh and M. Agrawal. Acid rain and its ecological consequences. *J. Environ. Biol.*, 29:15, 2007.

[94] Y. Hu, S. Naito, N. Kobayashi, and M. Hasatani. CO_2, NO_x and SO_2 emissions from the combustion of coal with high oxygen concentration gases. *Fuel*, 79:1925–1932, 2000.

[95] Y. H. Li, G. Q. Lu, and V. Rudolph. The kinetics of NO and N_2O reduction over coal chars in fluidised-bed combustion. *Chem. Eng. Sci.*, 53:1–26, 1998.

[96] David S. Bredt and Solomon H. Snyder. Nitric oxide, a novel neuronal messenger. *Neuron*, 8:3–11, 1992.

[97] D. S. Bredt and S. H. Snyder. Nitric oxide: A physiological messenger molecule. *Annu. Rev. Biochem.*, 63:175–195, 1994.

[98] Magdalena Arasimowicz and Jolanta Floryszak-Wieczorek. Nitric oxide as a bioactive signalling molecule in plant stress responses. *Plant. Sci.*, 172:876–887, 2007.

[99] Bernd Mayer and Benjamin Hemmens. Biosynthesis and action of nitric oxide in mammalian cells. *Trends Biochem. Sci.*, 22:477–481, 1997.

[100] Alvaro G. Estévez and Joaquín Jordán. Nitric oxide and superoxide, a deadly cocktail. *Ann. N.Y. Acad. Sci.*, 962:207–211, 2002.

[101] C. Cox, A. Saglam, J.-C. Gerard, J.-L. Bertaux, F. Gonzalez-Galindo, F. Leblanc, and A. Reberac. Distribution of the ultraviolet nitric oxide Martian night airglow: Observations from Mars Express and comparisons with a one-dimensional model. *J. Geophys. Res.-Planets*, 113:E08012, 2008.

[102] S. W. Bougher, J. C. Gérard, A. I. F. Stewart, and C. G. Fesen. The venus nitric oxide night airglow: Model calculations based on the venus thermospheric general circulation model. *J. Geophys. Res.-Space Phys.*, 95(A5):6271–6284, 1990.

[103] Jean-Loup Bertaux, François Leblanc, Séverine Perrier, E. Quemerais, Oleg Korablev, E. Dimarellis, A. Reberac, F. Forget, P. C. Simon, S. A. Stern, and Bill Sandel. Nightglow in the upper atmosphere of mars and implications for atmospheric transport. *Science*, 307(5709):566–569, 2005.

[104] M. Gerin, Y. Viala, F. Pauzat, and Y. Ellinger. The abundance of nitric oxide in molecular clouds. *Astron. Astrophys.*, 266:463–478, 1992.

[105] M. Gerin, Y. Viala, and F. Casoli. The abundance of nitric oxide in TMC 1. *Astron. Astrophys.*, 268:212–214, 1993.

[106] D. T. Halfen, A. J. Apponi, and L. M. Ziurys. Evaluating the N/O Chemical Network: The Distribution of N_2O and NO in the Sagittarius B2 Complex. *Astron. J.*, 561:244–253, 2001.

[107] S. Martin, R. Mauersberger, J. Martin-Pintado, S. Garcia-Burillo, and C. Henkel. First detections of extragalactic SO_2, NS and NO. *Astron. Astrophys.*, 411:L465–L468, 2003.

[108] Howard Chen, Zhuchang Zhan, Allison Youngblood, Eric T. Wolf, Adina D. Feinstein, and Daniel E. Horton. Persistence of flare-driven atmospheric chemistry on rocky habitable zone worlds. *Nature Astronomy*, 5:298–310, 2021.

[109] J. R. Partington. Joan Baptista van Helmont. *Ann. Sci.*, 1:359–384, 1936.

[110] Joseph Priestley. Observations on different kinds of air. *Philos. Trans. R. Soc. Lond.*, 62:147–264, 1772.

[111] W. G. Bessler and C. Schulz. Quantitative multi-line NO-LIF temperature imaging. *Appl. Phys. B-Lasers Opt.*, 78:519–533, 2004.

[112] A. F. H. Van Gessel, B. Hrycak, M. Jasiński, J. Mizeraczyk, J. J. A. M. Van Der Mullen, and P. J. Bruggeman. Temperature and NO density measurements by LIF and OES on an atmospheric pressure plasma jet. *J. Phys. D-Appl. Phys.*, 46:095201, 2013.

[113] Jonathan Tennyson, Sergei N. Yurchenko, Ahmed F. Al-Refaie, Emma J. Barton, Katy L. Chubb, Phillip A. Coles, S. Diamantopoulou, Maire N. Gorman, Christian Hill, Aden Z. Lam, Lorenzo Lodi, Laura K. McKemmish, Yueqi Na, Alec Owens, Oleg L. Polyansky, T Rivlin, Clara Sousa-Silva, Daniel S. Underwood, Andrey Yachmenev, and Emil Zak. The ExoMol database: molecular line lists for exoplanet and other hot atmospheres. *J. Mol. Spectrosc.*, 327:73–94, 2016.

[114] Andy Wong, S. N. Yurchenko, Peter Bernath, Holger S. P. Mueller, Stephanie McConkey, and J. Tennyson. ExoMol Line List XXI: Nitric Oxide (NO). *Mon. Not. Roy. Astron. Soc.*, 470:882–897, 2017.

[115] A. Lagerqvist and E. Miescher. Absorptionsspektrum des NO-Molekuels: Feinstruktur-Analyse der δ-und β-Banden und homogene Stoerung C2Π–B2Π. *Helv. Phys. Acta*, 31:221–262, 1958.

[116] J. Danielak, U. Domin, R. Kepa, M. Rytel, and M. Zachwieja. Reinvestigation of the emission gamma band system ($A\ ^2\Sigma^+ - X\ ^2\Pi$) of the NO molecule. *J. Mol. Spectrosc.*, 181:394–402, 1997.

[117] I. E. Gordon, L. S. Rothman, C. Hill, R. V. Kochanov, Y. Tan, P. F. Bernath, M. Birk, V. Boudon, A. Campargue, K. V. Chance, B. J. Drouin, J.-M. Flaud, R. R. Gamache, J. T. Hodges, D. Jacquemart, V. I. Perevalov, A. Perrin, K. P. Shine, M.-A. H. Smith, J. Tennyson, G. C. Toon, H. Tran, V. G. Tyuterev, A. Barbe, A. G. Császár, V. M. Devi, T. Furtenbacher, J. J. Harrison, J.-M. Hartmann, A. Jolly, T. J. Johnson, T. Karman, I. Kleiner, A. A. Kyuberis, J. Loos, O. M. Lyulin, S. T. Massie, S. N. Mikhailenko, N. Moazzen-Ahmadi, H. S. P. Müller, O. V. Naumenko, A. V. Nikitin, O. L. Polyansky, M. Rey, M. Rotger, S. W. Sharpe, K. Sung, E. Starikova, S. A. Tashkun, J. Vander Auwera, G. Wagner, J. Wilzewski, P. Wcisło, S. Yu, and E. J. Zak. The *HITRAN* 2016 molecular spectroscopic database. *J. Quant. Spectrosc. Radiat. Transf.*, 203:3–69, 2017.

[118] J. Luque and D. R. Crosley. Electronic-transition moment for the $B\ ^2\Pi$ - $X\ ^2\Pi$ system of NO. *J. Quant. Spectrosc. Radiat. Transf.*, 53:189–200, 1995.

[119] Jorge Luque and David R. Crosley. Radiative and predissociative rates for NO $A^2\Sigma^+$ v' = 0-5 and $D^2\Sigma^+$ v'= 0-3. *J. Chem. Phys.*, 112:9411–9416, 2000.

[120] K. Yoshino, J. R. Esmond, W. H. Parkinson, A. P. Thorne, J. E. Murray, R. C. M. Learner, G. Cox, A. S.-C. Cheung, K. W.-S. Leung, K. Ito, T. Matsui, and T. Imajo. The application of a VUV Fourier transform spectrometer

and synchrotron radiation source to measurements of: I. The *beta*(9,0) band of NO. *J. Chem. Phys.*, 109:1751–1757, 1998.

[121] D. L. Albritton, A. L. Schmeltekopf, and R. N. Zare. Potential energy curves for NO^+. *J. Chem. Phys.*, 71(8):3271–3279, 1979.

[122] T. Furtenbacher, A. G. Császár, and J. Tennyson. MARVEL: measured active rotational-vibrational energy levels. *J. Mol. Spectrosc.*, 245:115–125, 2007.

[123] Roland Tóbiás, Tibor Furtenbacher, Jonathan Tennyson, and Attila G. Császár. Accurate empirical rovibrational energies and transitions of $H_2{}^{16}O$. *Phys. Chem. Chem. Phys.*, 21:3473–3495, 2019.

[124] H. J. Werner, P. J. Knowles, G. Knizia, F. R. Manby, M. Schütz, P. Celani, W. Györffy, D. Kats, T. Korona, R. Lindh, A. Mitrushenkov, G. Rauhut, K. R. Shamasundar, T. B. Adler, R. D. Amos, A. Bernhardsson, A. Berning, D. L. Cooper, M. J. O. Deegan, A. J. Dobbyn, F. Eckert, E. Goll, C. Hampel, A. Hesselmann, G. Hetzer, T. Hrenar, G. Jansen, C. Köppl, Y. Liu, A. W. Lloyd, R. A. Mata, A. J. May, S. J. McNicholas, W. Meyer, M. E. Mura, A. Nicklass, D. P. O'Neill, P. Palmieri, D. Peng, K. Pflüger, R. Pitzer, M. Reiher, T. Shiozaki, H. Stoll, A. J. Stone, R. Tarroni, T. Thorsteinsson, and M. Wang. Molpro, version 2015.1, a package of ab initio programs. http://www.molpro.net, 2015.

[125] John F. Stanton. On the vibronic level structure in the NO_3 radical. i. the ground electronic state. *J. Chem. Phys.*, 126:134309, 2007.

[126] Hans-Joachim Werner, Peter J. Knowles, Gerald Knizia, Frederick R. Manby, and Martin Schütz. Molpro: a general-purpose quantum chemistry program package. *WIREs Comput. Mol. Sci.*, 2:242–253, 2012.

[127] F. Grein and A. Kapur. Low-lying valence and Rydberg states of nitric-oxide NO: Configuration-interaction studies. *J. Chem. Phys.*, 77:415–423, 1982.

[128] R. Devivie and S. D. Peyerimhoff. Theoretical spectroscopy of the NO radical. 1. Potential curves and lifetimes of excited states. *J. Chem. Phys.*, 89:3028–3043, 1988.

[129] Junxia Cheng, Hong Zhang, and Xinlu Cheng. Theoretical study of the structure and spectra for the γ and β systems of NO. *Comput. Theor. Chem.*, 1114:165–171, 2017.

[130] Junxia Cheng, Hong Zhang, Xinlu Cheng, and Xiaoshu Song. Theoretical study of spectral parameters for the γ and β band systems of NO for atmosphere and high temperature. *Mol. Phys.*, 115:2577–2585, 2017.

[131] Ramon S. da Silva, Maikel Y. Ballester, Laiz R. Ventura, and Carlos E. Fellows. Theoretical study of the spin-orbit coupling in the $X^2\Pi$ state of NO. *Chem. Phys. Lett.*, 780:138896, 2021.

[132] D. M. Cooper. Theoretical study of IR band intensities and electronic transition moments for the beta and delta systems of NO. *J. Quant. Spectrosc. Radiat. Transf.*, 27:459–465, 1982.

[133] S. R. Langhoff, C. W. Bauschlicher, and H. Partridge. Theoretical study of the NO gamma-system. *J. Chem. Phys.*, 89:4909–4917, 1988.

[134] S. R. Langhoff, H. Partridge, C. W. Bauschlicher, and A. Komornicki. Theoretical study of the NO beta-system. *J. Chem. Phys.*, 94:6638–6643, 1991.

[135] R. Polak and J. Fiser. On the behavior of the low-lying $^2\Sigma^+$ electronic states of NO. *Chem. Phys. Lett.*, 377:564–570, 2003.

[136] T. H. Dunning. Gaussian basis sets for use in correlated molecular calculations. I. The atoms boron through neon and hydrogen . *J. Chem. Phys.*, 90:1007–1023, 1989.

[137] K. P. Huber and G. Herzberg. *Molecular Spectra and Molecular Structure IV. Constants of Diatomic Molecules*. Van Nostrand Reinhold Company, New York, 1979.

[138] J. E. Murray, K. Yoshino, J. R. Esmond, W. H. Parkinson, Y. Sun, A. Dalgarno, Anne P. Thorne, and G. Cox. Vacuum ultraviolet Fourier transform spectroscopy of the δ(0,0) and β(7,0) bands of NO. *J. Chem. Phys.*, 101:62–73, 1994.

[139] T. Imajo, K. Yoshino, J. R. Esmond, W. H. Parkinson, A. P. Thorne, J. E. Murray, R. C. M. Learner, G. Cox, A. S.-C. Cheung, K. Ito, and T. Matsui. The application of a VUV Fourier transform spectrometer and synchrotron radiation source to measurements of: II. The $\delta(1,0)$ band of NO. *J. Chem. Phys.*, 112:2251–2257, 2000.

[140] A. S-C. Cheung, D. H-Y. Lo, K. W.-S. Leung, K. Yoshino, A. P. Thorne, J. E. Murray, K. Ito, T. Matsui, and T. Imajo. The application of a vacuum ultraviolet Fourier transform spectrometer and synchrotron radiation source to measurements of: IV. The $\beta(6,0)$ and $\gamma(3,0)$ bands of NO. *J. Chem. Phys.*, 116:155–161, 2002.

[141] J. Rufus, K. Yoshino, A. P. Thorne, J. E. Murray, T. Imajo, K. Ito, and T. Matsui. The application of a vacuum ultraviolet Fourier transform spectrometer and synchrotron radiation source to measurements of: V. The $\beta(11,0)$ band of NO. *J. Chem. Phys.*, 117:10621–10626, 2002.

[142] G. W. Faris and P. C. Cosby. Observation of NO $B^2\Pi$(v=3) - $X^2\Pi$(v=0) absorptions with 1+1 multiphoton ionization: Precision line position measurements and parity assignment of the $B^2\Pi$ state. *J. Chem. Phys.*, 97:7073–7086, 1992.

[143] M. Drabbels and A. M. Wodtke. The electric dipole moment and hyperfine structure of NO $B^2\Pi$: High resolution laser-induced fluorescence spectroscopy of the B $^2\Pi$(v=3-5) ¡- X $^2\Pi$(v=0) bands. *Chem. Phys. Lett.*, 256:8–14, 1996.

[144] C. Amiot and J. Verges. Fine Structure of the $C^2\Pi$- $A^2\Sigma^+$ and $D^2\Sigma^+$ - $A^2\Sigma^+$ Band Systems of the NO Molecule: Homogeneous and Heterogeneous Perturbations. *Phys. Scr.*, 25:302–311, 1982.

[145] A. G. Császár and T. Furtenbacher. Spectroscopic networks. *J. Mol. Spectrosc.*, 266:99 – 103, 2011.

[146] A. P. Thorne, J. Rufus, K. Yoshino, A. S.-C. Cheung, and T. Imajo. Erratum: The application of a VUV Fourier transform spectrometer and synchrotron radiation source to measurements of absorption bands of NO [J. Chem. Phys. 115, 3719 (2001); 116, 155 (2002); 117, 10621 (2002); 119, 8373 (2003)]. *J. Chem. Phys.*, 122:179901, 2005.

[147] Laiz R. Ventura and C. E. Fellows. The $^{14}N^{16}O$ γ system reviewed through Fourier transform spectroscopy. *J. Quant. Spectrosc. Radiat. Transf.*, 246:2–6, 2020.

[148] D T Colbert and W H Miller. A novel discrete variable representation for quantum-mechanical reactive scattering via the s-matrix kohn method. *J. Chem. Phys.*, 96:1982–1991, 1992.

[149] E G Lee, J Y Seto, T Hirao, P F Bernath, and R J Le Roy. FTIR emission spectra, molecular constants, and potential curve of ground state GeO. *J. Mol. Spectrosc.*, 194:197–202, 1999.

[150] S. N. Yurchenko, Istvan Szabo, Elizaveta Pyatenko, and J. Tennyson. ExoMol Molecular line lists XXXI: The spectrum of C_2. *Mon. Not. Roy. Astron. Soc.*, 480:3397–3411, 2018.

[151] J M Brown and A J Merer. Lambda-type doubling parameters for molecules in Π-electronic states of triplet and higher multiplicity. *J. Mol. Spectrosc.*, 74:488–494, 1979.

[152] S. T. Pratt. Vibrational autoionization and predissociation in high Rydberg states of nitric oxide. *J. Chem. Phys.*, 108:7131–7140, 1998.

[153] Jeffrey A. Sheehy, Charles W. Bauschlicher, Stephen R. Langhoff, and Harry Partridge. Theoretical study of the nitric oxide ϵ and 11000 Å bands. *Chem. Phys. Lett.*, 225:221–228, 1994.

[154] T. B. Settersten, B. D. Patterson, and W. H. Humphries. Radiative lifetimes of NO $A^2\Sigma^+$ ($v' = 0, 1, 2$) and the electronic transition moment of the $A^2\Sigma^+$ - $X^2\Pi$ system. *J. Chem. Phys.*, 131:11, 2009.

[155] Qianwei Qu, B. Cooper, Sergei N. Yurchenko, and Jonathan Tennyson. A spectroscopic model for the low-lying electronic states of NO. *J. Chem. Phys.*, 154:074112, 2021.

[156] J. Tennyson, C. Hill, and S. N. Yurchenko. Data structures for ExoMol: Molecular line lists for exoplanet and other atmospheres. In *6^{th} international conference on atomic and molecular data and their applications ICAMDATA-2012*, volume 1545 of *AIP Conference Proceedings*, pages 186–195. AIP, New York, 2013.

[157] H. S. P. Müller, K. Kobayashi, K. Takahashi, K. Tomaru, and F. Matsushima. Terahertz spectroscopy of $N^{18}O$ and isotopic invariant fit of several nitric oxide isotopologs. *J. Mol. Spectrosc.*, 310:92–98, 2015.

[158] D.J. Hart and O.L. Bourne. High-resolution coherent VUV spectroscopy of NO[$C^2\Pi(1)$ - $B^2\Pi(10)$, $B^2\Pi(11)$] and CO[$B^1\Sigma(0)$]. *Chem. Phys.*, 133:103–112, 1989.

[159] G. E. Gadd and T. G. Slanger. NO($B\ ^2\Pi$) radiative lifetimes: v =0–6. *J. Chem. Phys.*, 92:2194–2202, 1990.

[160] P. F. Bernath. Molecular astronomy of cool stars and sub-stellar objects. *Int. Rev. Phys. Chem.*, 28:681–709, 2009.

[161] N. Madhusudhan and S. Seager. On the inference of thermal inversions in hot Jupiter atmospheres. *Astrophys. J.*, 725:261, 2010.

[162] Thomas M. Evans, David K. Sing, Hannah R. Wakeford, Nikolay Nikolov, Gilda E. Ballester, Benjamin Drummond, Tiffany Kataria, Neale P. Gibson, David S. Amundsen, and Jessica Spake. Detection of H_2O and evidence for tio/vo in an ultra-hot exoplanet atmosphere. *Astrophys. J.*, 822:L4, 2016.

[163] Jake D. Turner, Robin M. Leiter, Lauren I. Biddle, Kyle A. Pearson, Kevin K. Hardegree-Ullman, Robert M. Thompson, Johanna K. Teske, Ian T. Cates, Kendall L. Cook, Michael P. Berube, Megan N. Nieberding, Christen K. Jones, Brandon Raphael, Spencer Wallace, Zachary T. Watson, and Robert E. Johnson. Investigating the physical properties of transiting hot Jupiters with the 1.5-m Kuiper Telescope. *Mon. Not. Roy. Astron. Soc.*, 472:3871–3886, 2017.

[164] E. Palle, G. Chen, J. Prieto-Arranz, G. Nowak, F. Murgas, L. Nortmann, D. Pollacco, K. Lam, P. Montanes-Rodriguez, H. Parviainen, and N. Casasayas-Barris. Feature-rich transmission spectrum for WASP-127b Cloud-free skies for the puffiest known super-Neptune? *Astron. Astrophys.*, 602, 2017.

[165] A. Tsiaras, I. P. Waldmann, T. Zingales, M. Rocchetto, G. Morello, M. Damiano, K. Karpouzas, G. Tinetti, L. K. McKemmish, J. Tennyson, and S. N. Yurchenko. A population study of gaseous exoplanets. *Astron. J.*, 155:156, 2018.

[166] Jayesh M. Goyal, Nathan Mayne, Benjamin Drummond, David K. Sing, Eric Hebrard, Nikole Lewis, Pascal Tremblin, Mark W. Phillips, Thomas Mikal-Evans, and Hannah R. Wakeford. A library of self-consistent simulated exoplanet atmospheres. *Mon. Not. Roy. Astron. Soc.*, 498:4680–4704, 2020.

[167] N. K. Lewis, H. R. Wakeford, R. J. MacDonald, J. M. Goyal, D. K. Sing, J. Barstow, D. Powell, T. Kataria, I. Mishra, M. S. Marley, N. E. Batalha, J. I. Moses, P. Gao, T. J. Wilson, K. L. Chubb, T. Mikal-Evans, N. Nikolov, N. Pirzkal, J. J. Spake, K. B. Stevenson, J. Valenti, and X. Zhang. Into the

UV: The Atmosphere of the Hot Jupiter HAT-P-41b Revealed. *Astrophys. J. Lett.*, 902:L19, 2020.

[168] L. K. McKemmish, T. Masseron, S. Sheppard, E. Sandeman, Z. Schofield, T. Furtenbacher, A. G. Császár, J. Tennyson, and C. Sousa-Silva. MARVEL analysis of the measured high-resolution spectra of $^{48}Ti^{16}O$. *Astrophys. J. Suppl. Ser.*, 228:15, 2017.

[169] Stevanus K. Nugroho, Hajime Kawahara, Kento Masuda, Teruyuki Hirano, Takayuki Kotani, and Akito Tajitsu. High-resolution Spectroscopic Detection of TiO and a Stratosphere in the Day-side of WASP-33b. *Astrophys. J.*, 154:221, 2017.

[170] Dilovan B. Serindag, Ignas A. G. Snellen, and Paul Molliere. Measuring titanium isotope ratios in exoplanet atmospheres. *Astron. Astrophys.*, 655:A69, 2021.

[171] Bibiana Prinoth, H. Jens Hoeijmakers, Daniel Kitzmann, Elin Sandvik, Julia Seidel, V, Monika Lendl, Nicholas W. Borsato, Brian Thorsbro, David R. Anderson, David Barrado, Kateryna Kravchenko, Romain Allart, Vincent Bourrier, Heather M. Cegla, David Ehrenreich, Chloe Fisher, Christophe Lovis, Andrea Guzman-Mesa, Simon Grimm, Matthew Hooton, Brett M. Morris, Maria Oreshenko, Lorenzo Pino, and Kevin Heng. Titanium oxide and chemical inhomogeneity in the atmosphere of the exoplanet WASP-189 b. *Nature Astr.*, 6:449–457, 2022.

[172] S. de Regt, A. Y. Kesseli, I. A. G. Snellen, S. R. Merritt, and K. L. Chubb. A quantitative assessment of the VO line list: Inaccuracies hamper high-resolution VO detections in exoplanet atmospheres. *arXiv e-prints*, page arXiv:2203.03585, March 2022.

[173] A. J. Merer. Spectroscopy of the diatomic 3d transition-metal oxides. *Annu. Rev. Phys. Chem.*, 40:407–438, 1989.

[174] C. A. Bowesman, H. Akbari, S. Hopkins, S. N. Yurchenko, and J. Tennyson. Fine and hyperfine resolved empirical energy levels for VO. *J. Quant. Spectrosc. Radiat. Transf.*, 289:108295, 2022.

[175] W. H. Hocking, A. J. Merer, and D. J. Milton. Resolved hyperfine structure in the C–X electronic transition of VO. An internal hyperfine perturbation in the C $^4\Sigma^-$ state. *Can. J. Phys.*, 59:266–270, 1981.

[176] A. S-C. Cheung, R. C. Hansen, and A. J. Merer. Laser spectroscopy of VO: Analysis of the rotational and hyperfine structure of the C $^4\Sigma^-$–X $^4\Sigma^-$ (0, 0) band. *J. Mol. Spectrosc.*, 91:165–208, 1982.

[177] R. D. Suenram, G. T. Fraser, F. J. Lovas, and C. W. Gillies. Microwave spectra and electric dipole moments of X $^4\Sigma^-_{12}$ VO and NbO. *J. Mol. Spectrosc.*, 148:114–122, 1991.

[178] A. G. Adam, M. Barnes, B. Berno, R. D. Bower, and A. J. Merer. Rotational and Hyperfine Structure in the B $^4\Pi$–X $^4\Sigma^-$ (0,0) Band of VO at 7900 Å: Perturbations by the a $^2\Sigma^+$, v = 2 Level. *J. Mol. Spectrosc.*, 170:94–130, 1995.

[179] A. S. C. Cheung, P. G. Hajigeorgiou, G. Huang, S. Z. Huang, and A. J. Merer. Rotational structure and perturbations in the BETA-4-PI-CHI-4-SIGMA-(1,0) band of VO. *J. Mol. Spectrosc.*, 163:443–458, 1994.

[180] Qianwei Qu, S. N. Yurchenko, and J. Tennyson. Hyperfine-resolved variational nuclear motion spectra of diatomic molecules. *J. Chem. Theory Comput.*, 18:1808–1820, 2022.

[181] C. W. Bauschlicher and P. Maitre. Theoretical-study of the first transition row oxides and sulfides. *Theor. Chim. Acta.*, 90:189–203, 1995.

[182] A. J. Bridgeman and J. Rothery. Periodic trends in the diatomic monoxides and monosulfides of the 3d transition metals. *J. Chem. Soc. Dalton*, pages 211–218, 2000.

[183] M. Calatayud, B. Silvi, J. Andres, and A. Beltran. A theoretical study on the structure, energetics and bonding of VO_x^+ and VO_x (x=1-4) systems. *Chem. Phys. Lett.*, 333:493–503, 2001.

[184] E. Broclawik and T. Borowski. Time-dependent DFT study on electronic states of vanadium and molybdenum oxide molecules. *Chem. Phys. Lett.*, 339:433–437, 2001.

[185] B. Dai, K. M. Deng, J. L. Yang, and Q. S. Zhu. Excited states of the 3d transition metal monoxides. *J. Chem. Phys.*, 118:9608–9613, 2003.

[186] M. Pykavy and C. van Wullen. Multireference correlation calculations for the ground states of $VO^{+/0/-}$ using correlation consistent basis sets. *J. Phys. Chem. A*, 107:5566–5572, 2003.

[187] Heather J. Kulik and Nicola Marzari. Systematic study of first-row transition-metal diatomic molecules: A self-consistent DFT plus U approach. *J. Chem. Phys.*, 133:114103, 2010.

[188] Evangelos Miliordos and Aristides Mavridis. Electronic structure of vanadium oxide. Neutral and charged species, $VO^{0,\pm}$. *J. Phys. Chem. A*, 111:1953–1965, 2007.

[189] Olaf Hübner, Julius Hornung, and Hans-Jörg Himmel. The electronic structure of VO in its ground and electronically excited states: A combined matrix isolation and quantum chemical (MRCI) study. *J. Chem. Phys.*, 143:024309, 2015.

[190] Laura K. McKemmish, Sergei N. Yurchenko, and Jonathan Tennyson. Ab initio calculations to support accurate modelling of the rovibronic spectroscopy calculations of vanadium monoxide (VO). *Mol. Phys.*, 114:3232–3248, 2016.

[191] Tonghuan Jiang, Yilin Chen, Nikolay A. Bogdanov, Enge Wang, Ali Alavi, and Ji Chen. A full configuration interaction quantum Monte Carlo study of ScO, TiO, and VO molecules. *J. Chem. Phys.*, page 164302, 2021.

[192] A. G. Adam, M. Barnes, B. Berno, R. D. Bower, and A. J. Merer. Rotational and hyperfine-structure in the $B^4\Pi$-$X^4\Sigma^-$ (0,0) band of VO at 7900 Angstrom: Perturbations by the $a^2\Sigma^+$, v=2 level. *J. Mol. Spectrosc.*, 170:94–130, 1995.

[193] W. Scott Hopkins, Suzanne M. Hamilton, and Stuart R. Mackenzie. The electronic spectrum of vanadium monoxide across the visible: New bands and new insight. *J. Chem. Phys.*, 130:144308, 2009.

[194] Frank Neese. The ORCA program system. *Wiley Interdiscip. Rev.-Comput. Mol. Sci.*, 2:73–78, 2012.

[195] Arthur Schweiger and Gunnar Jeschke. *Principles of pulse electron paramagnetic resonance*. Oxford University Press, 2001.

[196] A. S. C. Cheung, R. C. Hansen, and A. J. Merer. Laser Spectroscopy of VO-Analysis of the Rotational and Hyperfine Structure of the C $^4\Sigma^-$–X $^4\Sigma^-$ (O, O) band. *J. Mol. Spectrosc.*, 91:165–208, 1982.

[197] Lars Karlsson, Bo Lindgren, Cecilia Lundevall, and Ulf Sassenberg. Lifetime Measurements of the A $^4\Pi$, B $^4\Pi$, and C $^4\Sigma^-$ States of VO. *J. Mol. Spectrosc.*, 181:274–278, 1997.

[198] Timothy J. Slotterback, Simon G. Clement, Kenneth C. Janda, and Colin M. Western. Hyperfine analysis of the mixed $A^3\Pi_1$ $v = 28$ and $X^1\Sigma^+$ $v = 69$ states of $I^{35}Cl$. *J. Chem. Phys.*, 103(21):9125–9131, 1995.